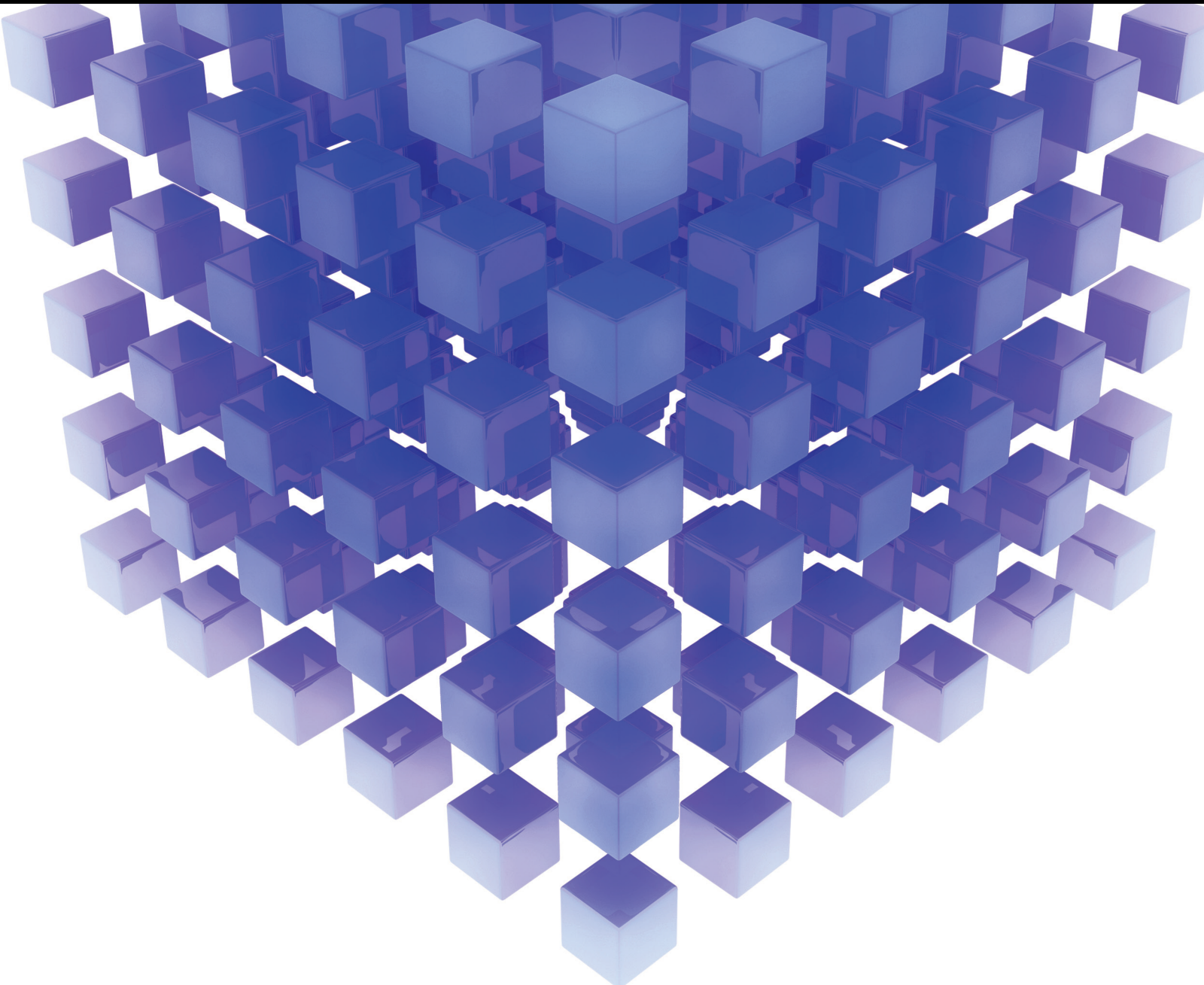


Application of Machine Learning in Civil Engineering

Lead Guest Editor: Afaq Ahmad

Guest Editors: Abdul Razzaq Ghumman, Faisal Shabbir, and Toqeer Mahmood





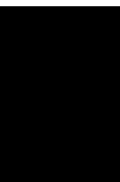
Application of Machine Learning in Civil Engineering

Mathematical Problems in Engineering

Application of Machine Learning in Civil Engineering

Lead Guest Editor: Afaq Ahmad


Guest Editors: Abdul Razzaq Ghumman, Faisal
Shabbir, and Toqeer Mahmood



Copyright © 2022 Hindawi Limited. All rights reserved.

This is a special issue published in “Mathematical Problems in Engineering.” All articles are open access articles distributed under the Creative Commons Attribution License, which permits unrestricted use, distribution, and reproduction in any medium, provided the original work is properly cited.

Chief Editor

Guangming Xie , China

Academic Editors

Kumaravel A , India
Waqas Abbasi, Pakistan
Mohamed Abd El Aziz , Egypt
Mahmoud Abdel-Aty , Egypt
Mohammed S. Abdo, Yemen
Mohammad Yaghoub Abdollahzadeh
Jamalabadi , Republic of Korea
Rahib Abiyev , Turkey
Leonardo Acho , Spain
Daniela Adnessi , Italy
Arooj Adeel , Pakistan
Waleed Adel , Egypt
Ramesh Agarwal , USA
Francesco Aggogeri , Italy
Ricardo Aguilar-Lopez , Mexico
Afaq Ahmad , Pakistan
Naveed Ahmed , Pakistan
Elias Aifantis , USA
Akif Akgul , Turkey
Tareq Al-shami , Yemen
Guido Ala, Italy
Andrea Alaimo , Italy
Reza Alam, USA
Osamah Albahri , Malaysia
Nicholas Alexander , United Kingdom
Salvatore Alfonzetti, Italy
Ghous Ali , Pakistan
Nouman Ali , Pakistan
Mohammad D. Aliyu , Canada
Juan A. Almendral , Spain
A.K. Alomari, Jordan
José Domingo Álvarez , Spain
Cláudio Alves , Portugal
Juan P. Amezcua-Sanchez, Mexico
Mukherjee Amitava, India
Lionel Amodeo, France
Sebastian Anita, Romania
Costanza Arico , Italy
Sabri Arik, Turkey
Fausto Arpino , Italy
Rashad Asharabi , Saudi Arabia
Farhad Aslani , Australia
Mohsen Asle Zaem , USA

Andrea Avanzini , Italy
Richard I. Avery , USA
Viktor Avrutin , Germany
Mohammed A. Awadallah , Malaysia
Francesco Aymerich , Italy
Sajad Azizi , Belgium
Michele Bacciocchi , Italy
Seungik Baek , USA
Khaled Bahlali, France
M.V.A Raju Bahubalendruni, India
Pedro Balaguer , Spain
P. Balasubramaniam, India
Stefan Balint , Romania
Ines Tejado Balsera , Spain
Alfonso Banos , Spain
Jerzy Baranowski , Poland
Tudor Barbu , Romania
Andrzej Bartoszewicz , Poland
Sergio Baselga , Spain
S. Caglar Baslamisli , Turkey
David Bassir , France
Chiara Bedon , Italy
Azeddine Beghdadi, France
Andriette Bekker , South Africa
Francisco Beltran-Carbajal , Mexico
Abdellatif Ben Makhlof , Saudi Arabia
Denis Benasciutti , Italy
Ivano Benedetti , Italy
Rosa M. Benito , Spain
Elena Benvenuti , Italy
Giovanni Berselli, Italy
Michele Betti , Italy
Pietro Bia , Italy
Carlo Bianca , France
Simone Bianco , Italy
Vincenzo Bianco, Italy
Vittorio Bianco, Italy
David Bigaud , France
Sardar Muhammad Bilal , Pakistan
Antonio Bilotta , Italy
Sylvio R. Bistafa, Brazil
Chiara Boccaletti , Italy
Rodolfo Bontempo , Italy
Alberto Borboni , Italy
Marco Bortolini, Italy

Paolo Boscariol, Italy
Daniela Boso , Italy
Guillermo Botella-Juan, Spain
Abdesselem Boulkroune , Algeria
Boulaïd Boulkroune, Belgium
Fabio Bovenga , Italy
Francesco Braghin , Italy
Ricardo Branco, Portugal
Julien Bruchon , France
Matteo Bruggi , Italy
Michele Brun , Italy
Maria Elena Bruni, Italy
Maria Angela Butturi , Italy
Bartłomiej Błachowski , Poland
Dhanamjayulu C , India
Raquel Caballero-Águila , Spain
Filippo Cacace , Italy
Salvatore Caddemi , Italy
Zuowei Cai , China
Roberto Caldelli , Italy
Francesco Cannizzaro , Italy
Maosen Cao , China
Ana Carpio, Spain
Rodrigo Carvajal , Chile
Caterina Casavola, Italy
Sara Casciati, Italy
Federica Caselli , Italy
Carmen Castillo , Spain
Inmaculada T. Castro , Spain
Miguel Castro , Portugal
Giuseppe Catalanotti , United Kingdom
Alberto Cavallo , Italy
Gabriele Cazzulani , Italy
Fatih Vehbi Celebi, Turkey
Miguel Cerrolaza , Venezuela
Gregory Chagnon , France
Ching-Ter Chang , Taiwan
Kuei-Lun Chang , Taiwan
Qing Chang , USA
Xiaoheng Chang , China
Prasenjit Chatterjee , Lithuania
Kacem Chehdi, France
Peter N. Cheimets, USA
Chih-Chiang Chen , Taiwan
He Chen , China



































Kebing Chen , China
Mengxin Chen , China
Shyi-Ming Chen , Taiwan
Xizhong Chen , Ireland
Xue-Bo Chen , China
Zhiwen Chen , China
Qiang Cheng, USA
Zeyang Cheng, China
Luca Chiapponi , Italy
Francisco Chicano , Spain
Tirivanhu Chinyoka , South Africa
Adrian Chmielewski , Poland
Seongim Choi , USA
Gautam Choubey , India
Hung-Yuan Chung , Taiwan
Yusheng Ci, China
Simone Cinquemani , Italy
Roberto G. Citarella , Italy
Joaquim Ciurana , Spain
John D. Clayton , USA
Piero Colajanni , Italy
Giuseppina Colicchio, Italy
Vassilios Constantoudis , Greece
Enrico Conte, Italy
Alessandro Contento , USA
Mario Cools , Belgium
Gino Cortellessa, Italy
Carlo Cosentino , Italy
Paolo Crippa , Italy
Erik Cuevas , Mexico
Guozeng Cui , China
Mehmet Cunkas , Turkey
Giuseppe D'Aniello , Italy
Peter Dabnichki, Australia
Weizhong Dai , USA
Zhifeng Dai , China
Purushothaman Damodaran , USA
Sergey Dashkovskiy, Germany
Adiel T. De Almeida-Filho , Brazil
Fabio De Angelis , Italy
Samuele De Bartolo , Italy
Stefano De Miranda , Italy
Filippo De Monte , Italy

José António Fonseca De Oliveira
Correia , Portugal
Jose Renato De Sousa , Brazil
Michael Defoort, France
Alessandro Della Corte, Italy
Laurent Dewasme , Belgium
Sanku Dey , India
Gianpaolo Di Bona , Italy
Roberta Di Pace , Italy
Francesca Di Puccio , Italy
Ramón I. Diego , Spain
Yannis Dimakopoulos , Greece
Hasan Dinçer , Turkey
José M. Domínguez , Spain
Georgios Dounias, Greece
Bo Du , China
Emil Dumic, Croatia
Madalina Dumitriu , United Kingdom
Premraj Durairaj , India
Saeed Eftekhari Azam, USA
Said El Kafhali , Morocco
Antonio Elipse , Spain
R. Emre Erkmen, Canada
John Escobar , Colombia
Leandro F. F. Miguel , Brazil
FRANCESCO FOTI , Italy
Andrea L. Facci , Italy
Shahla Faisal , Pakistan
Giovanni Falsone , Italy
Hua Fan, China
Jianguang Fang, Australia
Nicholas Fantuzzi , Italy
Muhammad Shahid Farid , Pakistan
Hamed Faruqi, Iran
Yann Favennec, France
Fiorenzo A. Fazzolari , United Kingdom
Giuseppe Fedele , Italy
Roberto Fedele , Italy
Baowei Feng , China
Mohammad Ferdows , Bangladesh
Arturo J. Fernández , Spain
Jesus M. Fernandez Oro, Spain
Francesco Ferrise, Italy
Eric Feulvarch , France
Thierry Floquet, France

Eric Florentin , France
Gerardo Flores, Mexico
Antonio Forcina , Italy
Alessandro Formisano, Italy
Francesco Franco , Italy
Elisa Francomano , Italy
Juan Frausto-Solis, Mexico
Shujun Fu , China
Juan C. G. Prada , Spain
HECTOR GOMEZ , Chile
Matteo Gaeta , Italy
Mauro Gaggero , Italy
Zoran Gajic , USA
Jaime Gallardo-Alvarado , Mexico
Mosè Gallo , Italy
Akemi Gálvez , Spain
Maria L. Gandarias , Spain
Hao Gao , Hong Kong
Xingbao Gao , China
Yan Gao , China
Zhiwei Gao , United Kingdom
Giovanni Garcea , Italy
José García , Chile
Harish Garg , India
Alessandro Gasparetto , Italy
Stylianios Georgantzinou, Greece
Fotios Georgiades , India
Parviz Ghadimi , Iran
Ştefan Cristian Gherghina , Romania
Georgios I. Giannopoulos , Greece
Agathoklis Giaralis , United Kingdom
Anna M. Gil-Lafuente , Spain
Ivan Giorgio , Italy
Gaetano Giunta , Luxembourg
Jefferson L.M.A. Gomes , United Kingdom
Emilio Gómez-Déniz , Spain
Antonio M. Gonçalves de Lima , Brazil
Qunxi Gong , China
Chris Goodrich, USA
Rama S. R. Gorla, USA
Veena Goswami , India
Xunjie Gou , Spain
Jakub Grabski , Poland

Antoine Grall , France
George A. Gravvanis , Greece
Fabrizio Greco , Italy
David Greiner , Spain
Jason Gu , Canada
Federico Guarracino , Italy
Michele Guida , Italy
Muhammet Gul , Turkey
Dong-Sheng Guo , China
Hu Guo , China
Zhaoxia Guo, China
Yusuf Gurefe, Turkey
Salim HEDDAM , Algeria
ABID HUSSANAN, China
Quang Phuc Ha, Australia
Li Haitao , China
Petr Hájek , Czech Republic
Mohamed Hamdy , Egypt
Muhammad Hamid , United Kingdom
Renke Han , United Kingdom
Weimin Han , USA
Xingsi Han, China
Zhen-Lai Han , China
Thomas Hanne , Switzerland
Xinan Hao , China
Mohammad A. Hariri-Ardebili , USA
Khalid Hattaf , Morocco
Defeng He , China
Xiao-Qiao He, China
Yanchao He, China
Yu-Ling He , China
Ramdane Hedjar , Saudi Arabia
Jude Hemanth , India
Reza Hemmati, Iran
Nicolae Herisanu , Romania
Alfredo G. Hernández-Díaz , Spain
M.I. Herreros , Spain
Eckhard Hitzer , Japan
Paul Honeine , France
Jaromir Horacek , Czech Republic
Lei Hou , China
Yingkun Hou , China
Yu-Chen Hu , Taiwan
Yunfeng Hu, China
Can Huang , China
Gordon Huang , Canada
Linsheng Huo , China
Sajid Hussain, Canada
Asier Ibeas , Spain
Orest V. Iftime , The Netherlands
Przemyslaw Ignaciuk , Poland
Giacomo Innocenti , Italy
Emilio Insfran Pelozo , Spain
Azeem Irshad, Pakistan
Alessio Ishizaka, France
Benjamin Ivorra , Spain
Breno Jacob , Brazil
Reema Jain , India
Tushar Jain , India
Amin Jajarmi , Iran
Chiranjibe Jana , India
Łukasz Jankowski , Poland
Samuel N. Jator , USA
Juan Carlos Jáuregui-Correa , Mexico
Kandasamy Jayakrishna, India
Reza Jazar, Australia
Khalide Jbilou, France
Isabel S. Jesus , Portugal
Chao Ji , China
Qing-Chao Jiang , China
Peng-fei Jiao , China
Ricardo Fabricio Escobar Jiménez , Mexico
Emilio Jiménez Macías , Spain
Maolin Jin, Republic of Korea
Zhuo Jin, Australia
Ramash Kumar K , India
BHABEN KALITA , USA
MOHAMMAD REZA KHEDMATI , Iran
Viacheslav Kalashnikov , Mexico
Mathiyalagan Kalidass , India
Tamas Kalmar-Nagy , Hungary
Rajesh Kaluri , India
Jyotheeswara Reddy Kalvakurthi, India
Zhao Kang , China
Ramani Kannan , Malaysia
Tomasz Kapitaniak , Poland
Julius Kaplunov, United Kingdom
Konstantinos Karamanos, Belgium
Michal Kawulok, Poland

Irfan Kaymaz , Turkey
Vahid Kayvanfar , Qatar
Krzysztof Kecik , Poland
Mohamed Khader , Egypt
Chaudry M. Khalique , South Africa
Mukhtaj Khan , Pakistan
Shahid Khan , Pakistan
Nam-Il Kim, Republic of Korea
Philipp V. Kiryukhantsev-Korneev ,
Russia
P.V.V Kishore , India
Jan Koci , Czech Republic
Ioannis Kostavelis , Greece
Sotiris B. Kotsiantis , Greece
Frederic Kratz , France
Vamsi Krishna , India
Edyta Kucharska, Poland
Krzysztof S. Kulpa , Poland
Kamal Kumar, India
Prof. Ashwani Kumar , India
Michal Kunicki , Poland
Cedrick A. K. Kwuimy , USA
Kyandoghere Kyamakya, Austria
Ivan Kyrchei , Ukraine
Márcio J. Lacerda , Brazil
Eduardo Lalla , The Netherlands
Giovanni Lancioni , Italy
Jaroslaw Latalski , Poland
Hervé Laurent , France
Agostino Lauria , Italy
Aimé Lay-Ekuakille , Italy
Nicolas J. Leconte , France
Kun-Chou Lee , Taiwan
Dimitri Lefebvre , France
Eric Lefevre , France
Marek Lefik, Poland
Yaguo Lei , China
Kauko Leiviskä , Finland
Ervin Lenzi , Brazil
ChenFeng Li , China
Jian Li , USA
Jun Li , China
Yueyang Li , China
Zhao Li , China






























Zhen Li , China
En-Qiang Lin, USA
Jian Lin , China
Qibin Lin, China
Yao-Jin Lin, China
Zhiyun Lin , China
Bin Liu , China
Bo Liu , China
Heng Liu , China
Jianxu Liu , Thailand
Lei Liu , China
Sixin Liu , China
Wanquan Liu , China
Yu Liu , China
Yuanchang Liu , United Kingdom
Bonifacio Llamazares , Spain
Alessandro Lo Schiavo , Italy
Jean Jacques Loiseau , France
Francesco Lolli , Italy
Paolo Lonetti , Italy
António M. Lopes , Portugal
Sebastian López, Spain
Luis M. López-Ochoa , Spain
Vassilios C. Loukopoulos, Greece
Gabriele Maria Lozito , Italy
Zhiguo Luo , China
Gabriel Luque , Spain
Valentin Lychagin, Norway
YUE MEI, China
Junwei Ma , China
Xuanlong Ma , China
Antonio Madeo , Italy
Alessandro Magnani , Belgium
Toqeer Mahmood , Pakistan
Fazal M. Mahomed , South Africa
Arunava Majumder , India
Sarfranz Nawaz Malik, Pakistan
Paolo Manfredi , Italy
Adnan Maqsood , Pakistan
Muazzam Maqsood, Pakistan
Giuseppe Carlo Marano , Italy
Damijan Markovic, France
Filipe J. Marques , Portugal
Luca Martinelli , Italy
Denizar Cruz Martins, Brazil

Francisco J. Martos , Spain
Elio Masciari , Italy
Paolo Massioni , France
Alessandro Mauro , Italy
Jonathan Mayo-Maldonado , Mexico
Pier Luigi Mazzeo , Italy
Laura Mazzola, Italy
Driss Mehdi , France
Zahid Mehmood , Pakistan
Roderick Melnik , Canada
Xiangyu Meng , USA
Jose Merodio , Spain
Alessio Merola , Italy
Mahmoud Mesbah , Iran
Luciano Mescia , Italy
Laurent Mevel , France
Constantine Michailides , Cyprus
Mariusz Michta , Poland
Prankul Middha, Norway
Aki Mikkola , Finland
Giovanni Minafò , Italy
Edmondo Minisci , United Kingdom
Hiroyuki Mino , Japan
Dimitrios Mitsotakis , New Zealand
Ardashir Mohammadzadeh , Iran
Francisco J. Montáns , Spain
Francesco Montefusco , Italy
Gisele Mophou , France
Rafael Morales , Spain
Marco Morandini , Italy
Javier Moreno-Valenzuela , Mexico
Simone Morganti , Italy
Caroline Mota , Brazil
Aziz Moukrim , France
Shen Mouquan , China
Dimitris Mourtzis , Greece
Emiliano Mucchi , Italy
Taseer Muhammad, Saudi Arabia
Ghulam Muhiuddin, Saudi Arabia
Amitava Mukherjee , India
Josefa Mula , Spain
Jose J. Muñoz , Spain
Giuseppe Muscolino, Italy
Marco Mussetta , Italy

Hariharan Muthusamy, India
Alessandro Naddeo , Italy
Raj Nandkeolyar, India
Keivan Navaie , United Kingdom
Soumya Nayak, India
Adrian Neagu , USA
Erivelton Geraldo Nepomuceno , Brazil
AMA Neves, Portugal
Ha Quang Thinh Ngo , Vietnam
Nhon Nguyen-Thanh, Singapore
Papakostas Nikolaos , Ireland
Jelena Nikolic , Serbia
Tatsushi Nishi, Japan
Shanzhou Niu , China
Ben T. Nohara , Japan
Mohammed Nouari , France
Mustapha Nourelfath, Canada
Kazem Nouri , Iran
Ciro Núñez-Gutiérrez , Mexico
Włodzimierz Ogryczak, Poland
Roger Ohayon, France
Krzysztof Okarma , Poland
Mitsuhiro Okayasu, Japan
Murat Olgun , Turkey
Diego Oliva, Mexico
Alberto Olivares , Spain
Enrique Onieva , Spain
Calogero Orlando , Italy
Susana Ortega-Cisneros , Mexico
Sergio Ortobelli, Italy
Naohisa Otsuka , Japan
Sid Ahmed Ould Ahmed Mahmoud , Saudi Arabia
Taoreed Owolabi , Nigeria
EUGENIA PETROPOULOU , Greece
Arturo Pagano, Italy
Madhumangal Pal, India
Pasquale Palumbo , Italy
Dragan Pamučar, Serbia
Weifeng Pan , China
Chandan Pandey, India
Rui Pang, United Kingdom
Jürgen Pannek , Germany
Elena Panteley, France
Achille Paolone, Italy

George A. Papakostas , Greece
Xosé M. Pardo , Spain
You-Jin Park, Taiwan
Manuel Pastor, Spain
Pubudu N. Pathirana , Australia
Surajit Kumar Paul , India
Luis Payá , Spain
Igor Pažanin , Croatia
Libor Pekař , Czech Republic
Francesco Pellicano , Italy
Marcello Pellicciari , Italy
Jian Peng , China
Mingshu Peng, China
Xiang Peng , China
Xindong Peng, China
Yuexing Peng, China
Marzio Pennisi , Italy
Maria Patrizia Pera , Italy
Matjaz Perc , Slovenia
A. M. Bastos Pereira , Portugal
Wesley Peres, Brazil
F. Javier Pérez-Pinal , Mexico
Michele Perrella, Italy
Francesco Pesavento , Italy
Francesco Petrini , Italy
Hoang Vu Phan, Republic of Korea
Lukasz Pieczonka , Poland
Dario Piga , Switzerland
Marco Pizzarelli , Italy
Javier Plaza , Spain
Goutam Pohit , India
Dragan Poljak , Croatia
Jorge Pomares , Spain
Hiram Ponce , Mexico
Sébastien Poncet , Canada
Volodymyr Ponomaryov , Mexico
Jean-Christophe Ponsart , France
Mauro Pontani , Italy
Sivakumar Poruran, India
Francesc Pozo , Spain
Aditya Rio Prabowo , Indonesia
Anchasa Pramuanjaroenkij , Thailand
Leonardo Primavera , Italy
B Rajanarayan Prusty, India

Krzysztof Puszynski , Poland
Chuan Qin , China
Dongdong Qin, China
Jianlong Qiu , China
Giuseppe Quaranta , Italy
DR. RITU RAJ , India
Vitomir Racic , Italy
Carlo Rainieri , Italy
Kumbakonam Ramamani Rajagopal, USA
Ali Ramazani , USA
Angel Manuel Ramos , Spain
Higinio Ramos , Spain
Muhammad Afzal Rana , Pakistan
Muhammad Rashid, Saudi Arabia
Manoj Rastogi, India
Alessandro Rasulo , Italy
S.S. Ravindran , USA
Abdolrahman Razani , Iran
Alessandro Reali , Italy
Jose A. Reinoso , Spain
Oscar Reinoso , Spain
Haijun Ren , China
Carlo Renno , Italy
Fabrizio Renno , Italy
Shahram Rezapour , Iran
Ricardo Rianza , Spain
Francesco Riganti-Fulginei , Italy
Gerasimos Rigatos , Greece
Francesco Ripamonti , Italy
Jorge Rivera , Mexico
Eugenio Roanes-Lozano , Spain
Ana Maria A. C. Rocha , Portugal
Luigi Rodino , Italy
Francisco Rodríguez , Spain
Rosana Rodríguez López, Spain
Francisco Rossomando , Argentina
Jose de Jesus Rubio , Mexico
Weiguo Rui , China
Rubén Ruiz , Spain
Ivan D. Rukhlenko , Australia
Dr. Eswaramoorthi S. , India
Weichao SHI , United Kingdom
Chaman Lal Sabharwal , USA
Andrés Sáez , Spain

Bekir Sahin, Turkey
Laxminarayan Sahoo , India
John S. Sakellariou , Greece
Michael Sakellariou , Greece
Salvatore Salamone, USA
Jose Vicente Salcedo , Spain
Alejandro Salcido , Mexico
Alejandro Salcido, Mexico
Nunzio Salerno , Italy
Rohit Salgotra , India
Miguel A. Salido , Spain
Sinan Salih , Iraq
Alessandro Salvini , Italy
Abdus Samad , India
Sovan Samanta, India
Nikolaos Samaras , Greece
Ramon Sancibrian , Spain
Giuseppe Sanfilippo , Italy
Omar-Jacobo Santos, Mexico
J Santos-Reyes , Mexico
José A. Sanz-Herrera , Spain
Musavarah Sarwar, Pakistan
Shahzad Sarwar, Saudi Arabia
Marcelo A. Savi , Brazil
Andrey V. Savkin, Australia
Tadeusz Sawik , Poland
Roberta Sburlati, Italy
Gustavo Scaglia , Argentina
Thomas Schuster , Germany
Hamid M. Sedighi , Iran
Mijanur Rahaman Seikh, India
Tapan Senapati , China
Lotfi Senhadji , France
Junwon Seo, USA
Michele Serpilli, Italy
Silvestar Šesnić , Croatia
Gerardo Severino, Italy
Ruben Sevilla , United Kingdom
Stefano Sfarra , Italy
Dr. Ismail Shah , Pakistan
Leonid Shaikhet , Israel
Vimal Shanmuganathan , India
Prayas Sharma, India
Bo Shen , Germany
Hang Shen, China

Xin Pu Shen, China
Dimitri O. Shepelsky, Ukraine
Jian Shi , China
Amin Shokrollahi, Australia
Suzanne M. Shontz , USA
Babak Shotorban , USA
Zhan Shu , Canada
Angelo Sifaleras , Greece
Nuno Simões , Portugal
Mehakpreet Singh , Ireland
Piyush Pratap Singh , India
Rajiv Singh, India
Seralathan Sivamani , India
S. Sivasankaran , Malaysia
Christos H. Skiadas, Greece
Konstantina Skouri , Greece
Neale R. Smith , Mexico
Bogdan Smolka, Poland
Delfim Soares Jr. , Brazil
Alba Sofi , Italy
Francesco Soldovieri , Italy
Raffaele Solimene , Italy
Yang Song , Norway
Jussi Sopanen , Finland
Marco Spadini , Italy
Paolo Spagnolo , Italy
Ruben Specogna , Italy
Vasilios Spitas , Greece
Ivanka Stamova , USA
Rafał Stanisławski , Poland
Miladin Stefanović , Serbia
Salvatore Strano , Italy
Yakov Strelniker, Israel
Kangkang Sun , China
Qiuqin Sun , China
Shuaishuai Sun, Australia
Yanchao Sun , China
Zong-Yao Sun , China
Kumarasamy Suresh , India
Sergey A. Suslov , Australia
D.L. Suthar, Ethiopia
D.L. Suthar , Ethiopia
Andrzej Swierniak, Poland
Andras Szekrenyes , Hungary
Kumar K. Tamma, USA




Yong (Aaron) Tan, United Kingdom
Marco Antonio Taneco-Hernández , Mexico
Lu Tang , China
Tianyou Tao, China
Hafez Tari , USA
Alessandro Tasora , Italy
Sergio Teggi , Italy
Adriana del Carmen Téllez-Anguiano , Mexico
Ana C. Teodoro , Portugal
Efstathios E. Theotokoglou , Greece
Jing-Feng Tian, China
Alexander Timokha , Norway
Stefania Tomasiello , Italy
Gisella Tomasini , Italy
Isabella Torricollo , Italy
Francesco Tornabene , Italy
Mariano Torrisi , Italy
Thang nguyen Trung, Vietnam
George Tsiatas , Greece
Le Anh Tuan , Vietnam
Nerio Tullini , Italy
Emilio Turco , Italy
Ilhan Tuzcu , USA
Efstratios Tzirtzilakis , Greece
FRANCISCO UREÑA , Spain
Filippo Ubertini , Italy
Mohammad Uddin , Australia
Mohammad Safi Ullah , Bangladesh
Serdar Ulubeyli , Turkey
Mati Ur Rahman , Pakistan
Panayiotis Vafeas , Greece
Giuseppe Vairo , Italy
Jesus Valdez-Resendiz , Mexico
Eusebio Valero, Spain
Stefano Valvano , Italy
Carlos-Renato Vázquez , Mexico
Martin Velasco Villa , Mexico
Franck J. Vernerey, USA
Georgios Veronis , USA
Vincenzo Vespri , Italy
Renato Vidoni , Italy
Venkatesh Vijayaraghavan, Australia

Anna Vila, Spain
Francisco R. Villatoro , Spain
Francesca Vipiana , Italy
Stanislav Vitek , Czech Republic
Jan Vorel , Czech Republic
Michael Vynnycky , Sweden
Mohammad W. Alomari, Jordan
Roman Wan-Wendner , Austria
Bingchang Wang, China
C. H. Wang , Taiwan
Dagang Wang, China
Guoqiang Wang , China
Huaiyu Wang, China
Hui Wang , China
J.G. Wang, China
Ji Wang , China
Kang-Jia Wang , China
Lei Wang , China
Qiang Wang, China
Qingling Wang , China
Weiwei Wang , China
Xinyu Wang , China
Yong Wang , China
Yung-Chung Wang , Taiwan
Zhenbo Wang , USA
Zhibo Wang, China
Waldemar T. Wójcik, Poland
Chi Wu , Australia
Qihong Wu, China
Yuqiang Wu, China
Zhibin Wu , China
Zhizheng Wu , China
Michalis Xenos , Greece
Hao Xiao , China
Xiao Ping Xie , China
Qingzheng Xu , China
Binghan Xue , China
Yi Xue , China
Joseph J. Yame , France
Chuanliang Yan , China
Xinggang Yan , United Kingdom
Hongtai Yang , China
Jixiang Yang , China
Mijia Yang, USA
Ray-Yeng Yang, Taiwan

Zaoli Yang , China
Jun Ye , China
Min Ye , China
Luis J. Yebra , Spain
Peng-Yeng Yin , Taiwan
Muhammad Haroon Yousaf , Pakistan
Yuan Yuan, United Kingdom
Qin Yuming, China
Elena Zaitseva , Slovakia
Arkadiusz Zak , Poland
Mohammad Zakwan , India
Ernesto Zambrano-Serrano , Mexico
Francesco Zammori , Italy
Jessica Zangari , Italy
Rafal Zdunek , Poland
Ibrahim Zeid, USA
Nianyin Zeng , China
Junyong Zhai , China
Hao Zhang , China
Haopeng Zhang , USA
Jian Zhang , China
Kai Zhang, China
Lingfan Zhang , China
Mingjie Zhang , Norway
Qian Zhang , China
Tianwei Zhang , China
Tongqian Zhang , China
Wenyu Zhang , China
Xianming Zhang , Australia
Xuping Zhang , Denmark
Yinyan Zhang, China
Yifan Zhao , United Kingdom
Debao Zhou, USA
Heng Zhou , China
Jian G. Zhou , United Kingdom
Junyong Zhou , China
Xueqian Zhou , United Kingdom
Zhe Zhou , China
Wu-Le Zhu, China
Gaetano Zizzo , Italy
Mingcheng Zuo, China

Contents




Cyclic Behavior of Retrofitted Low- and High-Strength Concrete Scaled Bridge Piers under Quasistatic Loading

Muhammad Khalid Hafiz , Qaiser-uz-Zaman Khan , and Sohaib Ahmad 
Research Article (17 pages), Article ID 2141485, Volume 2022 (2022)



Autonomous Classification and Decision-Making Support of Citizen E-Petitions Based on Bi-LSTM-CNN

Fengmei Sun  and Yi Zuo 
Research Article (17 pages), Article ID 9451108, Volume 2022 (2022)




3D Mechanical Characters and Their Fabric Evolutions of Granular Materials by DEM Simulation

Xuefeng Li , Weinan Lu , and Yuqi He 
Research Article (15 pages), Article ID 4765887, Volume 2022 (2022)

Remote Sensing Image Classification: A Comprehensive Review and Applications


Maryam Mehmood, Ahsan Shahzad, Bushra Zafar , Amsa Shabbir, and Nouman Ali 
Review Article (24 pages), Article ID 5880959, Volume 2022 (2022)

Evaluation of the Effectiveness of Collusion Control Policy Implementation by BP Neural Network Based on Annealing Algorithm Optimization

Chongsen Ma , Yun Chen , and Zeyang Lei 
Research Article (8 pages), Article ID 9238838, Volume 2022 (2022)

Research Article

Cyclic Behavior of Retrofitted Low- and High-Strength Concrete Scaled Bridge Piers under Quasistatic Loading

Muhammad Khalid Hafiz ¹, Qaiser-uz-Zaman Khan ¹ and Sohaib Ahmad ²

¹Civil Engineering Department, University of Engineering and Technology, Taxila, Pakistan

²Works and Services Organization, Islamabad, Pakistan

Correspondence should be addressed to Muhammad Khalid Hafiz; raomkhafiez@gmail.com

Received 27 February 2022; Revised 8 June 2022; Accepted 5 August 2022; Published 19 September 2022

Academic Editor: Ardashir Mohammadzadeh

Copyright © 2022 Muhammad Khalid Hafiz et al. This is an open access article distributed under the Creative Commons Attribution License, which permits unrestricted use, distribution, and reproduction in any medium, provided the original work is properly cited.

Bridges are vulnerable to devastation in the earthquake, resulting in the closure of the whole transport system of the particular region. Generally, pre-Kashmir earthquake bridges in Pakistan were not designed according to present seismic zoning requirements. Therefore, it is critical to evaluate their seismic performance and accordingly enhance their strength, stiffness, and thus reliability. Seismic retrofitting of existing bridges with CFRPs (carbon fiber-reinforced polymers) may be planned for typical bridge types of Pakistan. High-strength concrete (HSC) is now widely used in bridge construction, and the seismic behavior of typical bridge piers being a key component needs to be assessed. This investigation aims to evaluate the seismic performance of HSC piers before and after retrofitting in association with the earlier research in Pakistan on low-strength concrete prototypes. An experimental program was executed wherein scaled-down (4:1) HSC (6192 psi) RC bridge pier prototypes with axial load at the top were subjected to quasistatic cyclic loadings (QSCLs) under controlled drifts. The damaged pier prototypes were retrofitted with CFRP sheets beside another set of undamaged retrofitted models. The samples were tested under QSCL against several drift levels ranging from 0 to 5%. Hysteresis loops were drawn for each sample. The tests were studied for the assessment of the structural behavior of the prototypes. The results for the control models, damaged retrofitted models, and undamaged retrofitted models of low-strength concrete (LSC, 1800 psi and 2400 psi) obtained from doctoral research by Ali and Iqbal were compared with corresponding models of high-strength concrete (6192 psi). The outcomes clearly show a noteworthy increase in lateral load carrying capacity, ductility, strength, and energy absorption on an increase in concrete strength and retrofitting of the prototypes. The numerical modeling of these piers was in consistence with the experimental results. When retrofitted with CFRP, the existing bridge piers will enable the bridge stock to withstand high-intensity future earthquakes and lessen their seismic vulnerability against prospective damages.

1. Introduction

Bridges are the vital elements of a transport network. In an earthquake event, they are the most vulnerable to damage resulting in the closure of the whole transportation system. Generally, bridges constructed in Pakistan do not meet the present seismic requirements. After October 8, 2005 earthquake, seismic zoning, and seismic hazard maps were modified and the Building Code of Pakistan (BCP-2007) with seismic provisions was enforced. Bridges built prior to 2005 were constructed in accordance with the West Pakistan Code of Practice for Highway Bridges (WPCPHB1967),

wherein the earthquake considerations were nominal. This fact put these bridge structures at risk against newly recommended seismic zoning requirements [1, 2].

To reinforce the existing structures and to retrofit them for forthcoming challenges, a research was concluded to examine the behavior of reinforced concrete (RC) piers enwrapped with composites straps of fiber-reinforced plastic (FRP). Results established that RC piers showed noticeable enhancements in strength and translational ductility [3]. In addition, an investigation of short columns after wrapping with FRP composite tubes was finalized. Outcomes of this research revealed that the wrapping enhanced the capability

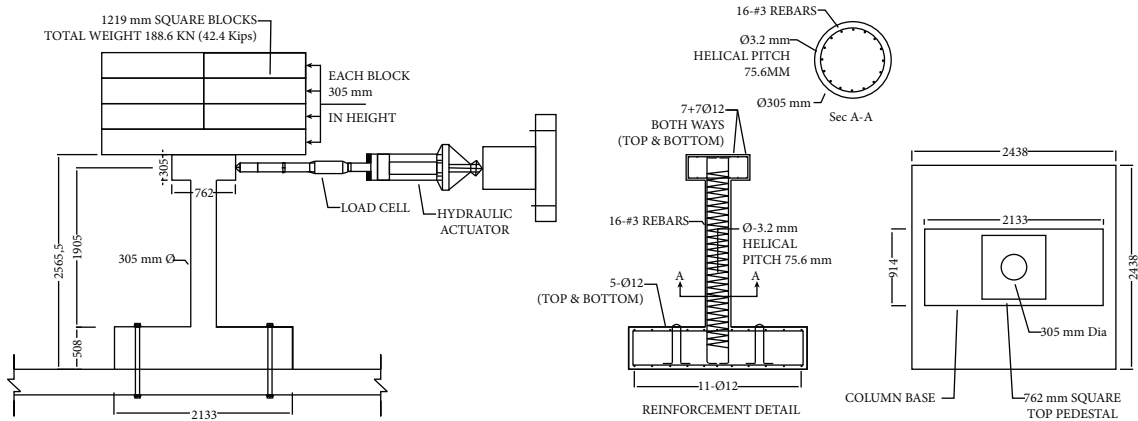


FIGURE 1: Investigational arrangement explaining the specimen sizes with top dead load arrangement and details of reinforcement used.

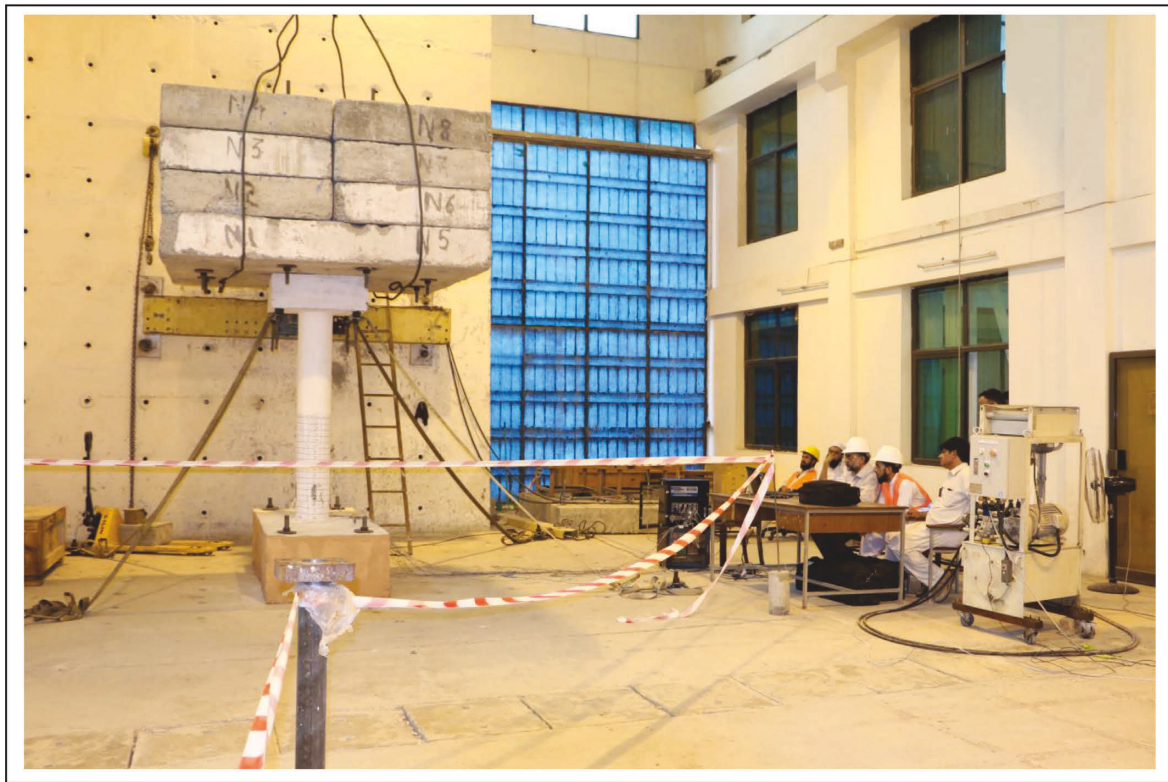


FIGURE 2: Test assembly setup with physical loading of 42.4 kips.

of tested RC columns in strain resistance, yielding, and energy dispersion [4]. In another study, surface-mounted FRP rods were bonded in the footings and the flexural capability of rectangular bridge piers was calculated. It was established that the flexural capacity of the piers was improved [5].

The properties of the materials used for confinement and the performance of confined cylinders were studied in the experimental investigations. The results concluded that columns were able to take 35% greater load when retrofitted with jacketing by pretensioned fiber-reinforced polymer

materials and were able to take 400% additional load when RC columns were unconfined but retrofitted [6]. In order to warrant shear failure, a work was carried out on short columns. Here, eight columns with deficient transverse steel and with longitudinal reinforcement higher than the upper boundaries were considered. CFRP application was made to seven out of these eight models. All of them were subjected to a sustained compressive load in addition to a lateral quasistatic cyclical loading. FRP reinforcement entirely transformed the failure mechanism of these samples and increased both the strength and ductility [7]. In addition,



FIGURE 3: Damaged column, cracks, and spalling of concrete.



FIGURE 4: Outer repair works with cementitious mix after filling of cracks.

four scaled-down pier samples having 1800 psi and 2400 psi concrete were tested under quasistatic cyclical loading. It was established that the ability of 1800 psi and 2400 psi models to dissipate energy was in a similar range. The cumulative energy dissipation did not have any remarkable difference within these limits of the concrete compressive strength [1].

The samples cracked in the investigation [1] were repaired and retrofitted. Additional prototypes were prepared and retrofitted in their undamaged position and placed under the study to ascertain the outcome of retrofitting on the strength and energy dispersion of low-strength concrete (LSC) piers. The evaluation concluded that the properties of undamaged but retrofitted models improved in their strength and ductility [8]. The evaluation of seismic behavior of two high-strength concrete (HSC)-reinforced short columns installed with PVC pipe confinement, and three additional similar column samples of HSC with conventional hoop confinement, steel, and steel tubes, respectively, was conducted by short-cycle reversed loading tests. Through these strengthening methods, the energy dissipation and deformation capability of HSC samples were efficiently enhanced [9].

In another study, six square slender HSC columns were tested. CFRP wrapping with changing thicknesses of carbon fiber over the height of all the column samples was made. The curves for moment versus curvature were plotted for all of these column segments, which revealed that segments with greater thickness of carbon fiber sheets displayed a noticeable improvement in the performance of the column subdivisions. The lateral moment carrying capability of jacket-confined samples was improved from 48% to 100% with the envelope of 0.40 inch thick carbon fiber sheets. An analytical study was also conducted, analysis results were matched with the experimental records, and it was noted that the load versus deformation graphs showed an acceptable arrangement [10].

A research work was carried out by retrofitting reinforced concrete columns with CFRP sheets in the longitudinal direction affixing them to their base. The outcomes established the enhancement in the lateral strength and the effective stiffness of these reinforced concrete samples [11]. The performance of nonductile RC slender column specimens when enwrapped with carbon fiber-reinforced polymer and subjected to cyclic load test showed substantial enhancement in respect of translational ductility, load



FIGURE 5: Grinded and prepared surface of pier for CFRP application.

carrying capacity, the total energy dissipation, and failure process [12]. Another investigational effort was concluded to estimate the effectiveness of the use of CFRP applications to retrofit the nonductile joints of beams or columns. It was appraised that the application of one layer of CFRP sheet appeared more beneficial than two layers [13]. The use of CFRP for fortifying the columns in RC buildings was probed for the capacities and the benefits by considering deviation of concrete class, reinforcement percentage and strengthening skills by conducting quasistatic tests both for

compressive loads and bending capability. It was established that CFRP applications are useful means to strengthen and retrofit RC structures due to the properties that they can comprehensively increase flexural properties, shear resistance, column confinement, and ductility [14].

It is studied that the similitude characteristics are not similar for static and dynamic testing [15]. In another research, reinforced concrete columns were subjected to hysteretic load and the result was concluded that the hysteric response of deficient columns may be increased by CF sheet



FIGURE 6: Application of CFRP (HEX-103-C) to pier.

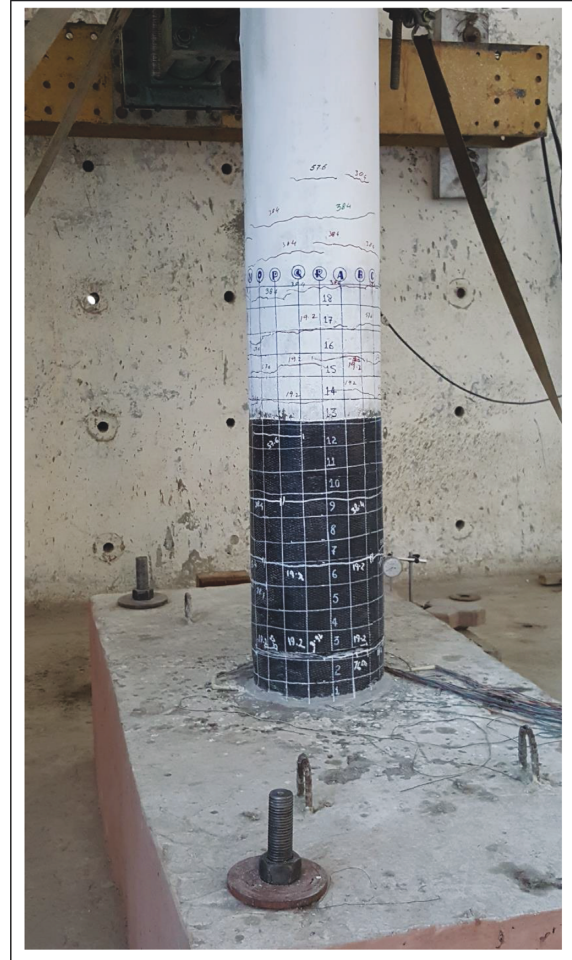


FIGURE 7: Testing of pier after the application of CFRP.

encasing being an efficient means to increase lateral confinement, strength, and ductility [16]. In a study, a crux of various analytical techniques for retrofitting in seismic regions by using FRP is presented [17]. In a research work, column samples were externally wrapped with carbon fiber-reinforced polymer and were having a continuous compressive force along with a lateral load to perform quasistatic cyclic testing. The outcomes established that confining application of CFRP totally improved the failure mechanism of those samples [7]. An extensive research was made on efficient rehabilitation techniques for structures damaged after a historic earthquake. During experimental work, eight low-strength scaled-down (4:1) piers were modeled and four of them were wrapped with CFRP. The quasistatic cyclic and free vibration tests were performed on these models to envisage CFRP wraps' behavior and effectiveness [2]. In another work, analytical simulation and analysis of LSC scaled-down models of bridge piers were conducted. Outcomes demonstrate that when columns are retrofitted prior to the damaged state, the ductility of columns is increased and their energy dissipation capacity effectively enhanced without noticeable loss in stiffness [18]. In other studies, the reliability analysis of CFRP-confined

concrete cylinders [19] and the performance of reinforced concrete circular columns wrapped with the CFRP and subjected to the axial load are represented very well with the analytical equations developed [20]. Similarly, the effect of CFRP, on seismic retrofit of short columns [7], on axial compressive strength [21], as a structural material [22], as an externally bonded reinforcement [23], on the behavior of inadequately detailed RC columns during an earthquake event [24], and on the residual performance of R.C. columns [25], has been studied by different researchers with promising results.

The bridges in the past have been constructed following WPCPHB1967. The concrete strength used in these structures was low to moderate level. Now with the implementation of the new building code with revised seismic provisions and modified seismic zonings, there is an immediate requirement to reinforce the standing bridge structures and especially their piers, being the most vulnerable parts of the structure, in order to resist more severe earthquake events. In a recent experiment [26] and numerical investigations [27], the energy dissipation behavior of HSC and CFRP retrofitted piers, which got damaged due to quasistatic loading, is presented. The current investigation has the main objectives to analyze and evaluate the lateral

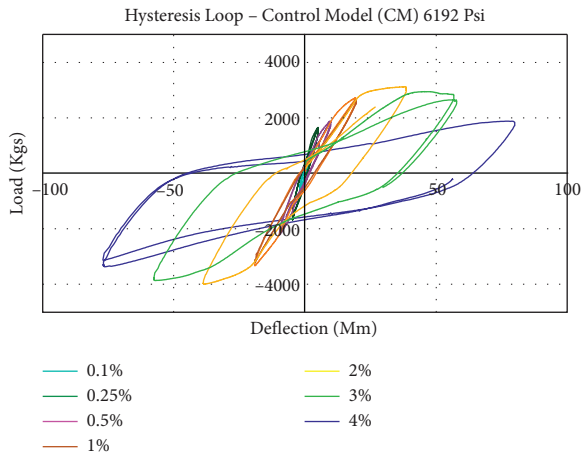


FIGURE 8: Hysteresis curves of the CM 6192 psi pier model subjected to different drift levels.

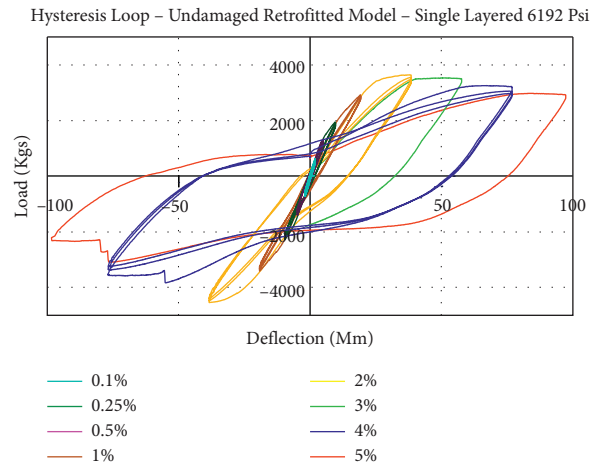


FIGURE 11: Hysteresis curves of the UDRM-SL 6192 psi pier model subjected to different drift levels.

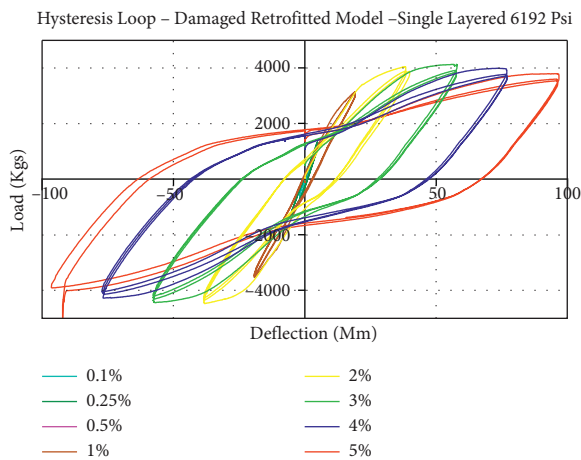


FIGURE 9: Hysteresis curves of the DRM-SL 6192 psi pier model subjected to different drift levels.

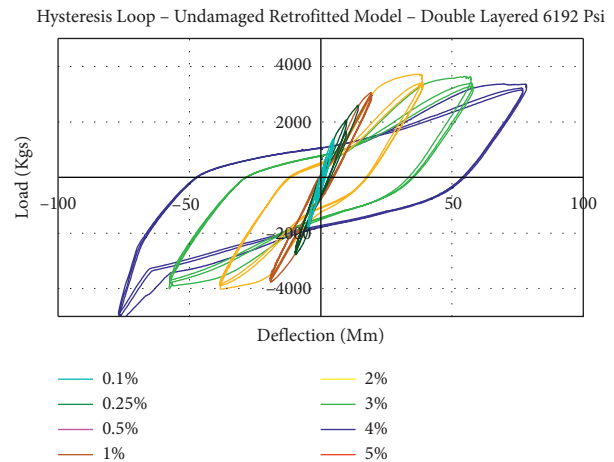


FIGURE 12: Hysteresis curves of the UDRM-DL 6192 psi pier model subjected to different drift levels.

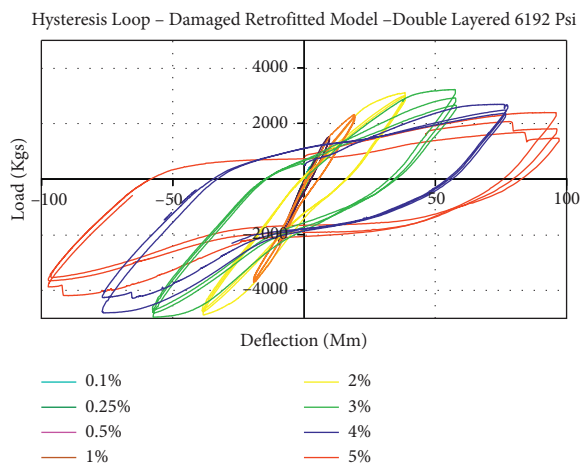


FIGURE 10: Hysteresis curves of the DRM-DL 6192 psi pier model subjected to different drift levels.

load carrying capacity, equivalent stiffness, and equivalent damping of HSC model bridge piers when these are provided with CFRP retrofitting. This investigation also presents the evaluation of the behavior of low-strength concrete (1800 and 2400 Psi) bridge piers viz, namely, a high-strength concrete (6192 Psi) in respect of load carrying capacity, equivalent stiffness, and equivalent damping. The investigation work on low-strength concrete has already been carried out vide references [2, 8, 18]. The experimental outcomes of these investigators were analyzed and compared with the results of the present study. This research also covers the numerical simulation and evaluation of HSC bridge models retrofitted with CFRP to find out its effectiveness in increasing the strength of the piers. A comparison of results of simulated models for both of high-strength and of low-strength concrete models with experimental results shows that they are in acceptable limits. The results clearly illustrate a noteworthy rise in load carrying capacity of high-

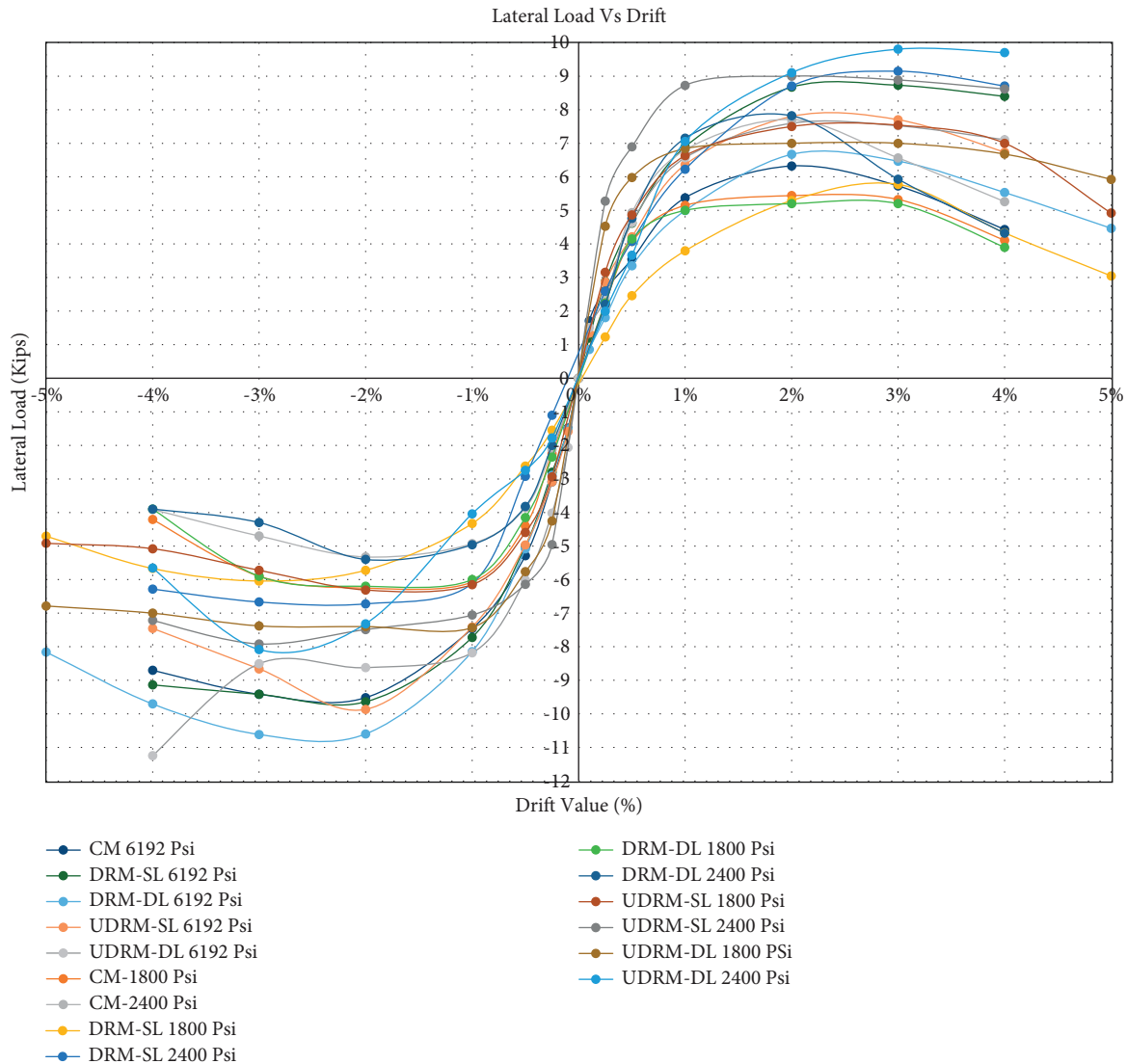


FIGURE 13: Lateral load vs drift: comparison of 6192 psi model backbone curves with those of similar work carried out by Ali [1] and Iqbal [2] with 1800 psi vs 2400 psi models.

strength concrete models, the minutiae of which are cited in subsequent sections.

2. Experimental Arrangement

All the experimental work was completed in the Civil Engineering Department of University of Engineering and Technology Peshawar, Pakistan, where satisfactory facilities and essential apparatus are available. The investigation work included quasistatic cyclic testing of Six (6) bridge pier samples with the following properties.

The model piers were prepared by scaling them down to 4:1 by similitude analysis [15] and then scheduled in experimentation as was performed by different researchers [1, 2]. These samples were having average concrete strength of 6192 psi. The steel used had 83000 psi yielding strength with an elastic modulus of 29,000,000 psi. A dead load of 42400 lbs was assembled on each prototype. The QSC test

was performed on each specimen. Polymer (CFRP) sheets labeled HEX 103-C with a 0.40 inch (1.016 mm) thick fabric, 153000 psi strength in tension, and modulus of elasticity of 9400000 psi were externally applied in lower 24 in each of the retrofitted model. The comprehensive experimental arrangement with all the geometric information is given in Figure 1.

The representative concrete cylinder samples were tested for compressive strength, whereas the QSC testing was performed on each pier sample. The enhancement of the properties due to retrofitting of these scaled-down models was envisaged. To better visualize these improvement effects, the following testing schedule was conceded:

- (a) Two HSC test samples were subjected to quasistatic cyclic loading tests with their unretrofitted state and were tested up to failure. These models are designated in the research as CM or control models.

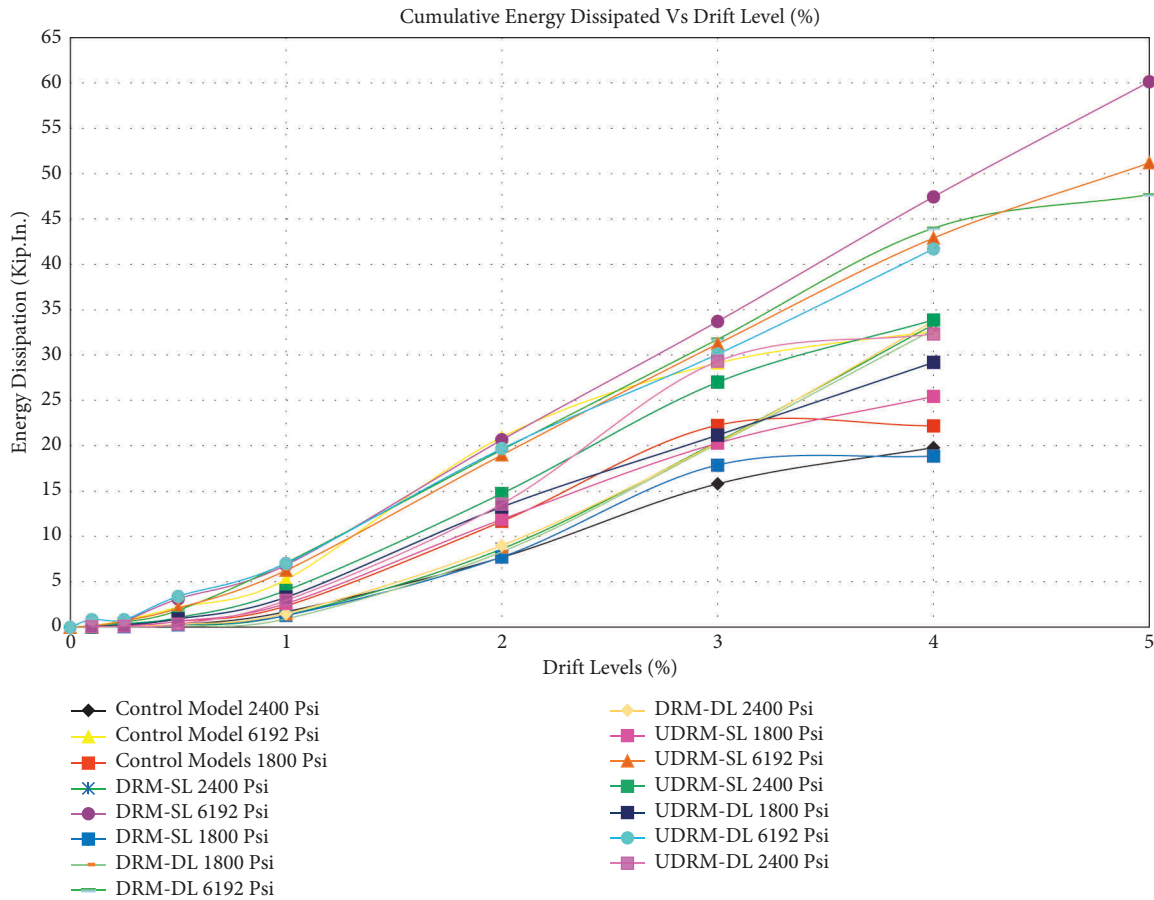


FIGURE 14: Cumulative energy dissipated vs drift—comparison of 6192 psi model curves [26] with those of similar work carried out by Ali [1] and Iqbal [2] with 1800 psi and 2400 psi models.

- (b) These cracked models were restored, which constituted repairing of cracks with the cementitious mix, restoring their shape and retrofitting with CFRP. For one model, single layer of CFRP was used for retrofitting, which is referred as damaged retrofitted model—single layer (DRM-SL), while for the second sample, double layer of CFRP was used for retrofitting, which is referred as damaged retrofitted model—double layer (DRM-DL). These two repaired and retrofitted models were subjected to QSCT up to failure. The tests were studied to assess strength, stiffness, and damping properties of the samples.
- (c) Two additional models prepared with similar high-strength concrete (6192 psi) were applied retrofitting sheets in their original/unspoiled state, and then, quasi-static cyclic tests were performed on them. A sample was wrapped with one sheet cover of CFRP, which is referred to as undamaged retrofitted model—single layer (UDRM-SL), while two CFRP sheet covers were applied to the other model, which is referred as undamaged retrofitted model—double layer (UDRM-DL).
- (d) QSCT was performed at different drift levels, i.e., 0 to 4% and 5% in some cases. The extent of 5% drift

involved depending upon the failure criteria set for the models and the safety concerns due to the presence of a dead load of 42400 lbs over the specimens of the small diameter of one foot only subjected to repeated reverse cyclic loading. Thus, a potential threat of an accident to the laboratory equipment and to the staff working in the laboratory was present. The safety measures were adopted accordingly.

- (e) After completion of QSCT on all the samples, IGOR Pro software was used to arrange the data recorded on the data logger in the format of spreadsheets.

The activities including test assembly setup, damaged column with cracks, and spalling of concrete, crack filling and repairing, preparation of surface, application of CFRP, and testing of the column after this application are illustrated in Figures 2–7, respectively. The cyclic lateral loading of the tests with the change in drift stages provided hysteresis curves for all the models. Hysteresis curves were separately shaped for each drift level, which are presented below in Figures 8–12. With the help of these hysteresis curves, backbone curves were generated.

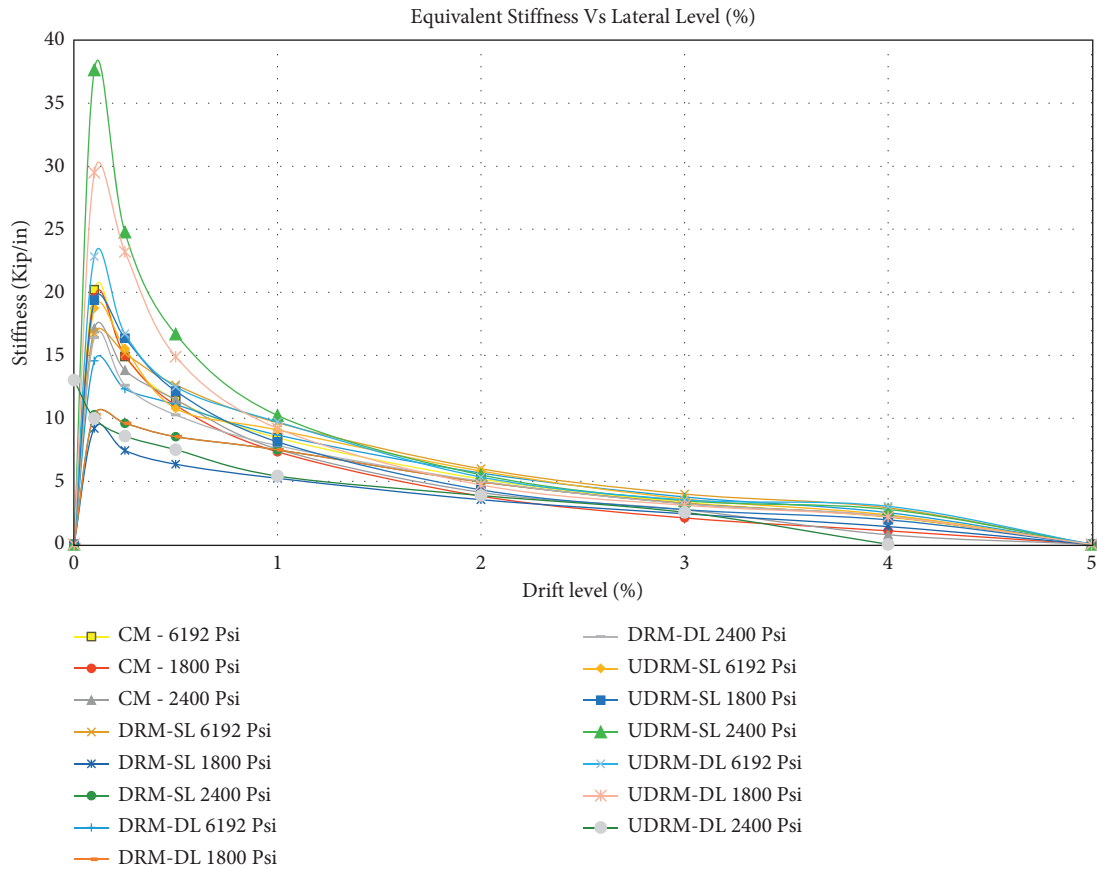


FIGURE 15: Equivalent stiffness vs drift—comparison of 6192 psi model curves with those of similar work carried out by Ali [1] and Iqbal [2] with 1800 psi and 2400 psi models.

3. Experimental Results

The statistics obtained from the investigational outcomes by the data collecting instrument data logger was analyzed with the help of a software named IGOR Pro, wherein it was organized in the form of spreadsheets and graphs were plotted. The number of tested specimens was six. The quasistatic cyclic load was applied to each sample with a varying range of drift increasing from 0% to 5%. The graphs accordingly portray the load carried/resisted by the model. The hysteresis curves are plotted by combining these graphs [26]. The peak value of each curve was marked and used to draw backbone curves. The backbone curves for representative control models, damaged retrofitted models, and undamaged retrofitted models for LSC (1800 psi and 2400 psi) were gained from previous work carried out by Ali [1], Khan et al. [8], and Iqbal [2] and have been analyzed in comparison with matching curves of HSC, i.e., 6192 psi (Figure 13).

The area under the hysteresis loop curves gives the value of energy dissipated. Energy dissipation values for different drift levels (0.1%, 0.25%, 0.5%, 1%, 2%, 3%, 4%, and 5%) for each model were the same as in recent research [26]. The energy dissipation values for control

models, damaged retrofitted models, and undamaged retrofitted models of HSC and those of LSC gained from previous work carried out by Ali [1] and Iqbal [2] were compared and analyzed [26] to investigate the improvements made by CFRP (Figure 14) and are replicated here for reference.

Herein CM = control model, DRM = damaged retrofitted model, UDRM = undamaged retrofitted model, SL = single layer, and DL = double layer.

Equivalent stiffness k_e (kip/in) and damping were also determined in this research. For this purpose, necessary calculations were made on Excel sheets. In these calculations, values of drift level, displacements, and push and pull forces were used, and relevant formulae for evaluating the equivalent stiffness and damping values were applied. Graphs were then plotted between different drift levels and equivalent stiffness and damping, respectively. Curves obtained for HSC (6192 psi) were then compared with LSC (1800 psi and 2400 psi) (Figures 15 and 16). It is noted that the stiffness values for UDRM-SL 2400 psi and UDRM-DL1800 psi are on the excessive side while others are in consistency. It was further noted that the value of equivalent damping increased with the increase in drift level while it is approximately in the same zone for high-strength concrete.

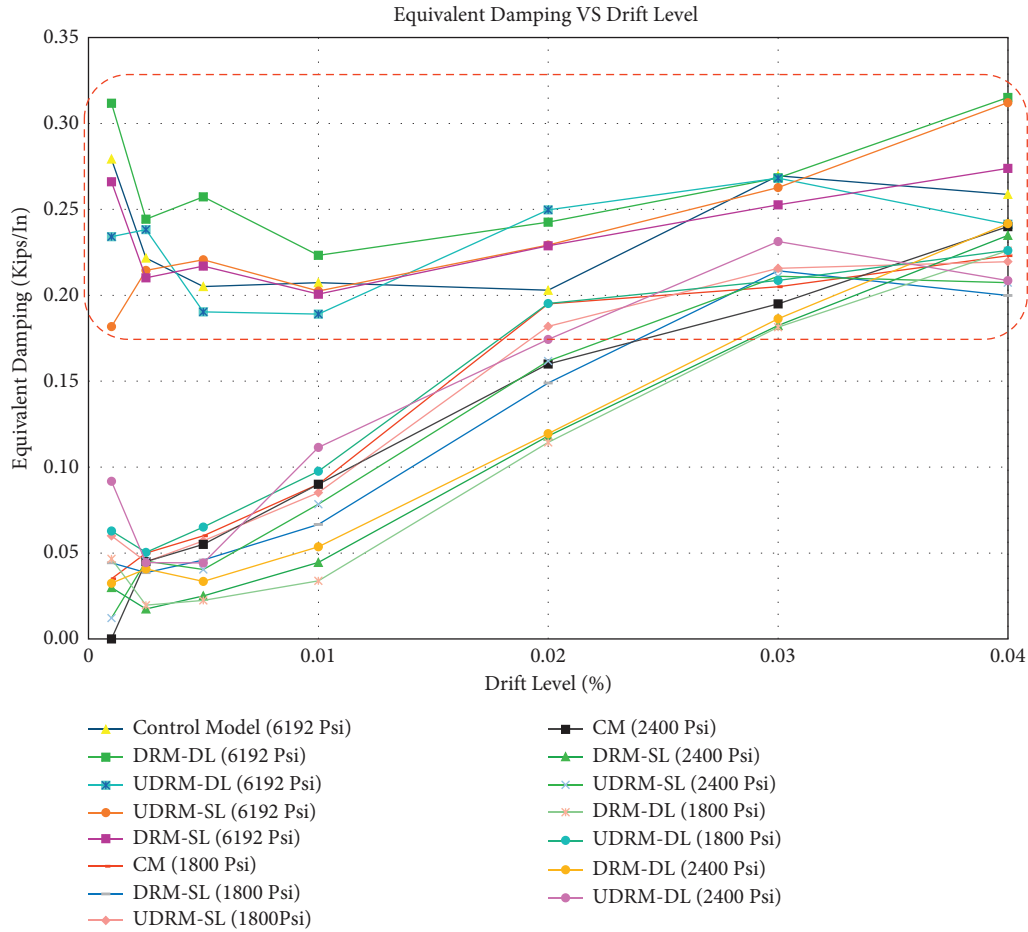


FIGURE 16: Equivalent damping vs drift—comparison of 6192 psi model curves with those of similar work carried out by Ali [1] and Iqbal [2] with 1800 psi and 2400 psi models.

TABLE 1: Material properties used in SiesmoStruct.

Description	Limits
<i>Unconfined concrete</i>	
Compressive strength (psi)	6192
Tensile strength (psi)	382
Strain at peak stress	0.0018
Confinement factor	1.0
<i>Steel reinforcement</i>	
Modulus of elasticity (psi)	29000000
Yield strength (psi)	83000
Fracture/buckling strain	0.067
<i>CRFP</i>	
Thickness (in)	0.04
Tensile strength (psi)	153000
Confinement factor	1.981
FRP jacket elastic modulus (psi)	9400000
FRP jacket ultimate strain	0.01
Radius of rounding corner (in)	1.50

It is obvious from the evaluation of different sets of high-strength concrete (6192 psi) models and their comparison with the corresponding single- and double-layered CFRP low-strength concrete models (1800 and 2400 psi) that the

rise in the strength of concrete substantially increased the load carrying capacity, equivalent stiffness, equivalent damping, and energy dissipation of the samples.

4. Numerical Simulation of Bridge Pier Models

The numerical modeling of the high-strength concrete bridge pier models for assessing their dynamic properties was also made. The hysteretic performance, the lateral stiffness, and damping properties were assessed for the columns wrapped with CFRP layers. The model geometry, different dimensions, type, and magnitude of applied loading were the same as considered in the experimental work. The control specimen was modeled and analyzed through the finite element method (FEM) using the “SeismoStruct” software. Then, the retrofitting of the specimen was modeled by encasing it with CFRP layers and it was analyzed again for assessing the effectiveness and performance of confined concrete. The software is capable of accounting for different sorts of nonlinearity. Quasistatic cyclic loading was stimulated through the static pushover analysis. A dead load of 42400 lbs was applied on the top of the model. The horizontal load generated on the round model was applied in the form of incremental drift stages

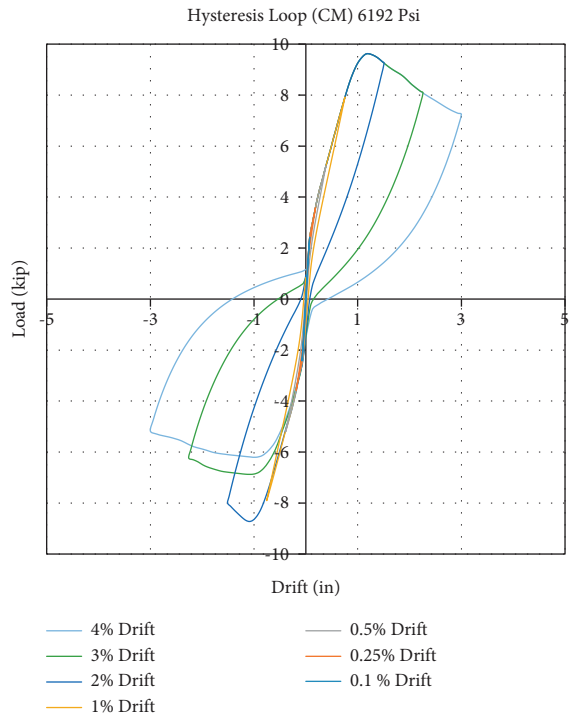


FIGURE 17: Hysteresis curve of control models (6192 psi).

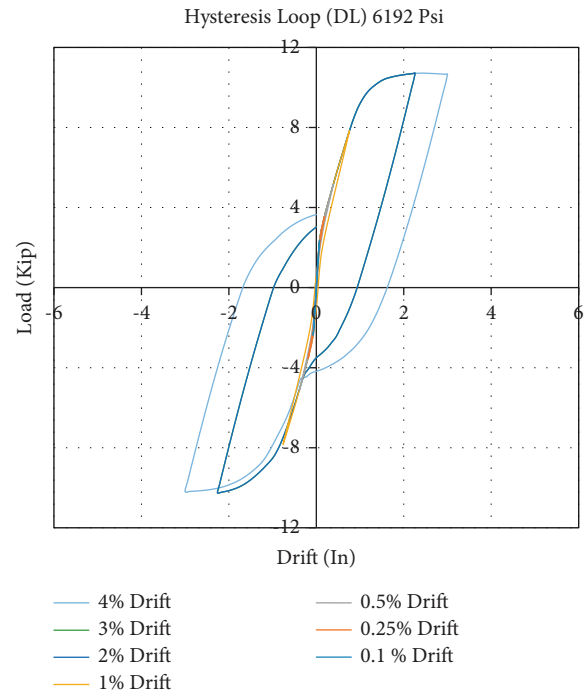


FIGURE 19: Hysteresis curve of double-layer models (6192 psi).

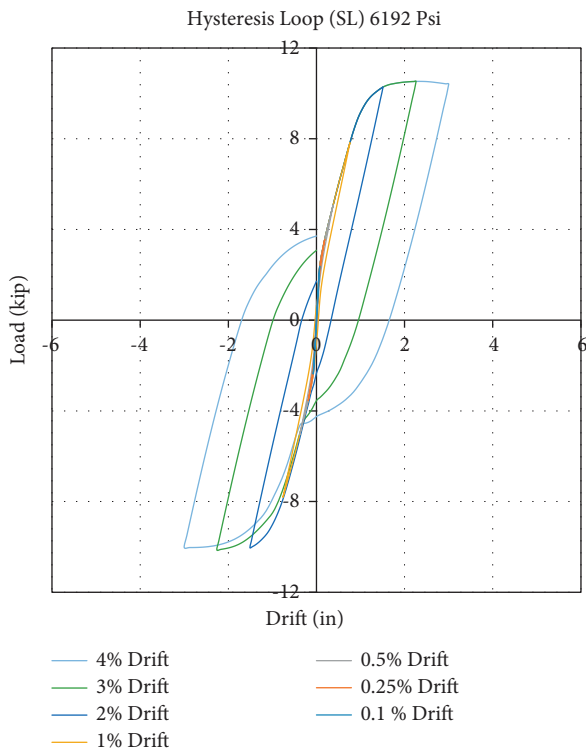


FIGURE 18: Hysteresis curve of single-layer models (6192 psi).

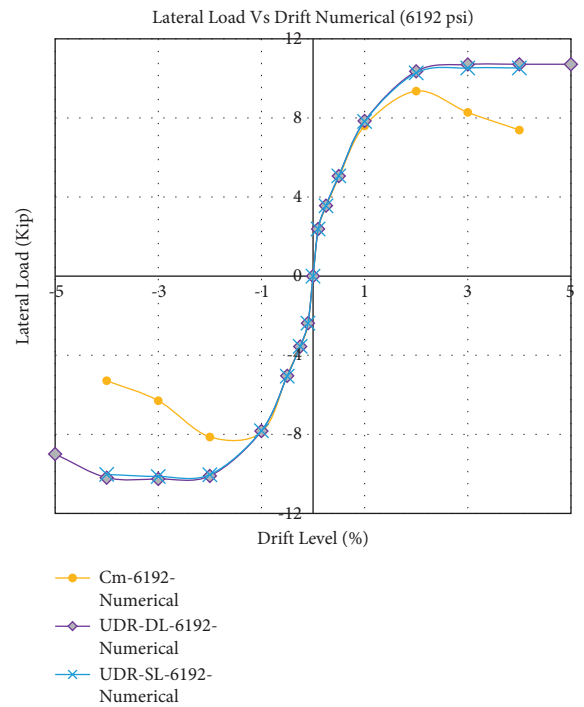


FIGURE 20: Comparison of lateral load vs drift (6192 psi).

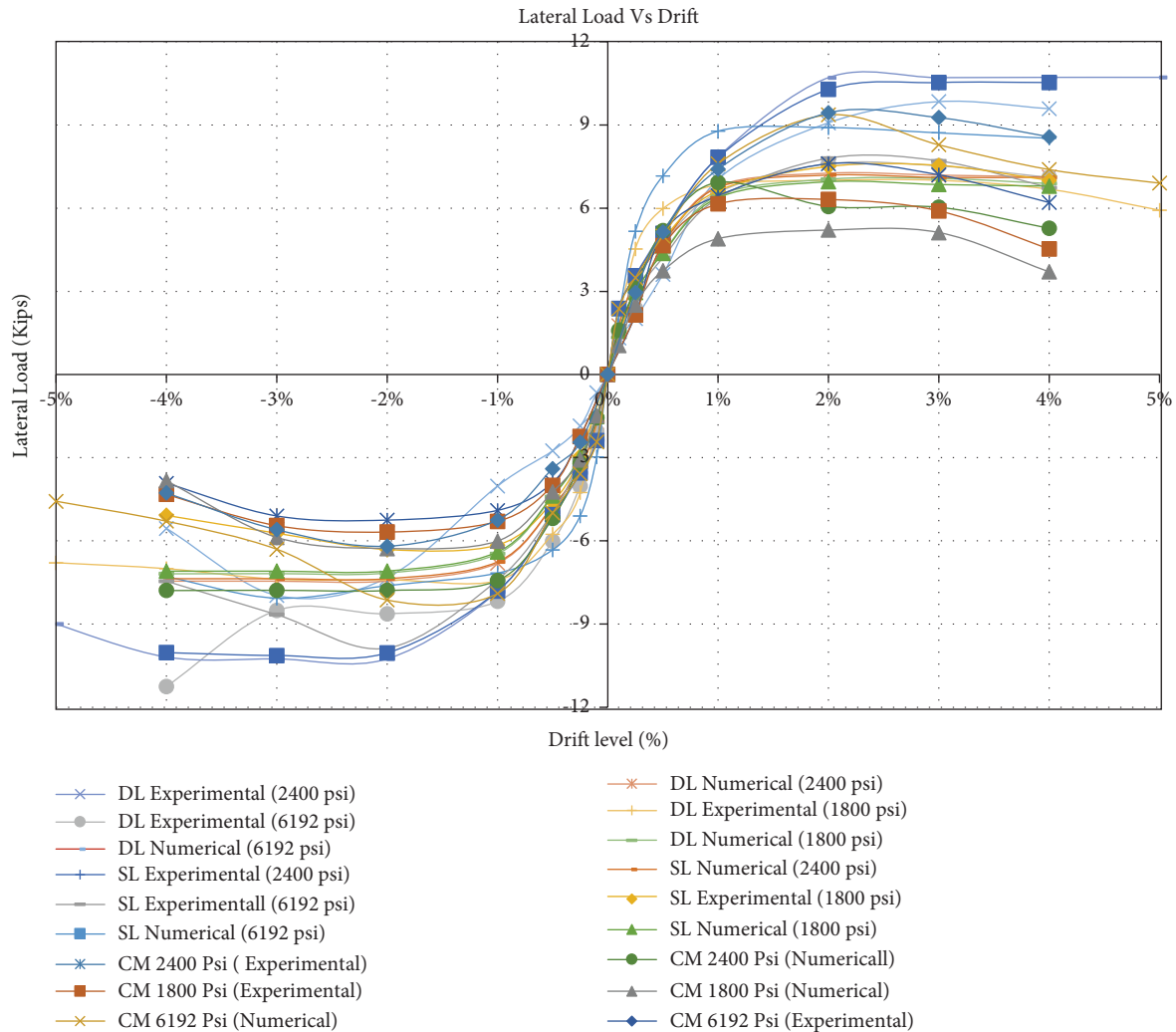


FIGURE 21: Lateral load vs drift—comparison of experimental vs numerical results.

on one specific track and then a returning force on the opposite path, thus establishing the hysteresis loop for every cycle.

Thirteen diverse features are present in SeismoStruct V6.5 to define material and loading conditions, which may be used by several methods to organize any number of materials and loads to be employed to the models. In the present research, the Mander et al. nonlinear concrete model (con_mat) was selected to describe the concrete in the core and in the cover while the pier was modeled as an inelastic force-based frame element type (infrmFB). Similarly, the steel was represented by the Menegotto–Pinto steel model (stl_mp). The parameters of nonlinear concrete material, the confinement factor, physical properties for the confined concrete model, and the type of element used for the model and the size element effect on the nonlinear behavior were based on the previous research conducted by the authors [18]. The properties of the materials considered in the software are arranged in Table 1.

5. SeismoStruct Results

Simulation of quasistatic cyclic load tests using pushover analysis was carried out. Subsequent to simulating the QSCL test, the accompanying actions were performed:

- The statistics obtained after the analysis of the model from SeismoStruct were rearranged in a manageable format and transferred to spreadsheets of Excel program.
- Hysteresis loop curves at various drift levels (in) against lateral load (kip) were individually plotted in Excel program. The damaged retrofitted model was not analytically analyzed; however, the curves for control model (CM), undamaged retrofitted model—single layer (UDRM-SL), and undamaged retrofitted model—double layer (UDRM-DL) for HSC have been displayed in Figures 17–19. The following information was derived from these curves:

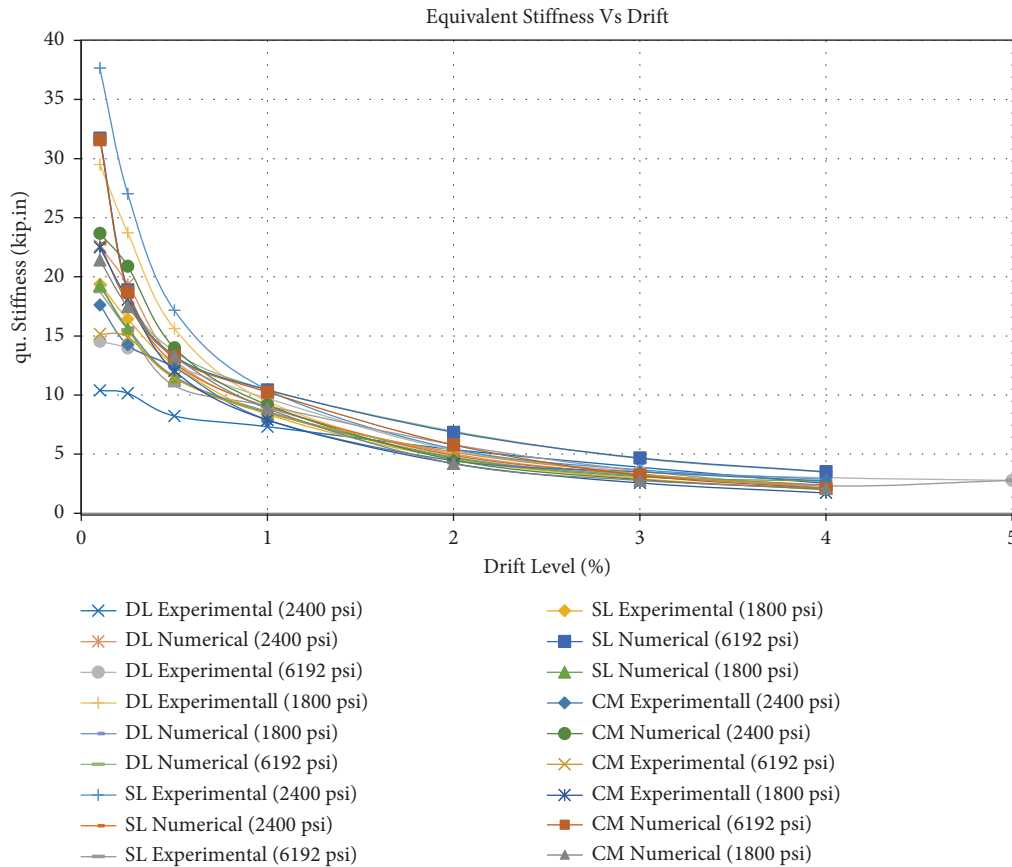


FIGURE 22: Equivalent stiffness vs drift—comparison of experimental vs numerical results.

- (i) Maximum lateral load/strength of the column at each drift stage
 - (ii) Equivalent stiffness
 - (iii) Equivalent damping
- (c) For the respective drift levels, curves were drawn for ultimate lateral loads for each drift value, as backbone curves, and are shown in Figures 20 and 21. The values for equivalent stiffness and equivalent damping were calculated in the same manner as in the experimental work and graphs, and Figures 22 and 23, respectively, are also plotted. The values for energy dissipation have been taken from recent research by Mustahsan [27] and reproduced here in Figure 24 for reference.

These curves of the control model (CM), undamaged retrofitted model—single layer (UDRM-SL), and undamaged retrofitted model—double layer (UDRM-DL) of HSC piers were compared with those of LSC specimens of the experimental work mentioned in this research and earlier research works [1, 2, 26] and earlier numerical works [18, 27] and checked for the increase with reference to the control models.

6. The Discussion on the Results

After the detailed study of experimental and numerical results discussed above, the following are the main outcomes:

- (i) The percent increase in lateral load carrying capacity, equivalent stiffness, and damping in experimental results of the **DRM-SL and DL** and **UDRM-SL and DL** above those of **CM** for HSC 6192 Psi models is presented in Table 2.

A comparison of column #3 and column #4 of Table 2 reveals that for high-strength concrete the application of a single layer of CFRP is more efficient. Figure 16 demonstrates that the equivalent damping value remained approximately the same for high-strength concrete.

- (ii) The summary of the experimental results of CM and DRM-SL and DL and UDRM-SL and DL of HSC 6192 Psi and of corresponding models of LSC (1800 and 2400 psi) in comparison of percent increase for lateral load carrying capacity, equivalent stiffness, and damping is given in Table 3.

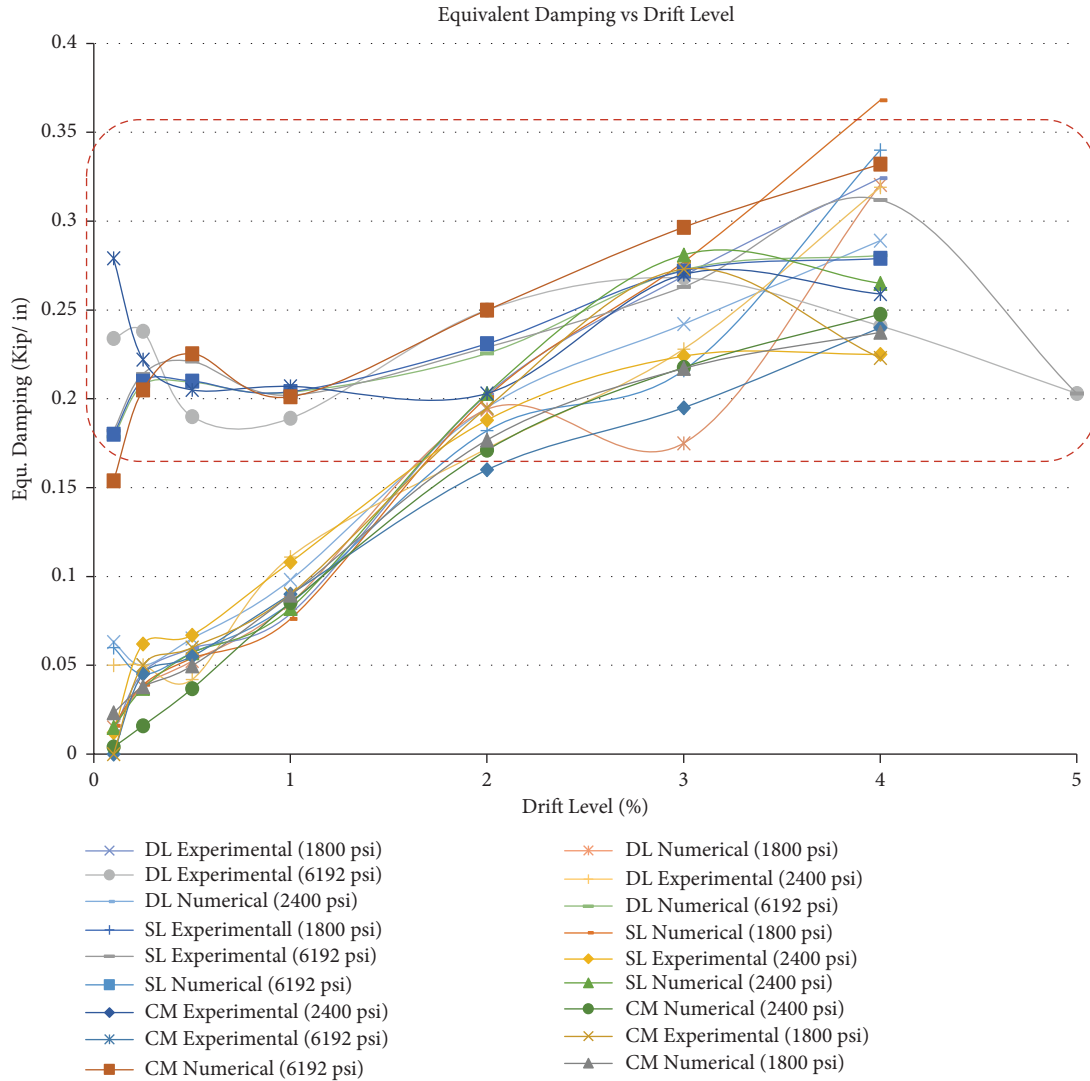


FIGURE 23: Equivalent damping vs drift—comparison of experimental vs numerical results.

Columns #3 and #8 of Table 3 exhibit the increase in properties on the increase of strength only. A comparison of column #3 and #4 of Table 3 with column #4 and #5 and #11 of the same table, respectively, shows that the increase in properties is more prominent in 1800psi models, i.e., in low-strength columns.

Figure 16 further demonstrates that the value of equivalent damping increases with the increase in lateral drift for low-strength concrete models.

- (iii) The comparison of numerical results of the control models (CM) and undamaged retrofitted models (UDRM)-SL and DL of HSC 6192 Psi for the percent increase of lateral load carrying capacity, equivalent stiffness, and damping is summarized here under in Table 4. Figure 23 further demonstrates that the equivalent damping value remained approximately the same for high-strength concrete.

- (iv) The summary of the numerical results of CM and of SL and DL of HSC 6192 Psi and of corresponding models of LSC (1800 and 2400 psi) in comparison to percent increase for lateral load carrying capacity, equivalent stiffness, and damping is here under in Table 5.

The numerical analysis results are steady when compared with the experimental results due to the assumptions and parameters selected for analysis devised by different researchers. The results of the recent research studies [26, 27] also give the same trends. Figure 23 further demonstrates that the value of equivalent damping increases with the increase in lateral drift for low-strength concrete models. The percent increase in values above control model in low-strength concrete (1800 psi and 2400 psi) samples is more prominent as compared to their improvement in high-strength concrete (6192 Psi).

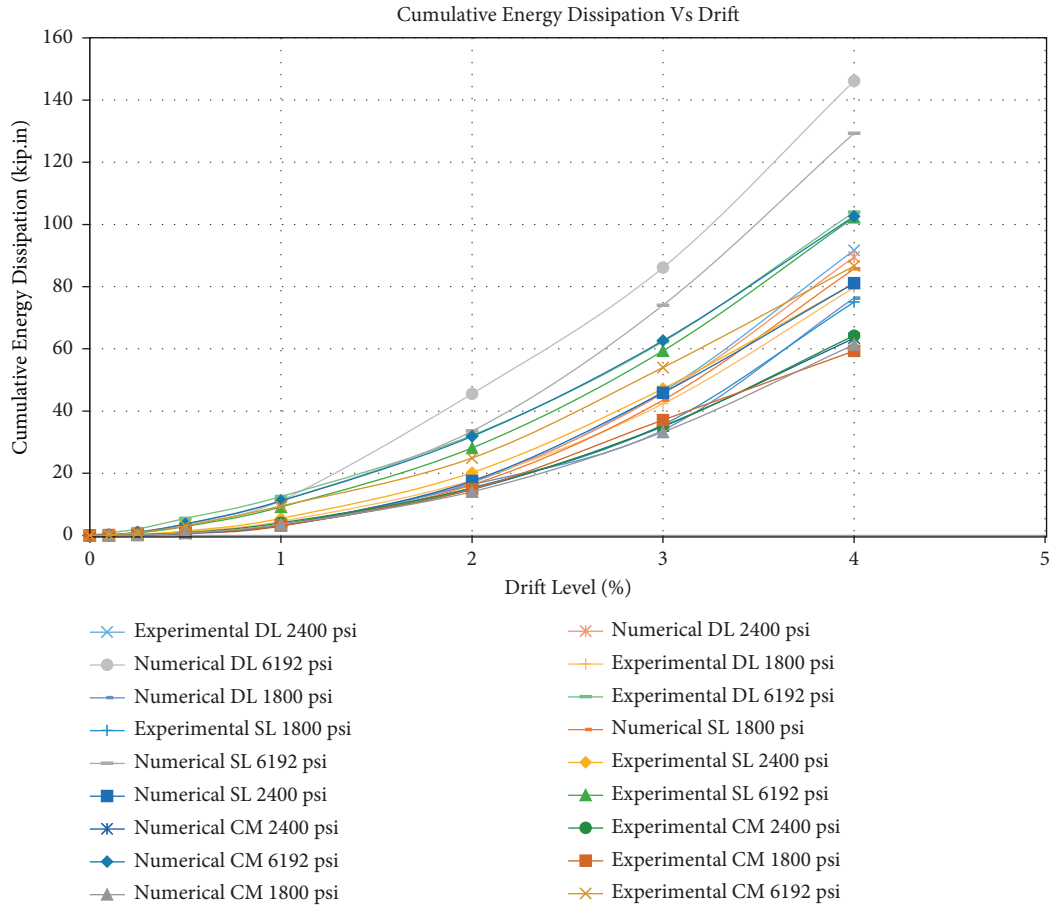


FIGURE 24: Cumulative energy dissipation vs drift—comparison of experimental vs numerical results.

TABLE 2: Percent increase above control model for HSC 6192 psi models in experimental results.

Sr. no.	Property	DRM-SL	DRM-DL	UDRM-SL	UDRM-DL
1	2	3	4	5	6
1	Lateral load carrying capacity	15.96	09.11	11.51	18.95
2	Equivalent stiffness	34.637	17.01	8.59	40.45
3	Equivalent damping	-1.93	12.85	11.78	-3.97

TABLE 3: Percent increase above control model for HSC 6192 vs 1800psi and 2400psi models in experimental results.

Sr. no.	Property	CM 6192 vs- 1800	UDRM-SL 6192 vs- 1800	UDRM-DL 6192 vs- 1800	DRM-SL 6192 vs- 1800	DRM-DL 6192 vs- 1800	CM 6192 vs- 2400	UDRM-SL 6192 vs- 2400	UDRM -DL 6192 vs- 2400	DRM-SL 6192 vs- 2400	DRM-DL 6192 vs- 2400
1	2	3	4	5	6	7	8	9	10	11	12
1	Lateral load carrying capacity	35.45	27.54	30.56	55.46	51.61	21.52	04.42	05.33	15.74	30.47
2	Equivalent stiffness	46.07	20.21	38.07	105.44	08.67	41.26	03.52	09.91	25.04	11.59
3	Equivalent damping	25.22	42.18	18.59	27.22	39.43	16.35	47.89	28.61	16.61	30.39

TABLE 4: Percent increase above control model for HSC 6192 psi models in numerical results.

Sr. no.	Property	UDRM-SL	UDRM-DL
1	2	3	4
1	Lateral load carrying capacity	16.32	18.04
2	Equivalent stiffness	4.61	4.52
3	Equivalent damping	05.88	05.65

TABLE 5: Percent increase above control model for HSC 6192 vs 1800psi and 2400psi models in numerical results.

Sr. no.	Property	CM 6192 vs- 1800	UDRM-SL 6192 vs- 1800	UDRM-DL 6192 vs- 1800	CM 6192 vs- 2400	UDRM-SL 6192 vs- 2400	UDRM-DL 6192 vs- 2400
1	2	3	4	5	6	7	8
1	Lateral load carrying capacity	31.75	48.20	47.01	35.26	43.22	43.20
2	Equivalent stiffness	43.25	60.19	62.40	31.05	40.08	40.70
3	Equivalent damping	86.92	19.53	37.31	92.86	63.93	36.50

7. Conclusions

Upon comparison of the experimental and numerical results of control models and CFRP wrapped LSC models (1800 and 2400 Psi) and CFRP wrapped HSC models (6192 psi) for lateral load carrying capacity, stiffness, and damping, it is concluded that

- (i) All the properties effectively improve with the increase in the strength of concrete
- (ii) The retrofitting significantly enhances all the properties of the piers
- (iii) The effect of retrofitting is more prominent in case of concrete with low strength due to its effectiveness in the confinement
- (iv) The outcome of double layer of CFRP sheets is more significant in low-strength concrete
- (v) The result of single layer of CFRP retrofitting is more prominent in high-strength concrete
- (vi) The effect of CFRP retrofitting is steady in numerical modeling as compared to that of the experimental results
- (vii) The value of equivalent damping increases with the increased lateral drift for low-strength concrete models while it remained approximately the same for high-strength concrete prototypes

Therefore, it may be concluded that a significant enhancement in lateral load carrying capacity, equivalent stiffness, and equivalent damping is noticed in the HSC models when compared to those of LSC. This improvement is further enriched when HSC models are retrofitted. The numerical analysis further supports the experimental results.

The existing bridges made of low- and high-strength concrete need structural improvements after the revision of relevant seismic zones to comply with the revised seismic provisions. When retrofitted with CFRP sheets, the bridge piers showed a considerable growth in lateral strength, ductility, stiffness, and energy absorption as evident from the

results of this research. This will enable the bridge structure to withstand high-intensity future earthquakes and lessen their vulnerability against prospective damages. Therefore, it is suggested that the available bridge stock may be checked for the capacity of their piers to meet with the seismic demand and may be retrofitted with CFRP to comply with the contemporary seismic zoning requirements instead of their replacement with new structures.

Data Availability

Data supporting the results of this study are available with the corresponding author.

Conflicts of Interest

The authors declare that they have no conflicts of interest.

Acknowledgments

The authors would like to thank Engr. Obaid Shahid Mir, Engr. Mustahsan, and Engr. Dr. Adeel Mehmood who helped throughout the research work, particularly the staff of Civil Engineering Department UET Peshawar for their help and guidance in performing the test at this facility. The diligent evaluation and productive recommendations and observations by the unknown referees are thankfully admitted.

Supplementary Materials

The energy dissipation, equivalent stiffness, and damping were calculated in Excel sheets using relevant equations. The necessary calculation notes (Appendix A) describing the procedure used here with sample calculation sheets as Appendices B and C along with supporting Graph 1 for 1% drift for DRM-SL have been added for ready reference. (*Supplementary Materials*)

References

- [1] S. M. Ali, "Study of energy dissipation capacity of RC bridge columns under seismic demand," 2009, <http://173.208.131.244:9060/xmlui/handle/123456789/4742>.
- [2] M. Iqbal, *Evaluation of Retrofitted Bridge Piers under Seismic Loading*, Dissertations. PhD, 2012.
- [3] H. Saadatmanesh, M. Ehsani, and L. Jin, "Seismic strengthening of circular bridge pier models with fiber composites," *ACI Structural Journal*, vol. 93, pp. 639–647, 1996.
- [4] M. Saafi, H. Toutanji, and Z. J. Li, "Behavior of concrete columns confined with fiber reinforced polymer tubes," *ACI Materials Journal*, vol. 96, pp. 500–509, 1999.
- [5] T. Alkhrdaji and A. Nanni, "Flexural strengthening of bridge piers using FRP composites," *Structures Congress*, 2000.
- [6] A. A. Mortazavi, K. Pilakoutas, and K. S. Son, "RC column strengthening by lateral pre-tensioning of FRP," *Construction and Building Materials*, vol. 17, no. 6-7, pp. 491–497, 2003.
- [7] F. Colomb, H. Tobbli, E. Ferrier, and P. Hamelin, "Seismic retrofit of reinforced concrete short columns by CFRP materials," *Composite Structures*, vol. 82, no. 4, pp. 475–487, 2008.
- [8] Q. U. Z. Khan, M. Fiaz Tahir, A. Ahmad, and M. Iqbal, "Seismic evaluation of repaired and retrofitted circular bridge piers of low-strength concrete," *Arabian Journal for Science and Engineering*, vol. 40, no. 11, pp. 3057–3066, 2015.
- [9] K. E. Xiaojun, C. Zongping, X. Jianyang, and Y. Wudang, "Experimental Study on Seismic Performance of High-Strength concrete Short Columns with Different Strengthening Measures," *Journal of Building Structures*, vol. 34, 2013.
- [10] M. Zarei, "Normal-strength and high-strength concrete columns under cyclic axial load and biaxial moment," *Dissertations*, vol. 65, 2016.
- [11] E. Del Rey Castillo, J. Ingham, and M. Griffith, "Seismic Strengthening of RC Columns with Straight FRP Anchors," in *Proceedings of the 13th International Symposium on Fiber-Reinforced Polymer Reinforcement for Concrete Structure (FRPRCS-13)*, Anaheim, California, October 2017.
- [12] W. Aules, "Behavior of Non-ductile Slender Reinforced Concrete Columns Retrofit by CFRP under Cyclic Loading," Portland State University, Portland, Oregon, Doctor of Philosophy, 2019.
- [13] A. Zerkane, Y. Saeed, and F. Rad, "Cyclic Loading Behavior of CFRP-Wrapped Non-ductile Beam-Column Joints," in *Proceedings of the Concrete Convention and Exposition - American Concrete Institute*, Detroit, MI, USA, February 2019.
- [14] R. Artur, B. Julijana, B. Jordan, and T. Zoran, "Quasi-static tests on RC building columns strengthened with CFRP," *Građevinar*, vol. 73, 2021.
- [15] A. M. Syed, "Similitude analysis of concrete scaled bridge columns for quasi-static and free vibration testing," *IOSR Journal of Mechanical and Civil Engineering*, vol. 3, no. 6, pp. 42–48, 2012.
- [16] K. Kawashima, M. Hosotani, and K. Yoneda, "Carbon fiber sheet retrofit of reinforced concrete bridge piers," in *Proceedings International Workshop on Annual Commemoration of Chi-Chi Earthquake, Vol. II Technical Aspect, National Center for Research on Earthquake Engineering*, pp. 124–213, Taipei, Taiwan, ROC, January 2000.
- [17] A. Prota, G. Manfredi, F. Ceroni, and M. Pecce, *Influence of FRP Jackets on Stress Transfer between Steel Rebars and concrete*, Japan concrete institute, Tokyo, Japan, 2001.
- [18] J. B. Mander, M. J. N. Priestley, and R. Park, "Theoretical stress-strain model for confined concrete," *Journal of Structural Engineering*, vol. 114, no. 8, 1988.
- [19] A. Ahmad, Q. u Z. Khan, and A. Raza, "Reliability analysis of strength models for CFRP-confined concrete cylinders," *Composite Structures*, vol. 244, Article ID 112312, 2020.
- [20] C. Chastre and M. A. G. Silva, "Monotonic axial behavior and modelling of RC circular columns confined with CFRP," *Engineering Structures*, vol. 32, no. 8, pp. 2268–2277, April 2010.
- [21] M. R. Esfahani and M. R. Kianoush, "Axial compressive strength of reinforced concrete columns wrapped with fiber reinforced polymers (FRP)," *IJE Transaction B, Applications*, vol. 18, pp. 9–13, 2005.
- [22] M. N. Fardis and H. H. Khalili, "FRP-encased concrete as a structural material," *Magazine of Concrete Research*, vol. 34, no. 121, pp. 191–202, 1982.
- [23] Fib, *Externally bonded FRP reinforcement for RC structures*, Federation International du Berton, 2001.
- [24] O. Ozcan, B. Binici, and G. Ozcebe, "Improving seismic performance of deficient reinforced concrete columns using carbon fiber-reinforced polymers," *Engineering Structures*, vol. 30, no. 6, pp. 1632–1646, 2008.
- [25] R. Perera, "A numerical model to study the seismic retrofit of RC columns with advanced composite jacketing," *Composites Part B: Engineering*, no. 4-5, pp. 337–345, 2006.
- [26] O. Shahid Mir, M. Khalid Hafeez, and Qaiser-Uz-Zaman, "Investigation of high strength concrete bridge piers retrofitted with CFRP under seismic loading," in *Proceedings of the 1st International Conference on Advances in Civil & Environmental Engineering*, Feb 2022.
- [27] M. Iqbal, M. Khalid Hafeez, and Qaiser-Uz-Zaman, "Numerical investigation of typical scale down bridge pier retrofitted with CFRP under seismic loading," in *Proceedings of the 1st International Conference on Advances in Civil & Environmental Engineering*, Feb 2022.

Research Article

Autonomous Classification and Decision-Making Support of Citizen E-Petitions Based on Bi-LSTM-CNN

Fengmei Sun ¹ and Yi Zuo ^{2,3}

¹Collaborative Innovation Center for Transport Studies, Dalian Maritime University, Dalian 116026, China

²Collaborative Innovation Center of Maritime Big Data & Shipping Artificial General Intelligence, Navigation College Dalian Maritime University, Dalian 116026, China

³The Research Institute for Socionetwork Strategies, Kansai University, Osaka 5648680, Japan

Correspondence should be addressed to Yi Zuo; zuo@dlmu.edu.cn

Received 27 May 2022; Revised 12 August 2022; Accepted 22 August 2022; Published 16 September 2022

Academic Editor: Toqeer Mahmood

Copyright © 2022 Fengmei Sun and Yi Zuo. This is an open access article distributed under the Creative Commons Attribution License, which permits unrestricted use, distribution, and reproduction in any medium, provided the original work is properly cited.

The increasing number of e-petition services requires accurate calculation methods to perform rapid and automated delivery. Automated text classification significantly reduces the burden of manual sorting, improving service efficiency. Moreover, existing text classification methods focus on improving sole models with an insufficient exploration of hybrid models. Moreover, existing research lacks combinatorial model selection schemes that yield satisfactory performance for petition classification applications. To address these issues, we propose a hybrid deep-learning classification model that can accurately classify the responsible department of a petition. First, e-petitions were collected from the Chinese bulletin board system and then cleaned, segmented, and tokenized into a sequence of words. Second, we employed the word2vec model to pretrain an embedding matrix based on the e-petition corpus. An embedding matrix maps words into vectors. Finally, a hybridized classifier based on convolutional neural networks (CNN) and bidirectional long short-term memory (Bi-LSTM) is proposed to extract features from the title and body of the petition. Compared with baseline models such as CNN, Bi-LSTM, and Bi-LSTM-CNN, the weighted *F1* score of the proposed model is improved by 5.82%, 4.31%, and 1.58%, respectively. Furthermore, the proposed automated petition classification decision support system is available on the e-petition website and can be used to accurately deliver petitions and conduct citizen opinion analysis.

1. Introduction

Online applications of e-government have been increasingly applied to pursuing citizen demand and government regulations that allow citizens to interact efficiently with government agencies. One of the most widely used e-government applications is e-petition, which enhances the communication of citizens with functional departments [1]. Recently, the burden of e-petition delivery has grown, and the number of messages has significantly increased from hundreds per week to thousands per day for government offices [2, 3]. According to the Shanghai Municipal Bureau of Petition in China, over 69,000 public opinions and suggestions were received and handled in 2021, with a

monthly average of 5,750 cases and an average public response rate of 79.08% in each district. Also, 49,554 petitions have been received from January to April 2022, with the number of petition submissions increasing rapidly and the daily response rate dropping to below 70%.

The government requires the ability to automatically determine the content of these petitions to reduce this burden. Alternatively, the exponential growth of easily accessible text data has led to a surge of research interest in automated content methods, such as automated text classification (ATC) [4, 5]. ATC is a subfield of natural language processing (NLP) that assigns documents to one or more prespecified categories, while these texts are usually unstructured [6, 7]. Large amounts of e-petition data are

publicly available. These data are novel in their availability and high storage volume, not widely used for research purposes [8]. ATC might offer an effective solution to address automated e-petition deliveries. However, selecting an accurate and efficient model is a challenge for current applications [9].

In traditional text classification research, classical classifiers include support vector machines (SVM) [10, 11], k-nearest neighbor (KNN) [12], and naive Bayes (NB) [13]. However, these methods cannot extract contextual relationships between words and text [5]. Since the concept of deep learning was proposed in 2006 [14], Kim [15] first proposed a text-based convolutional neural network (Text-CNN). The model performance was verified on seven short-text data sets with an average length of below 25. The outstanding performance of convolutional neural network (CNN) in short-text classification is attributed to the local correlation captured by the convolution and pooling operations. The limitation of CNN lies in the loss of structural information in maximum pooling; therefore, finding complex patterns such as adversative relations in long texts is difficult. Subsequently, a recurrent neural network (RNN) was applied to extract global semantic information from texts, which is suitable for time-series analyses such as text classification [16]. Long short-term memory (LSTM) is a special type of RNN. LSTM effectively solves the problems of long-term memory dependence and gradient disappearance in backpropagation and is more effective in processing chapter-level texts [17]. As an improvement of LSTM, bi-directional long short-term memory (Bi-LSTM) has forwarding and backward directions, which excels in extracting context features [18]. Improvements in these text classification models focus more on the network structure, activation function, etc. [19–22]. As deep learning models alone cannot improve classification performance, several scholars have proposed hybridized models [6, 23, 24]. The hybridized model takes advantage of each other to improve the accuracy of text classification. However, no single model is generic for all tasks, and different types of models are useful for specific domains [25]. Modeling unstructured text to achieve automated classification is a challenging task; for instance, a submitted e-petition contains two parts: title and body. Furthermore, the text length varies considerably, so extracting features using a unified method is ineffective.

To address this issue, this study proposes a hybrid autonomous classification method for e-petitions based on Bi-LSTM and CNN and integrates the rich information of the petition text to solve the decision-making support of the autonomous transmission of e-petitions. The proposed hybrid model combines the CNN and LSTM algorithms. The preprocessed title and body of the petition were input in parallel and represented as word embeddings. Then, a CNN with a small convolution kernel captures local features of the concise title, whereas Bi-LSTM-CNN extracts complex semantic features of the complex body. These two features were concatenated to form a unified representation and provide information for classification. To verify the performance of the proposed method, we collected e-petitions from the Chinese bulletin board system (BBS). The

numerical results show that the proposed method achieved the highest weighted precision (0.8288) and weighted recall (0.8262). The *F1* score reached 0.8267, which was higher than that of the baseline models. In addition, we also found that the classification effect of the model using the CNN structure to extract the features of the title was better than that of the model using the LSTM structure. The proposed model can effectively solve the problems of inconsistent text lengths and difficulty in feature extraction. The contributions of this study are twofold. First, it proposes a hybrid deep learning model incorporating title and body features, which is more adaptable to text classification tasks with more information than existing neural network structures. The second is the decision support system, which helps citizens automatically select the responsible department and to provide references for staff to judge petition demands. These two improvements significantly increase the efficiency and effectiveness of the petition workflow.

The remainder of this study is organized as follows. Section 2 reviews related studies on ATC and their applications. In Section 3, we introduce the methodological idea and the proposed classification model. The numerical experiments are presented in Section 4, and we conclude the study in Section 5.

2. Research Background and Literature Review

2.1. Related Studies of Automated Text Classification. Recently, ATC has attracted considerable attention from researchers in NLP. ATC techniques have developed rapidly and profoundly with the support of a large-scale research community. Table 1 lists several advanced studies on text-classification techniques.

Machine learning is considered superior to dictionary-based text classification methods [5]. Traditional machine learning models are widely used in various small-scale text classification tasks, owing to their simple implementation and high interpretability. The corpus size is usually above 10,000, and traditional text representation is high dimensional and highly sparse with weak feature representation, which usually requires additional feature engineering. SVM can effectively pursue two main properties of textual data: high dimensionality and sparsity [11]. However, an SVM requires extensive storage space and training time when the data volume is large [10]. Classic models are adept at solving the problem with strong individual signal words; they may make the classification insufficient because of ignorance of the interaction between words [12, 13].

Deep learning solves the limited representation of complex functions in previous shallow-structured algorithms and has become the mainstream research method in text classification [14]. A CNN has achieved significant success in image classification. The convolutional kernel extracts multidimensional features by setting different weights to obtain local key information through the pooling layer. A CNN enables fast dimensionality reduction and relatively few training parameters through its unique network structure and weight-sharing strategy [28]. Recently, CNN has been applied to various NLP tasks [29] and has

TABLE 1: Advanced studies on text classification techniques.

Model	Data set	Training set	Classes	Text length	Vocab
SVM [11]	Newspaper	250	2	500	11672
KNN [12]	Newspaper	4731	87	1000	10000
CNN [15]	Customer reviews	12700	3	16	13612
CNN [26]	Twitter	1600000	2	60	76643
LSTM [17]	Newspaper articles	8552	2	339	-
Bi-LSTM [18]	Service documents	9121	10	128	-
CNN + LSTM [6]	Clinical notes	26363	50	200	49354
LSTM-CNN [27]	Newspaper	50000	10	100	-

been extended to Text-CNN, which has several convolutional windows of varied sizes and has an excellent classification effect in the short-text classification task [15, 26]. CNN cannot effectively capture long-term context information between discontinuous words, which is important in text models [30]. To solve this limitation, RNN and LSTM can efficiently explore the potential semantic information of text, and LSTM is more common in long texts [17]. Bi-LSTM has two parallel layers that propagate in both forward and backward directions to fully capture dependencies in the context [18]. However, the accuracy of LSTM is further hampered by the inability to identify the different relationships between the various parts of the document [24]. In addition, CNN can be efficiently computed in parallel, whereas LSTM is less efficient than CNN because of the sequence dependencies problems in transmission [6, 25].

To improve classification, some researchers have proposed hybrid neural networks that combine CNN and LSTM algorithms. The convolution and pooling operations of CNN help the model extract locally salient features, whereas LSTM solves the long-sentence dependency problem by using a gate control mechanism to extract more complex contextual information [6, 31]. Regarding the hybrid model, attention should be paid to the organization of the structure [24]. The model structure design depends on the nature of the problem, and the data researched in the existing literature are derived from news, reviews, and social media. The design scheme of a hybrid model structure explored for novel data sets is rare.

2.2. Related Applications of Text Classification. The prospect of affordable access to substantial amounts of text data has encouraged opportunities for various analytic business, academic, and contextual exploits [5]. Text-classification applications have gained considerable attention from scholars in the field of NLP [27, 32, 33].

Bencke et al. [34] collected messages on citizens' complaints on official social networks regarding transportation, entertainment, and other services. They classified the messages into 14 corresponding dimensions of smart cities. The study compared different feature extraction methods to help classical classification models alleviate the dimensionality problem and pointed out the problem that the classification effect is affected by unbalanced data distribution. [35] proposed an intelligent system to monitor public opinion (i.e., favorable, neutral, and unfavorable) on vaccination decisions, which adopted a bag of words for text representation and achieved the best accuracy with a small sample

of training data (693 pieces of data). [36] analyzed law-related news (i.e., relevant, and irrelevant) and proposed a learning method that combines titles and body text, using a bidirectional gated recurrent unit (Bi-GRU) to encode title and body text, and then constructed a bidirectional attention stream to integrate information from both. A new approach for automatically analyzing political discourses of citizens and civil servants was proposed in [22], where they used multiscale CNNs in seven different languages to construct a discourse classifier to classify political manifestos into seven policy domains as well as political party background information to enhance the predictive power of the network.

Table 2 summarizes the text classification intelligent systems that support decision-making for governments. From the perspective of data sources, existing research collected data from specialized social networks [22, 34] and general social networks [35, 36], where general social network information requires additional operations to filter relevant texts. For the sample, unevenly distributed data adds difficulties to the multiclassification task. Methodologically, feature selection and deep learning are used to alleviate the problem of the high sparsity and high dimensionality of textual data. Finally, the text used in the model had a single body part, and the title information was ignored. In relatively few studies that consider titles, uniform structures are used to extract the characteristics of different components, lacking the analysis of textual characteristics. To address these issues, we propose a hybrid model based on deep learning to classify information-rich text. Developing e-government and establishing specialized channels have made accessing substantial amounts of petition data easy. Word2vec was utilized to convert words into low-dimensional vectors to solve the sparse word representation problem. We also analyzed the characteristics of each component of the e-petition text and designed various neural network structures to improve the classification ability of the model.

3. Materials and Methods

The proposed method combines CNN and Bi-LSTM to classify petition text. Figure 1 shows an overview of the proposed method.

3.1. Data Collection. The progress of the petitions and replies were selected and posted on the Shanghai e-petition BBS. Citizens register with their real names, log in, fill out the petition, and submit it. The petitions submitted are received

TABLE 2: Text classification intelligent systems supporting decision-making for governments.

Function	Data set	Class	Method	Text
Classification of smart city service [35]	Colab	14	Logistic regression	Body
Social media monitor [36]	Tweets related to vaccination	3	SVM + n-gram	Body
Public opinion analysis [22]	Law-related news	2	Bi-GRU	Title + body
Political analysis [37]	Political manifestos	7	CNN + Word2vec	Body

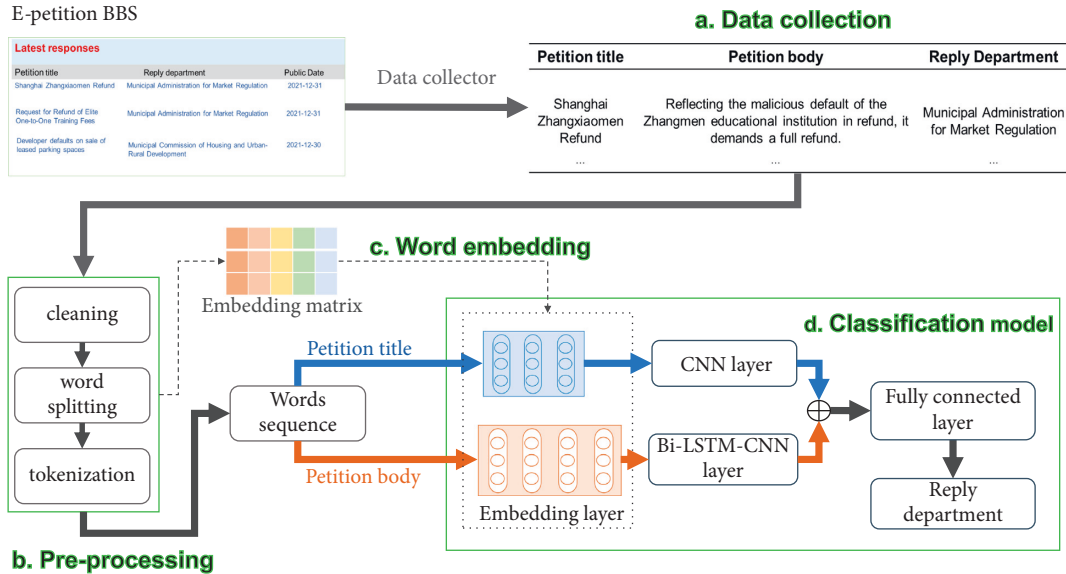


FIGURE 1: The proposed automated petition classification method overview. (a) Data collection; (b) pre-processing; (c) word embedding; (d) classification model.

and registered regularly by office workers and then forwarded to the relevant functional departments for proper handling according to their duties.

This study used the octopus data collector to automatically crawl petition text data in the BBS. An octopus is an automatic data collection application that simulates human behavior and supports user-designed collection processes. Figure 2 illustrates the collection process for this research. First, the petition bulletin board web page is opened within the collector and contains links to multiple publicized petitions. Clicking on the links leads to a petition details page, and clicking on the corresponding positions on the details page can conveniently capture the text in the corresponding fields on the page. An octopus can generate and loop all links, open the linked pages in turn, and automatically collect the text of the specified fields until all the corresponding texts of the links are collected. The collected data were saved locally in CSV file format. After data collection, each petition text was automatically labeled according to the reply to department. The automatic transmission problem of petition text was transformed into an ATC problem.

3.2. Data Preprocessing. Data preprocessing is the process of transforming raw text into the format required by ML algorithms. We preprocessed the raw data using three operations: cleaning, word splitting, and tokenization. Data preprocessing was implemented using python3 (see

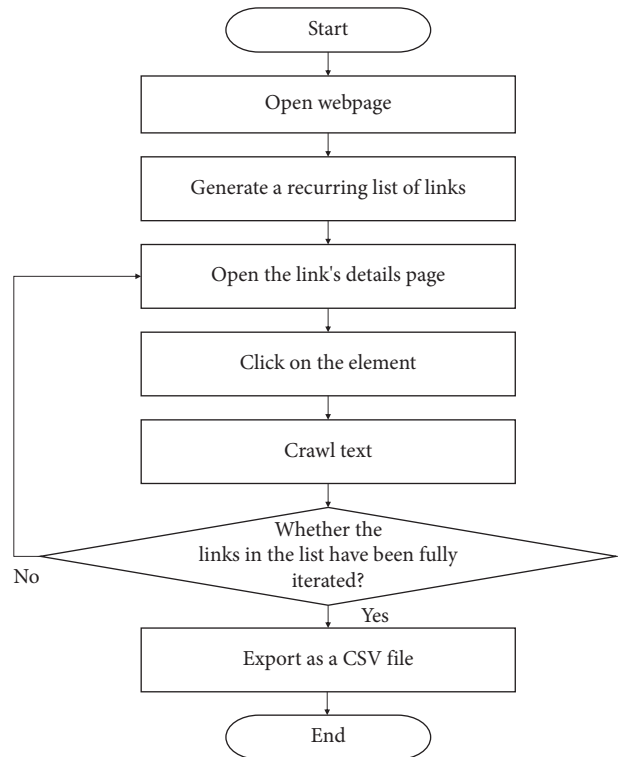


FIGURE 2: E-petition data collection process with octopus collector: design of the Data Collection Process.

```

Input: texts, user_dictionary_list, stopwords_list
Output: word_sequences
(1) //Step 1: content cleaning
(2)  $m = \text{size of (texts)}$  //get number of total documents in texts
(3) For  $i = 1$  to  $m$  do
(4)   Content = texts[ $i$ ] //get the content of  $i_{\text{th}}$  document
(5)   Content = content.strip() //remove the blanks
(6)    $n = \text{length (content)}$  //get number of total characters in content
(7)     For  $j = 1$  to  $n$  do
(8)       Character = content[ $j$ ]
(9)       If character <  $u^{\backslash}u4e00^{\prime}$  and character >  $u^{\backslash}u9fa5^{\prime}$  then
(10)        Character = character.strip() //remove the blanks
(11)      End if
(12)    End for
(13)  End for
(14) //Step 2: word splitting
(15) Jieba.load () //jieba is a python Chinese word segmentation module
(16) User_dictionary_list.load ()
(17) Stopwords_list.load ()
(18) Corpus = [] //build internal corpus
(19) For  $i = 1$  to  $m$  do
(20)   Word_list = jieba.lcut (texts[ $i$ ]) //split texts[ $i$ ]
(21)    $s = \text{length (word\_list)}$  //get number of total words in word_list
(22)   For  $j = 1$  to  $s$  do
(23)     If word_list[ $j$ ] in stopwords_list then
(24)       Remove (word_list[ $j$ ])
(25)     End if
(26)   End for
(27)   Corpus.append (word_list)
(28) End for
(29) //Step 3: tokenization
(30) Tensorflow.load () //tensorflow is a machine learning framework
(31) Tokenizer = tensorflow.keras.pre-processing.text.Tokenizer() //Tokenizer is a class that converts text into sequences
(32) Tokenizer.fit_on_texts (corpus)
(33) Sequences = tokenizer.texts_to_sequences (corpus)
(34) Word_sequences = tensorflow.keras.pre-processing.sequence.pad_sequences (sequences, maxlen =  $l$ )

```

ALGORITHM 1: Data Preprocessing

Algorithm 1 for the pseudocode). Figure 3 shows an example of the preprocessing of a petition text.

- (a) The cleaning process includes removing duplicate samples and null values, non-Chinese characters, and extra spaces. We first cleaned up these noises to prevent interference with the results. As shown in Figure 3(a), the horizontal tabs on both sides were removed.
- (b) The word-splitting process involves splitting text into individual words. The Chinese texts require specialized operations for word splitting because of the absence of space. Jieba [37] is an open-source library for NLP that targets Chinese texts for word splitting. The library supports adding a custom user dictionary and removing stop-words. This study added 1495 words for the names of local streets and roads to the user dictionary. We also summarized three stop-word lists (the Chinese stop-word list, the stop-words list of Harbin Institute of Technology, and the stop-words list of the machine intelligence laboratory) with a total of 2490 stop-

words. These words and symbols do not help the model to analyze and predict the category of the text but add computational complexity and system overhead. Figure 3(b) shows that after word splitting, such a sentence constitutes a row in the internal corpus.

- (c) Tokenization represents a sentence as a sequence of words. First, all words in the corpus are obtained to form vocabulary V , and each word is assigned a unique integer number. Thus, a sentence is transformed into a sequence of word tokens. The tokenizer class in Keras facilitates this. Because the neural network can only receive inputs of the same length, we processed sentences of varying lengths into a sequence of standard lengths based on the length distribution of the petition text. Sequences less than the standard length were padded with zeros at the end of the sequences, and sequences longer than the standard length had extra words at the back-end cut-off.

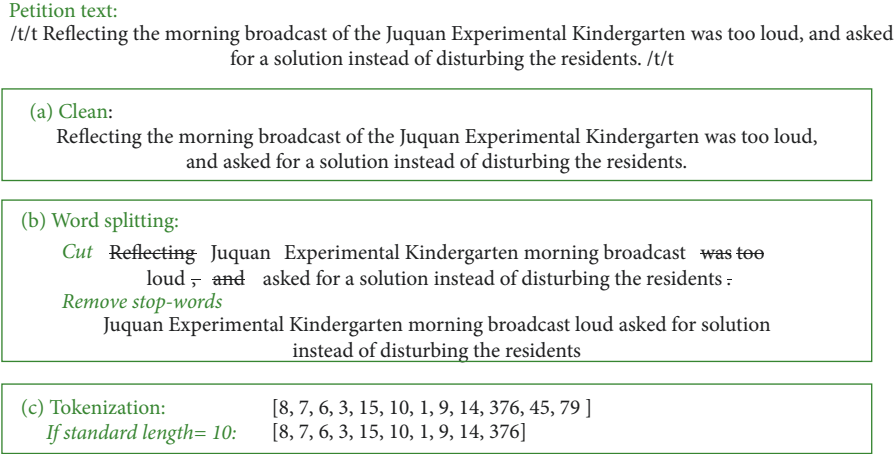


FIGURE 3: Example of preprocessing operation.

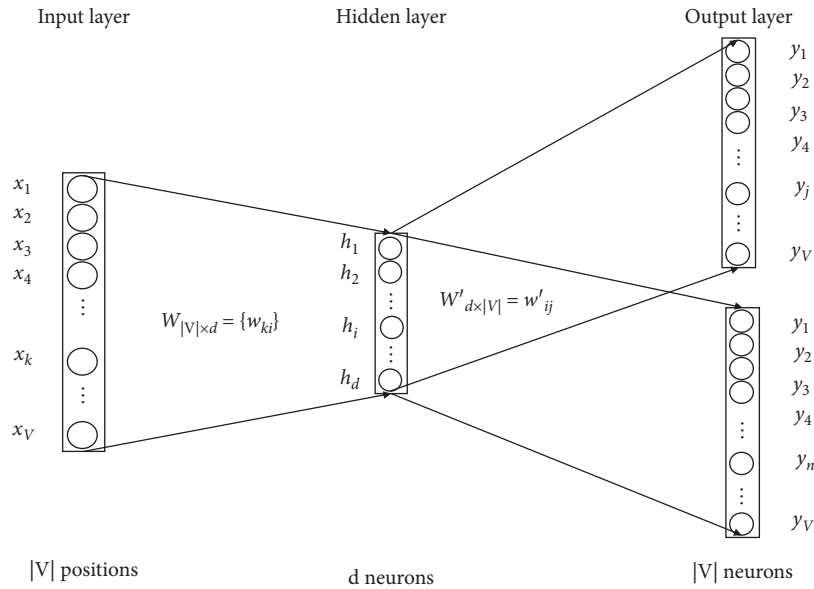


FIGURE 4: Word2vec embedding model training based on the skip-gram algorithm.

3.3. *Word Embedding.* To analyze text using machine learning algorithms, unstructured text must be converted into numerical form as input. Word embedding is a method of transforming words into vectors. In contrast to one-hot coding, word embedding allows text to be expressed low dimensionally. Word2vec is a mainstream statistical method for obtaining word vectors [38]. We employed word2vec based on the skip-gram algorithm to pretrain the embedding matrix. The skip-gram algorithm predicts the context words of the currently known word w_t in an internal corpus. The optimized objective function is as follows:

$$\mathcal{L} = \max \sum_{w \in c} \log p(\text{Context}(w) | w), \quad (1)$$

where $\text{Context}(w)$ is the context of the input word w . We defined a skip window parameter to represent the number of words selected from one side (left or right) of the current

input word. Then, several contextual words from the whole window were selected as our output words; thus, there were multiple sets (input words and output words) of the training data. This neural network was trained using all training data. The model structure of the skip-gram is shown in Figure 4, which has three layers: the input, hidden, and output layers. The input layer was a one-hot vector of length $|V|$. Hidden layer was calculated as follows:

$$h = W^T \cdot X = V_{w_t}^T. \quad (2)$$

The weight $W \in R^{|V| \times d}$ from the input layer to the hidden layer is the embedding matrix, in which d represents the dimension of the word-embedding vector and $|V|$ is a constant-size vocabulary. $V_{w_t}^T$ is a distributed vector that represents the word w_t .

The output layer represents the probability that each word in dictionary V is an output word.

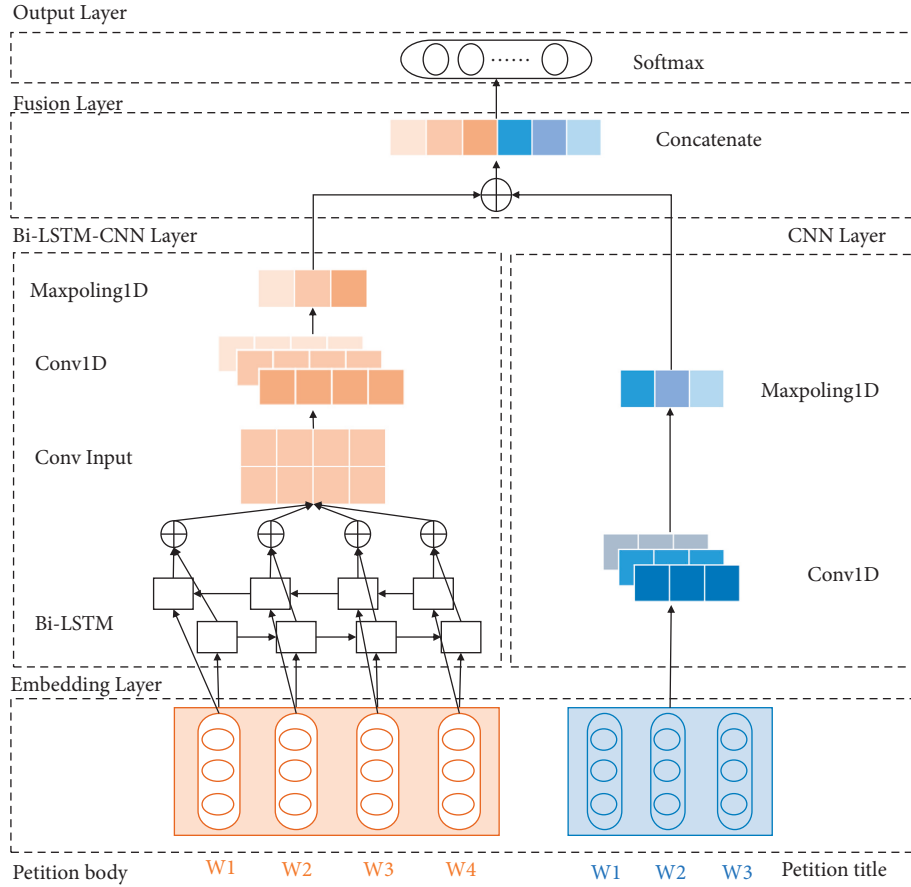


FIGURE 5: Architecture of the proposed hybrid deep learning classification method.

$$u_j = \sum_{i=1}^d W_{ij}'^T h_i, \quad (3)$$

$$P(w_j | w_i) = y_j = \frac{\exp(u_j)}{\sum_{k \in V} \exp(u_k)}.$$

3.4. Classification

3.4.1. Embedding Layer. This study used word2vec to pre-train an embedding matrix to initialize the weights of the embedding layers and fine-tune them. Each input sequence is mapped as a vector group through the embedding layer. Given a sequence consisting of l words: $\text{doc} = w_1, w_2, \dots, w_l$, where each word w_i is associated with tokenized real-valued encoding, we looked up the embedding matrix W and transform w_i to e_i by matrix vector product:

$$e_i = W^T v_i. \quad (4)$$

In equation (4), v_i has an equal length to $|V|$ and the elements have values between 0 and 1. The sequence of words is represented as

$$\text{doc} = [e_1, e_2, \dots, e_i, \dots, e_l]^T. \quad (5)$$

Figure 5 shows that the petition title and petition body are represented as vector groups of different standard lengths, which are subsequently input into the CNN and Bi-LSTM-CNN layers, respectively.

3.4.2. CNN Layer. CNN was widely used in the early days of image processing, but it has only recently been used for text classification tasks and outperformed sequence-based methods. The convolution windows applied to text in the NLP domain are usually one dimensional. For the 1DCNN, the convolution layer uses a 1D cross-correlation operation, which slides the convolution window from top to bottom on the input text. The length of the 1D convolution window was consistent with the dimensions of the word vector and the width was n . The convolution operation applies the filter $F \in R^{d \times n}$ dots with n words in the text to obtain a new feature c_i :

$$c_i = f(F \cdot x_{i:n} + b). \quad (6)$$

Here, f is a nonlinear activation function such as relu or tanh, $x_{i:n}$ is the concatenation of n words: $x_{i:n} = x_i \oplus x_{i+1} \oplus x_{i+2} \oplus \dots \oplus x_{i+n-1}$, and b is the bias term.

The convolution stride defines the distance between the positions of the convolution windows when they sweep through the adjacent feature map. In this study, the convolution step was set to 1, which means that the convolution

windows swept through the elements of the feature map one by one. We performed the same padding to maintain the output and input of the same size for feature extraction at the word level. Therefore, filter A generated one feature map $c = [c_1, c_2, \dots, c_l]$. Finally, we performed a 1D maximum pooling operation on the feature map generated by the filter f_i to capture the most important features.

$$p_i = \max(c_1, c_2, \dots, c_l). \quad (7)$$

Figure 6 shows an example of a filter that performs a one-dimensional convolution operation. The filter was multiplied by the word embeddings in the convolution window and summed to obtain a feature map containing locally dependent information. The maximum pooling operation selects the maximum value in the feature map to represent the local features captured by the filter. Filters are considerably important for CNN to automatically learn the features required to understand the text. Therefore, the size and number of filters are important parameters affecting the performance of CNN.

3.4.3. Bi-LSTM-CNN Layer. The unidirectional LSTM network accesses only forward information; however, reverse information is also needed in most cases to fully understand the context. Bi-LSTM effectively uses past and future contextual information to learn semantic information. LSTM is a variant of RNN that introduces a gating mechanism to control the accumulation speed of information, including the input gate i_t , forget the door f_t , and output gate o_t . The LSTM network introduces a new internal state c_t to simultaneously transmit recurrent information and output information to the external state of the hidden state h_t at the same time. The formula used is as follows:

$$\begin{aligned} i_t &= \sigma(W_i x_t + U_i h_{t-1} + b_i), \\ f_t &= \sigma(W_f x_t + U_f h_{t-1} + b_f), \\ o_t &= \sigma(W_o x_t + U_o h_{t-1} + b_o), \\ \tilde{c}_t &= \tanh(W_c x_t + U_c h_{t-1} + b_c), \\ c_t &= f_t \odot c_{t-1} + i_t \odot \tilde{c}_t. \end{aligned} \quad (8)$$

Here, σ is the sigmoid function. x_t is the input of the current time t , h_{t-1} is the hidden state of the last moment, \odot is the product of vector elements, c_{t-1} is the memory unit of the last moment, and \tilde{c}_t is a candidate state obtained by a nonlinear function. It selectively adds new information and forgets previously accumulated information, which can effectively solve the problems of gradient disappearance and gradient explosion of a simple recurrent neural network.

Assuming that the first layer is in the order of sentences and the second layer is in the reverse order of sentences, the hidden state at time t is defined as $h_t^{(1)}$ and $h_t^{(2)}$, then

$$\begin{aligned} h_t^{(1)} &= f(U^{(1)} h_{t-1}^{(1)} + W^{(1)} x_t + b^{(1)}), \\ h_t^{(2)} &= f(U^{(2)} h_{t-1}^{(2)} + W^{(2)} x_t + b^{(2)}), \\ h_t &= h_t^{(1)} \oplus h_t^{(2)}, \end{aligned} \quad (9)$$

where \oplus is a vector concatenate operation.

When using LSTM for text classification tasks, the hidden-layer state of the last time step is typically used as the penultimate layer. However, this study extracted local features using a 1DCNN based on the contextual features of long texts. Therefore, the hidden state of each time step was returned, and h_t was the concatenation of the hidden states of the forward and backward units at time step t . A text sequence of length l returns l hidden states after context features are extracted by Bi-LSTM, and these returned hidden states can be regarded as a sequence of words of length l with embedding dimension $2h$. Next, we performed the convolution and maximum pooling operations described in Subsection 3.4.2. The 1DCNN was performed on returned hidden states and then a maximum pooling operation to capture the prominent features of the petitioning body.

3.4.4. Fusion Layer. This study used different neural network structures to extract features according to the length characteristics of various petition parts. The Bi-LSTM-CNN layer uses the petition body as input, extracts contextual information from the input using forward and backward LSTMs, and returns the hidden state of all time steps into a 1DCNN for convolution and maximum pooling. Meanwhile, the CNN layer uses the petition title as input, performs a convolution operation on the input, and calculates the maximum value of each activation mapping using 1D maximum pooling. To obtain the advantages of both shallow neural networks, the output of the Bi-LSTM-CNN layer, noted O_b , and the output of the CNN layer, noted O_t , are concatenated to create a unified representation Y . Finally, the resulting unified representation is transported to the output layer.

$$Y = O_b \oplus O_t. \quad (10)$$

3.4.5. Output Layer. The proposed end-to-end framework for automatic classification supports multiple petition classifications. The fully connected layer integrates the category differentiation information in Y and then outputs y_i . The calculation formula is as follows:

$$y_i = W_{(y_i)}^T Y, \quad (11)$$

where $W_{(y_i)}^T$ is the learnable weight connected to the neuron y_i . The softmax activation function was used to generate a probability p_i for each label. Finally, the label with the highest probability among the k labels was selected as the final reply department of petition P .

$$p_i = \frac{\exp(y_i)}{\sum_{j \in k} \exp(y_j)}, \quad (12)$$

$$y = \max(p_1, p_2, \dots, p_k).$$

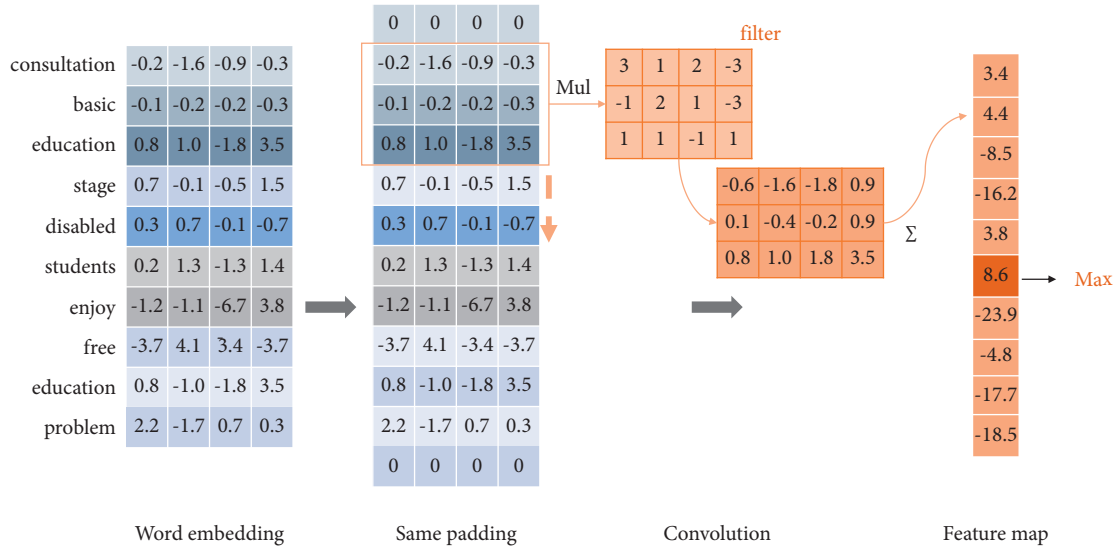


FIGURE 6: An example of using a filter to extract features.

4. Numerical Experiments

4.1. E-Petition Data Set. In 2016, Shanghai integrated various channels to establish a comprehensive e-petitioning platform. This study conducted an experiment using open petition data collected from May 2016 to September 2021. We chose departments that received over 1000 e-petitions as labels for the classifier, and 11 departments were selected. After removing duplicate and missing values, 28085 records were collected as the data set for this study, and Table 3 shows the categories and data volume statistics.

4.2. Data Preparation. The number of words in the corpus of the fully structured e-petition data was 110,645. Figure 7 shows the text length distributions of the title and body. The title is truncated at 10, and the text is truncated at 500, but with a relatively long right tail. Excessive length increases the computational overhead; therefore, we used 10 and 500 as the standard length of the title sequence and body sequence, respectively.

For the preprocessed petition data set, 20% of the shuffling data set was selected as the test set and 80% as the training set. The validation set comprised the last 10% of the training set. The proportions of the categories in the three data sets remained similar. Table 4 summarizes the statistics and splitting of the data sets.

4.3. Classification and Comparison

4.3.1. Parameter Setting. Some basic parameter settings are summarized in Table 5, which serve as the default settings for the proposed classification model and work well in many cases. Owing to the limited amount of sample data, which contains noisy data, it is easy to obtain high training accuracy on an unknown data set. Early stopping is used to prevent overfitting. During the gradient descent training process, the parameters that converged on the

training set were not necessarily the best on the test set. This study used validation loss as the monitor. In each epoch, we estimated the newly obtained model for the validation set and computed the validation loss. If the validation loss did not decrease, then the iteration was stopped. To solve the problem of class imbalance, class weight was considered to weigh the loss function during training to make the model more attentive to the samples of underrepresented classes. In this study, the class weight was set to “balanced” and the weight of category i was calculated as follows:

$$w_i = \frac{N}{\text{labels} * n_i}, \quad (13)$$

where N is the total number of samples, labels are the total number of categories, and n_i is the number of samples in category i .

In addition to the aforementioned basic settings, some important parameters were sought to improve the performance of the model (see Table 6). The introduction of a dropout before the output layer can alleviate this overfitting problem. The problem of gradient explosion appears in model training when the activation function in LSTM is set as relu; therefore, tanh was set as the default. The activation function of the CNN layer was optimized for relu and tanh, as recommended by [15]. To select the optimal parameter value to achieve high accuracy, we trained the model on the training set and determined the optimal parameter settings based on the classification performance of the validation set.

4.3.2. Evaluation Measures. The evaluation measures include accuracy, precision, recall, and $F1$ score; category i to be observed was considered positive, and the rest of the categories were considered negative, and a confusion matrix similar to binary classification was obtained. The evaluation metrics were calculated as follows:

TABLE 3: Classes and volume of the petition data set.

Reply departments	Volume	Label	Proportion (%)
Municipal Finance Bureau	1174	0	4.18
Public Security Bureau	3033	1	10.80
Municipal Education Commission	4765	2	16.97
Municipal Human Resources and Social Security Bureau	1707	3	6.08
Municipal Administration for Market Regulation	5597	4	19.93
Municipal Health Commission	1437	5	5.12
Municipal Commission of Housing and Urban-Rural Development	3992	6	14.21
Municipal Transportation Commission	2446	7	8.71
Landscaping & City Appearance Administrative Bureau	822	8	2.93
Urban Management and Law Enforcement Bureau	1252	9	4.46
Planning and Natural Resources Bureau	1860	10	6.62

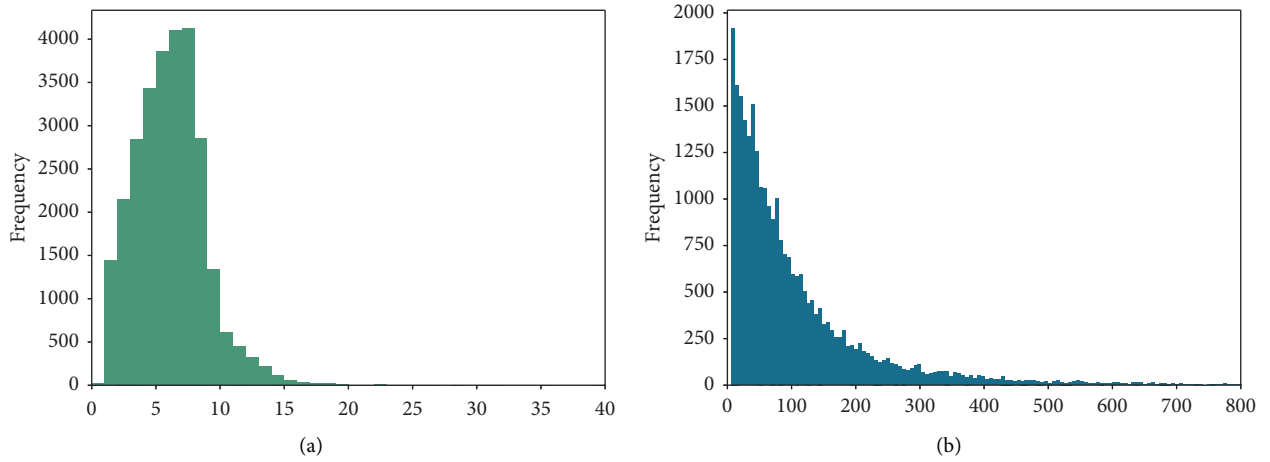


FIGURE 7: Length distribution of word sequences. (a) Length of title; (b) length of body.

TABLE 4: Statistics and splitting of e-petition data set.

Data set	Training set	Validation set	Test set	Vocab	Title length	Body length
28085	20221	2247	5617	110645	10	500

TABLE 5: Basic parameter settings of the classification model.

Parameter	Value
Loss function	Categorical cross-entropy
Metrics	Categorical accuracy
Optimizer	Adam
Early stopping	monitor = 'val-loss', patience = 1
Class weight	Balanced

TABLE 6: Key parameters of the classification model to be optimized.

Parameter	Explanation	Scope
Batch size (b)	Number of samples per gradient update	$16 \leq b \leq 64, b \in \mathbb{Z}$
Learning rate (lr)	Hyperparameters in updating weights during gradient descent	$0.0001 \leq lr \leq 0.01$
Embedding size (e)	The dimensionality of the word vector	$100 \leq e \leq 600, e \in \mathbb{Z}$
Hidden size (h)	Number of neurons in the hidden layer	$32 \leq h \leq 256, h \in \mathbb{Z}$
Kernel size (c_1)	Length of convolution window in Bi-LSTM-CNN layer	$2 \leq c_1 \leq 10, c_1 \in \mathbb{Z}$
Kernel size (c_2)	Length of convolution window in CNN layer	$1 \leq c_2 \leq 6, c_2 \in \mathbb{Z}$
Filter size (f_1)	Number filters in Bi-LSTM-CNN layer	$10 \leq f_1 \leq 400, f_1 \in \mathbb{Z}$
Filter size (f_2)	Number filters in CNN layer	$5 \leq f_2 \leq 200, f_2 \in \mathbb{Z}$
Dropout (d)	A simple way to prevent neural networks from overfitting	$0 \leq d \leq 0.8$
Activation function (a)	A function for introducing nonlinear factors into a neural network	Relu or tanh

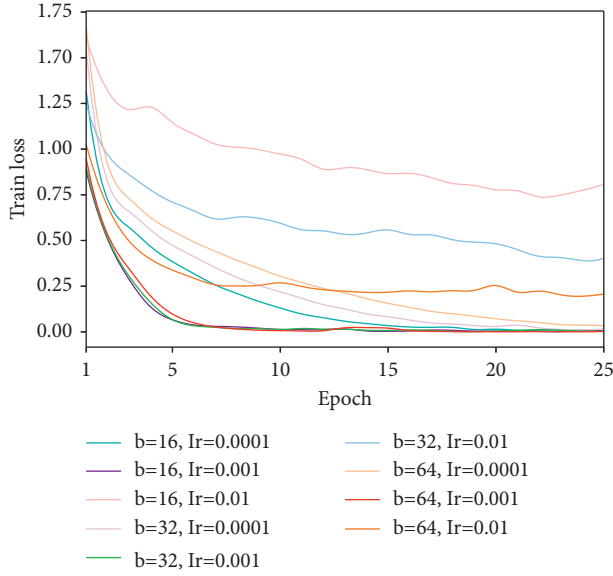


FIGURE 8: Training loss reduction curves for different combinations of batch size and learning rate.

$$\begin{aligned}
 \text{Accuracy} &= \frac{TP + TN}{N}, \\
 P_i &= \frac{TP}{TP + FP}, \\
 R_i &= \frac{TP}{TP + FN}, \\
 F1_i &= \frac{2P_i \times R_i}{P_i + R_i}.
 \end{aligned} \tag{14}$$

Considering the uneven distribution of the samples, we introduced weights to each evaluation index to evaluate the overall classification effect of the samples. Here, the weights were determined by the sample proportion, p .

$$\begin{aligned}
 \text{Weighted - } P &= \sum_{i=0}^{10} p_i P_i, \\
 \text{Weighted - } R &= \sum_{i=0}^{10} p_i R_i, \\
 \text{Weighted - } F1 &= \sum_{i=0}^{10} p_i F1_i.
 \end{aligned} \tag{15}$$

4.3.3. Parameter Optimization. To determine the optimal settings of many hyperparameters in the model step-by-step, we randomly initialized a set of parameters and selected the optimal choice in the current state as the setting of the parameters. Figure 8 shows the decline of the model in the training loss over 25 epochs with nine sets of batch sizes and learning rates. The results show that the model reached the lowest loss fastest at a learning rate of 0.001, with three batch size settings. When the batch size was 64, the training time was shorter than that for the other two batch size settings. Considering the training time of the model, the final choice was a learning rate of 0.001 and a batch size of 64.

Next, the remaining parameters were optimized sequentially. Figure 9(a) shows the classification accuracy of the configuration of the embedding size on the validation set. The model had the highest validation accuracy when the embedding size was set to 400. Figure 9(b) shows that the classification results were slightly better when the hidden size was set to 128. For the kernel size, the convolution size of the body had a significant impact on the classification performance of the model, fluctuating by 5%. We selected $c1=5$ and $c2=3$ as the optimal parameter settings. Figures 10(a) and 10(b) show that when the number of filters was below 100, the accuracy was positively correlated with the number of filters, and the optimal number of filters was set to 100. Figure 10(c) shows that the model performed best when dropout=0.25. Figure 10(d) shows that the two activation functions have minimal impact on model performance, and the activation function set as tanh is slightly better.

4.3.4. Classification Result. We controlled the three embedded modes of the proposed structure in the embedding layer and obtained the classification results for the test set (see Table 7). Word2vec pretrained word embedding with fine-tuning in the embedding layer had the highest classification accuracy, weighted precision, weighted recall, and weighted-F1 score, and the randomly initialized word embedding approach had the poorest classification performance. In addition, pretrained word embeddings, either static or fine-tuned, can reduce the training time of the model.

4.3.5. Comparisons and Discussion. This study compared baseline models with the proposed model to verify its classification performance. The basic settings of the baseline models were consistent with those of the proposed model (see Table 5), and the other settings are listed in Table 8. The input of baseline models represented as “body + title”, which respectively indicates the petition body and petition title.

The classification results of the proposed and baseline models for the test set are summarized in Table 9. The baseline models provided reasonable results, and the proposed method was more effective. First, in the case of using the body as the input text for the model, hybrid models (M7, M10) outperformed the single structure models (M1 and M4) in each evaluation. The results showed that Bi-LSTM outperforms Text-CNN, which demonstrates that extracting contextual features is more effective for classification tasks for long petition bodies. In addition, the hybrid approach of Bi-LSTM for extracting contextual features, followed by CNN for extracting local features, showed better results. Second, introducing title information can improve the classification effect (M2, M3, M5, M6, M8, M9, M11, and proposed model). Compared to the Bi-LSTM-CNN, the proposed model improves 1.26%, 1.67%, and 1.58% in weighted precision, weighted recall, and weighted F1 score, respectively. Text-CNN, which performed the worst in text classification using the body of the petition, improved the recall by 3.22% after adding the title. Third, among the models with titles, the evaluations of models with the CNN

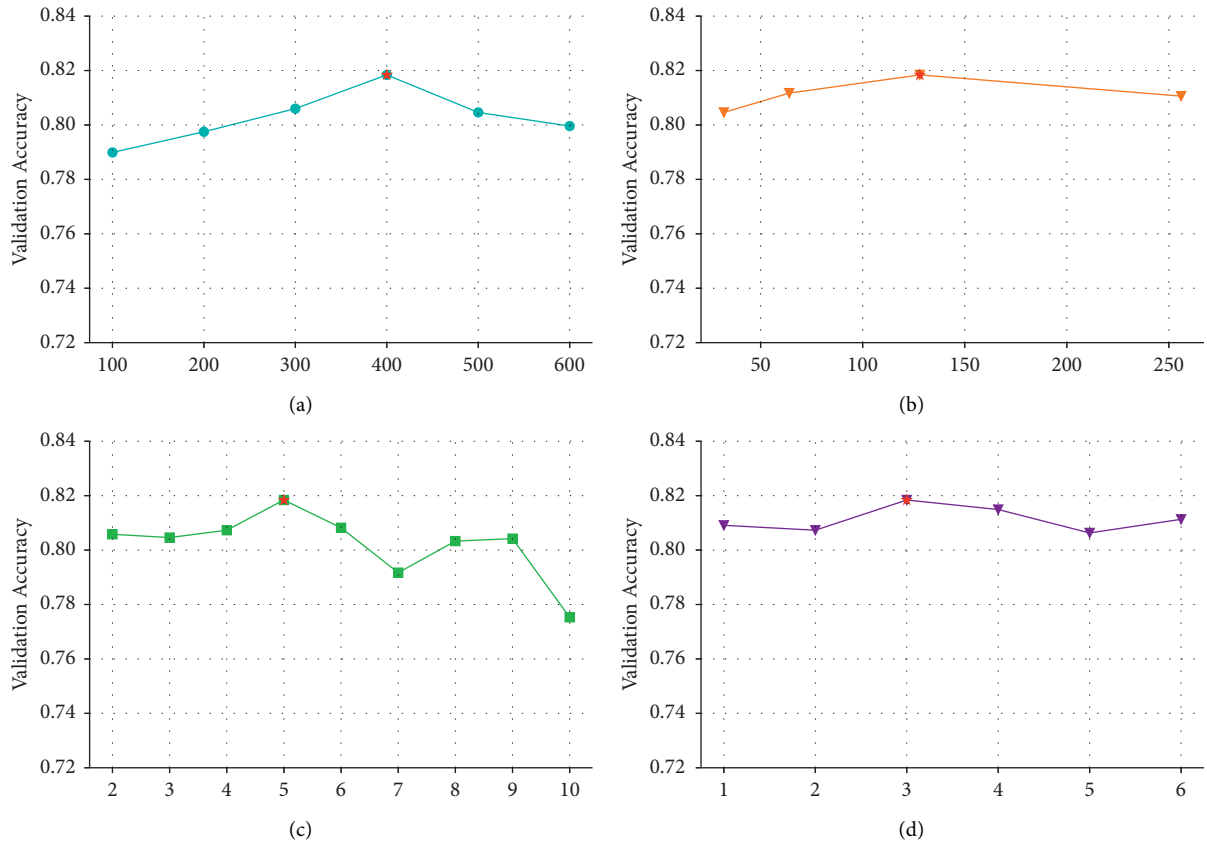


FIGURE 9: Parameter optimization of embedding size (e), hidden size (h), and convolutional kernel size ($c1$, $c2$). (a) Embedded size (e); (b) hidden size (h); (c) kernel size ($c1$); (d) kernel size $c2$.

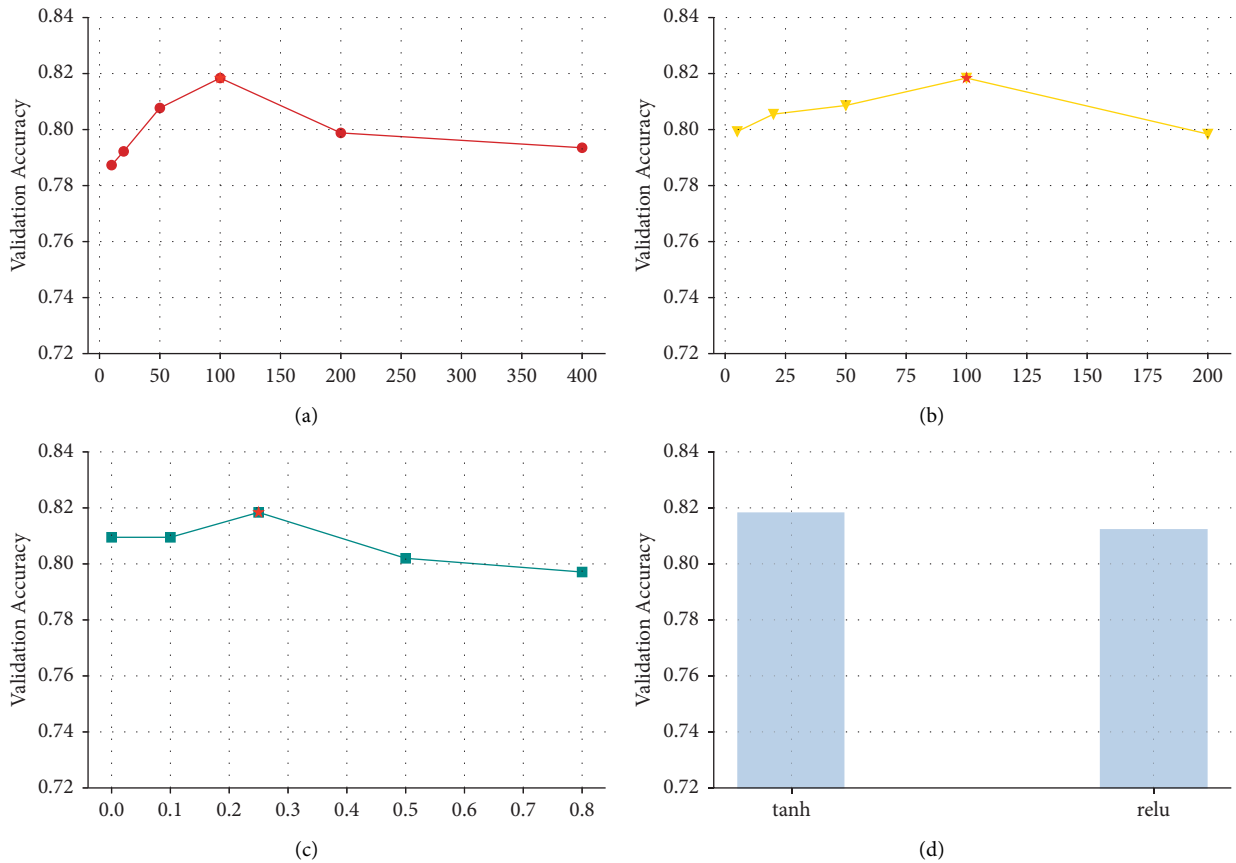


FIGURE 10: Parameter optimization of filters ($f1$, $f2$), dropout d , and activation function a . (a) Filters ($f1$); (b) filters ($f2$); (c) dropout (d); (d) activation function (a).

TABLE 7: Classification results of three embed modes of the embedding layer on the test set.

Embed mode	Weighted-P	Weighted-R	Weighted-F1	Training time (second)
Random	0.8137	0.8104	0.8103	1249
Static	0.8226	0.8214	0.8212	430
Fine-tuning	0.8288	0.8262	0.8267	1100

TABLE 8: Configurations of baseline models.

Baseline models	Parameter setting
Text-CNN (M1)	$e = 400, c_1 = 3, 4, 5$, filters = 100, input = petition body
Text-CNN + LSTM (M2)	$e = 400, c_1 = 3, 4, 5, h = 128$, input = petition body and title
Text-CNN + CNN (M3)	$e = 400, c_1 = 3, 4, 5, c_2 = 3$, filters = 100, input = petition body and title
Bi-LSTM (M4)	$e = 400, h = 128$, input = petition body
Bi-LSTM + LSTM (M5)	$e = 400, h_1 = 128, h_2 = 128$, input = petition body and title
Bi-LSTM + CNN (M6)	$e = 400, h = 128, c_2 = 3$, input = petition body and title
CNN - Bi-LSTM (M7)	$e = 400, c_1 = 5, h = 128, c_2 = 3$, input = petition body
CNN - Bi-LSTM + LSTM (M8)	$e = 400, c_1 = 5, h_1 = 128, h_2 = 128$, input = petition body and title
CNN - Bi-LSTM + CNN (M9)	$e = 400, c_1 = 5, h = 128, c_2 = 3$, input = petition body and title
Bi-LSTM-CNN (M10)	$e = 400, c_1 = 5, h = 128$, input = petition body
Bi-LSTM-CNN + LSTM (M11)	$e = 400, c_1 = 5, h_1 = 128, h_2 = 128$, input = petition body and title

TABLE 9: Evaluation of the proposed model and baseline models in the test set.

Models	Weighted-P	Weighted-R	Weighted-F1
M1	0.7856	0.7668	0.7685
M2	0.8006	0.7899	0.7920
M3	0.8026	0.7990	0.7988
M4	0.7892	0.7839	0.7836
M5	0.8044	0.7953	0.7971
M6	0.8124	0.8109	0.8104
M7	0.7883	0.7821	0.7825
M8	0.7986	0.7942	0.7952
M9	0.7941	0.7887	0.7894
M10	0.8162	0.8095	0.8109
M11	0.8169	0.8124	0.8131
Proposed model	0.8288	0.8262	0.8267

structure (M3, M6, proposed model) are better than those of models with the LSTM structure (M2, M5, M11). Compared with the baseline models, the proposed model achieved the best classification results in the petition text classification task.

We summarized the *F1* score for each class (see Figure 11) to investigate the classification performance of each model in the unbalanced data set. *F1* score balances the precision and recall of the classification model. The results show that the proposed model had a high *F1* score of over 0.74 in each class. For Classes 2, 3, and 5, where the classification results were generally good, the *F1* scores of the proposed model were close to 0.9. The *F1* scores of the proposed model significantly improved for classes 0, 7, 8, and 10. Our model provides more comprehensive classification results for biased samples.

Considering the independence of each government department, evaluating the classification effects of all departments is beneficial for discovering the causes of differences in classification effects among departments. We calculated the confusion matrix for the classification results. Each matrix element was divided by the sum of each column, i.e., the misclassification rate of each category (see Figure 12). Although the proposed model significantly improves the misclassification rate of class 6 compared to the other baseline models, all models tend to misclassify classes 6, 7, and 10. Analyzing the classification results of the proposed model, there were 41 petitions for “tenement” and “facility management” in class 7 that were mistakenly classified as class 6 (8.12%) and 57 petitions for housing relocation in class 10 that were mistakenly classified as class 6 (15.45%). We investigated the duties of the department of Class 6, which included coordinating various departments to manage land use and supervising construction and housing issues. One of the duties of the department of Class 10 is planning the construction of engineering projects, and the department of Class 7’s duties are related to parking lot

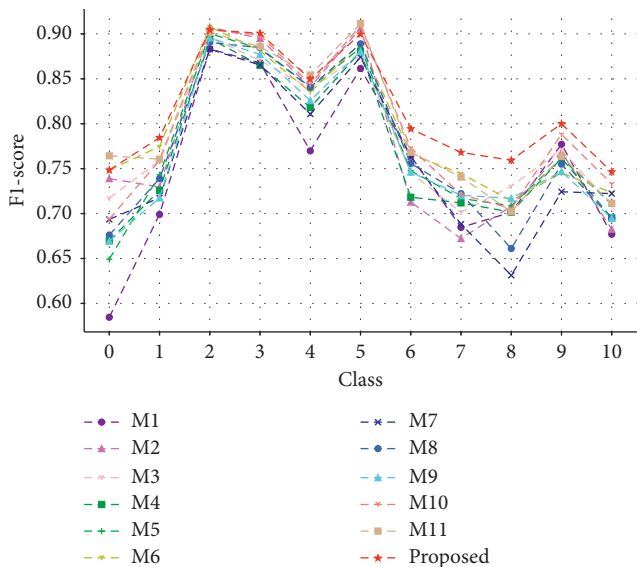


FIGURE 11: *F1* score of proposed model and baseline models in each class on the test set.

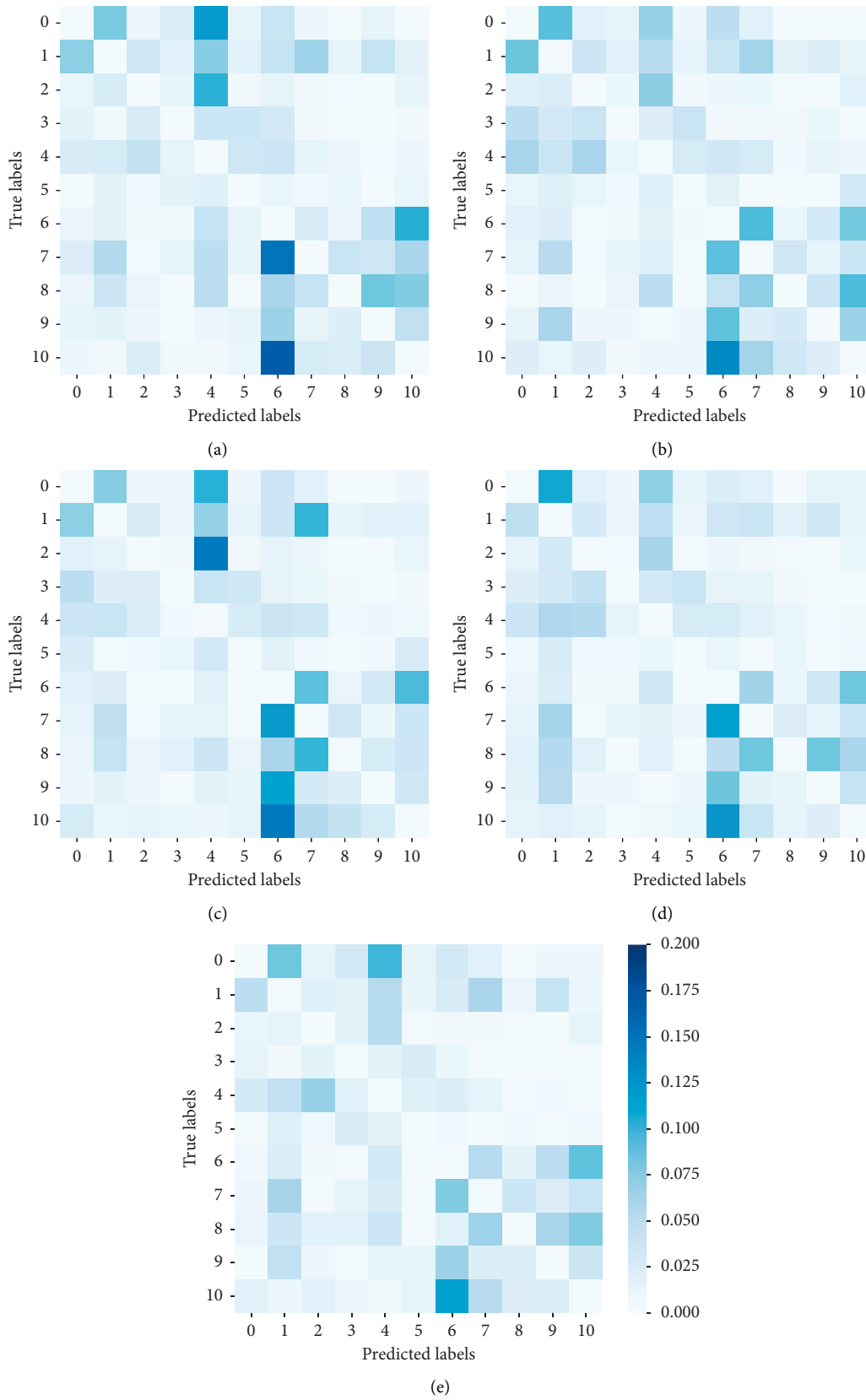


FIGURE 12: Misclassification of the proposed and baseline models on the test set: (a) Text-CNN; (b) Bi-LSTM; (c) CNN-Bi-LSTM; (d) Bi-LSTM-CNN; (e) Proposed model.

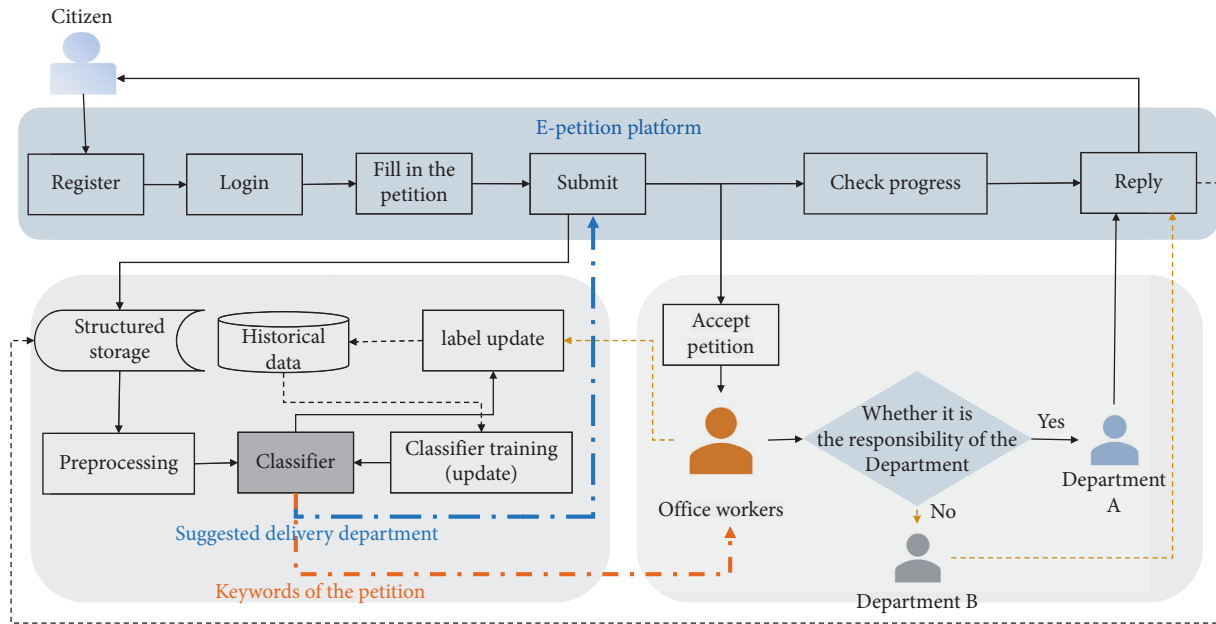


FIGURE 13: Petition automated forwarding decision support system.

operations in urban areas. Their duties overlap when dealing with housing issues. Clear and well-defined responsibilities are important for the effective automatic classification of petitions.

4.4. Implications and Applications. Efficient interaction between citizens and the government can help the government analyze public opinion, understand and solve difficulties in people’s lives, and make favorable decisions. Assessing the “e-petition platform” in China, citizens are required to choose a responsible department when submitting a petition, and office workers receive the petition, sort it, and send it to the responsible department according to the demand. Because citizens do not have a clear understanding of the department’s responsibility, they sometimes choose the wrong responsible department. When petition office workers sort many petitions, some petitions have unknown needs and cannot be quickly processed.

Using the automatic text classification model proposed in this study and the current application requirements, we designed a text-based petition decision support system to help citizens in selecting a responsible department and to help office staff improve the sorting speed of petitions with unclear demands. As shown in Figure 13, on the one hand, after citizens register and log in to the e-petition platform, they submit a petition with a title and body. The decision support system uses a classifier trained from historical data to predict the responsible department, provides the predicted result to the citizen for reference, and then stores label A. Moreover, the submitted petition is received and registered by the office staff, which provides reference keywords to help the staff improve the sorting speed and handle petitions with unclear needs. If the staff judges that the petition does not fall under the authority of Department A, the petition is forwarded to Department B, and the label is

updated. Meanwhile, the data are added to the training set to update the classifier. Before autonomous classification, we first store the data in a structured manner and store the labels and replies, which accumulate data resources for further analysis of public opinion, prediction of hot topics, and evaluation of department performance. This will become an integral part of the e-government decision support system. The system will also continuously update the data to improve the accuracy of autonomous classification, which remarkably improves the efficiency of petition administrators.

In addition to the application framework, we also provide some useful application suggestions based on the research results and findings. First, the data of each department is unbalanced. We should strengthen the ability to identify categories with small sample sizes, balance the proportion of samples in each category, and be alert to the extreme prediction of the classifier as a department with a large sample size. Second, we set a classification threshold for a single petition. Departments with more overlapping responsibilities had similar predicted probabilities. When the difference between the predicted probabilities of multiple classes is small, we set a threshold for delivery to multiple departments.

5. Conclusion

Communication and interaction between citizens and government are important for social governance. This study researched questions for petition autonomous delivery and decision support by reviewing the gap between existing research and application requirements. We proposed a hybrid model that integrates the advantages of both neural networks. The petitions were unstructured. Therefore, we preprocessed the text and mapped the words into low-dimensional vectors. Then, we input the word

embedding of the title and body into the hybrid deep learning model, extracting the contextual and local features to realize the autonomous classification of the petition-responsible department. Numerical experimental results show that compared with the baseline models, the overall *F1* score of the proposed method is 0.8267, which is 5.82% higher than that of Text-CNN, 4.31% higher than that of Bi-LSTM, and 1.58% higher than that of Bi-LSTM-CNN.

Further, we explored the superiority of the model in various classes and found that the hybrid model outperformed the simple model. The proposed model incorporates the title and body of the text well and had better classification performance. Finally, we designed a decision-making support system that can store data and update classifiers, thereby significantly promoting the automation and efficiency of the petition workflow. We also provided useful suggestions for applications in real-world scenarios. In conclusion, our research provides a significant practical reference.

Furthermore, we must note that departments receiving a few e-petitions are not included in this study and that overlapping responsibilities among departments may be biased in practice. Therefore, further analysis should focus on small samples and the problem of e-petitions corresponding to multiple departments.

Data Availability

Data can be obtained via the request of the corresponding author.

Conflicts of Interest

The authors declare that they have no conflicts of interest.

Acknowledgments

This work was supported in part by the National Natural Science Foundation of China (grant nos. 52131101, 51939001, and U1813203), the Liaoning Revitalization Talents Program (grant nos. XLYC1807046, and XLYC1908018), the Natural Science Foundation of Liaoning Province (grant no. 2020-HYLH-26), and the Science and Technology Fund for Distinguished Young Scholars of Dalian (grant no. 2021RJ08). Thanks to Jinsong Jia, Jinling Zhou, Yuchuan Hu, Weizheng Zhao, and Licheng Zhao for the experiment assistance and technique discussion. We acknowledge editors Afaq Ahmad and Toqeer Mahmood and reviewers for the valuable advice and publishing support.

References

- [1] J. Jiang, T. Meng, and Q. Zhang, "From Internet to social safety net: the policy consequences of online participation in China," *Governance*, vol. 32, no. 3, pp. 531–546, 2019.
- [2] C. Leston-Bandeira, "Parliamentary petitions and public engagement: an empirical analysis of the role of e-petitions," *Policy & Politics*, vol. 47, no. 3, pp. 415–436, 2019.
- [3] C. Puschmann, M. T. Bastos, and J. H. Schmidt, "Birds of a feather petition together? Characterizing e-petitioning through the lens of platform data," *Information, Communication & Society*, vol. 20, no. 2, pp. 203–220, 2016.
- [4] C. C. Aggarwal and C. X. Zhai, "A survey of text classification algorithms," in *Mining Text Data*, C. Aggarwal and C. Zhai, Eds., Springer, Boston, MA, 2012.
- [5] J. Hartmann, J. Huppertz, C. Schamp, and M. Heitmann, "Comparing automated text classification methods," *International Journal of Research in Marketing*, vol. 36, no. 1, pp. 20–38, 2019.
- [6] M. A. Ibrahim, M. U. Ghani Khan, F. Mehmood, M. N. Asim, and W. Mahmood, "GHS-NET a generic hybridized shallow neural network for multi-label biomedical text classification," *Journal of Biomedical Informatics*, vol. 116, Article ID 103699, 2021.
- [7] P. Barberá, A. E. Boydston, S. Linn, R. Nagler, and J. Nagler, "Automated text classification of news articles: a practical guide," *Political Analysis*, vol. 29, no. 1, pp. 19–42, 2021.
- [8] S. Clark, N. Lomax, and M. A. Morris, "Classification of Westminster Parliamentary constituencies using e-petition data," *EPJ Data Science*, vol. 6, no. 1, p. 16, 2017.
- [9] J. Bughin, E. Hazan, S. Ramaswamy et al., *Artificial Intelligence: The Next Digital Frontier?* McKinsey Global Institute, McKinsey & Company, Atlanta, 2017.
- [10] T. Joachims, "Text categorization with support vector machines: learning with many relevant features," in *Lecture Notes in Computer Science*, C. Nédellec and C. Rouveirol, Eds., vol. 1398, Berlin, Heidelberg, Springer, 1998.
- [11] V. D'Orazio, S. T. Landis, G. Schrodt, and P. Schrodt, "Separating the wheat from the chaff: applications of automated document classification using support vector machines," *Political Analysis*, vol. 22, no. 2, pp. 224–242, 2014.
- [12] S. Tan, "An effective refinement strategy for KNN text classifier," *Expert Systems with Applications*, vol. 30, no. 2, pp. 290–298, 2006.
- [13] Z. Yang, X. Nie, W. Xu, and J. Guo, "An approach to spam detection by naive Bayes ensemble based on decision induction," in *Proceedings of the 6th International Conference on Intelligent Systems Design and Applications*, pp. 861–866, Jian, China, October 2006.
- [14] G. E. Hinton, R. R. Salakhutdinov, and R. R. Salakhutdinov, "Reducing the dimensionality of data with neural networks," *Science*, vol. 313, no. 5786, pp. 504–507, 2006.
- [15] Y. Kim, "Convolutional neural networks for sentence classification," in *Proceedings of the 2014 Conference on Empirical Methods in Natural Language Processing*, pp. 1746–1751, Doha Qatar, Aug 2014.
- [16] J. Cheng, P. Li, Z. Ding, S. Zhang, and H. Wang, "Sentiment classification of Chinese microblogging texts with global RNN," in *Proceedings of the 2016 IEEE First International Conference on Data Science in Cyberspace*, pp. 653–657, Changsha, China, June 2016.
- [17] C. Masterson and M. Masterson, "Using word order in political text classification with long short-term memory models," *Political Analysis*, vol. 28, no. 3, pp. 395–411, 2020.
- [18] H. Ye, B. Cao, Z. Peng, T. Chen, Y. Liu, and J. Liu, "Web services classification based on wide & Bi-LSTM model," *IEEE Access*, vol. 7, pp. 43697–43706, 2019.
- [19] J. L. Cui, S. Qiu, M. Y. Jiang, Z. L. Pei, and Y. N. Lu, "Text classification based on ReLU activation function of SAE algorithm," *Advances in Neural Networks - ISNN 2017*, vol. 10261, pp. 44–50, 2017.

- [20] M. Y. Jiang, Y. C. Liang, X. Y. Feng et al., "Text classification based on deep belief network and softmax regression," *Neural Computing & Applications*, vol. 29, no. 1, pp. 61–70, 2018.
- [21] D. Larabi-Marie-Sainte and S. Larabi-Marie-Sainte, "Arabic text classification using convolutional neural network and genetic algorithms," *IEEE Access*, vol. 9, pp. 91670–91685, 2021.
- [22] A. Bilbao-Jayo and A. Almeida, "Automatic political discourse analysis with multi-scale convolutional neural networks and contextual data," *International Journal of Distributed Sensor Networks*, vol. 14, no. 11, Article ID 155014771881182, 2018.
- [23] W. Huang and H. Huang, "A gating context-aware text classification model with BERT and graph convolutional networks," *Journal of Intelligent and Fuzzy Systems*, vol. 40, no. 3, pp. 4331–4343, 2021.
- [24] B. Jang, M. Kim, G. Harerimana, S. u. Kang, and J. W. Kim, "Bi-LSTM model to increase accuracy in text classification: combining Word2vec CNN and attention mechanism," *Applied Sciences*, vol. 10, no. 17, p. 5841, 2020.
- [25] P. Zhou and N. El-Gohary, "Domain-specific hierarchical text classification for supporting automated environmental compliance checking," *Journal of Computing in Civil Engineering*, vol. 30, no. 4, 2016.
- [26] P. Blunsom, E. Grefenstette, and N. Kalchbrenner, "A convolutional neural network for modelling sentences," pp. 655–665, 2014, <https://arxiv.org/abs/1404.2188>.
- [27] M. M. Mostafa, "More than words: social networks' text mining for consumer brand sentiments," *Expert Systems with Applications*, vol. 40, no. 10, pp. 4241–4251, 2013.
- [28] S. Lu and Y. Lu, "A modularized architecture of multi-branch convolutional neural network for image captioning," *Electronics*, vol. 8, no. 12, p. 1417, 2019.
- [29] R. Collobert, J. Weston, L. Bottou, M. Karlen, K. Kavukcuoglu, and P. Kuksa, "Natural language processing (almost) fromscratch," *Journal of Machine Learning Research*, vol. 12, pp. 2493–2537, 2011.
- [30] A. C. Metlapalli, T. Muthusamy, and B. P. Battula, "Classification of social media text spam using VAE-CNN and LSTM model," *Ingénierie des Systèmes d'Information*, vol. 25, no. 6, pp. 747–753, 2020.
- [31] C. Li, G. Zhan, and Z. Li, "News text classification based on improved Bi-LSTM-CNN," in *Proceedings of the 9th International Conference on Information Technology in Medicine and Education*, pp. 890–893, Hangzhou, China, October 2018.
- [32] X. Han, J. Wang, M. Zhang, and X. Wang, "Using social media to mine and analyze public opinion related to COVID-19 in China," *International Journal of Environmental Research and Public Health*, vol. 17, no. 8, p. 2788, 2020.
- [33] H. Xuan Huynh, V. T. Nguyen, N. Duong-Trung, V.-H. Phan, and C. T. Phan, "Distributed framework for automating opinion discretization from text corpora on facebook," *IEEE Access*, vol. 7, pp. 78675–78684, 2019.
- [34] L. Bencke, C. Cechinel, and R. Munoz, "Automated classification of social network messages into smart cities dimensions," *Future Generation Computer Systems*, vol. 109, pp. 218–237, 2020.
- [35] E. D'Andrea, P. Ducange, A. Bechini, A. Renda, and F. Marcelloni, "Monitoring the public opinion about the vaccination topic from tweets analysis," *Expert Systems with Applications*, vol. 116, pp. 209–226, 2019.
- [36] Y. Zhang, Z. Yu, C. Mao, Y. X. Huang, and S. X. Gao, "Correlation analysis of law-related news combining bidirectional attention flow of news title and body," *Journal of Intelligent and Fuzzy Systems*, vol. 40, no. 3, pp. 5623–5635, 2021.
- [37] Jieba, "Chinese word segmentation tool," 2012, <https://github.com/fxsjy/jieba>.
- [38] T. Mikolov, K. Chen, G. S. Corrado, and J. Dean, "Efficient estimation of word representations in vector space," in *Proceedings of the 2013 International Conference on Learning Representations*, Scottsdale, Arizona, U.S, 2013, <https://arxiv.org/abs/1301.3781>.

Research Article

3D Mechanical Characters and Their Fabric Evolutions of Granular Materials by DEM Simulation

Xuefeng Li ^{1,2}, Weinan Lu ¹ and Yuqi He ¹

¹School of Physics and Electronic-Electronic Engineering, Ningxia University, Yinchuan 750021, China

²Solid Mechanics Institute, Ningxia University, Yinchuan 750021, China

Correspondence should be addressed to Xuefeng Li; lixuefeng1928@163.com

Received 20 March 2022; Accepted 15 June 2022; Published 9 August 2022

Academic Editor: Faisal Shabbir

Copyright © 2022 Xuefeng Li et al. This is an open access article distributed under the Creative Commons Attribution License, which permits unrestricted use, distribution, and reproduction in any medium, provided the original work is properly cited.

To quantitatively describe the influence of the contact characteristics of granular materials on their mechanical response, the true-triaxial tests with different particle shapes are simulated by the discrete element method (DEM), and the connection between the evolutions of particle contact fabric and the anisotropic mechanical responses is studied. The contact normal vector of the particle in 3D space is described by two independent angles, by which the contact fabric tensor is defined. The amplitude parameters in three orthogonal directions are defined by the invariants of the plane fabric tensor, which are scalars and describe the degree of anisotropy of the contact fabric in each plane. The expression of orthotropic fabric tensor is derived from the amplitude parameters, with the change of geometric space of contact normal vector, which is reduced to the different tensor of transverse isotropic naturally. The fabric tensor can be directly applied to the constitutive equation to describe the effects of the particle contact on the mechanical response. For verifying the rationality of contact characteristics described by fabric tensor, four particle shapes are clumped by PFC^{3D}. The mechanical properties of specimens with different particles are simulated under the true-triaxial loading path, and the data of contact normal vector is extracted in real time. The simulation results showed that the particle shapes have a significant effect on the 3D stress-strain relationship and strength, which showed apparent anisotropy, and the invariants of fabric tensor can be used to describe the evolution of particle contact in the loading process.

1. Introduction

Due to the unique properties of granular materials, such as dispersion, for a long time, their macroscopic mechanical properties and microscopic mechanical properties are often studied separately. Taking geotechnical engineering as an example, the strength and stability of granular materials in slope, foundation, and underground engineering studies from a macroscopic perspective can often meet engineering needs. However, under complex stress conditions such as cyclic loading, the failure's forms are quite different macroscopically, due to anisotropy, strain localization, strain softening, etc. The fundamental reason for these phenomena is the microscopic properties of the material, such as particle morphology, motion, fabric, and evolution [1–4]. Therefore, it is of theoretical and practical significance to study the

relationship between macroscopic and microscopic mechanical properties of granular materials [5–9].

Fabric tensor is a great connection tool for granular materials, and quantitative description is helpful in revealing the influence of microscopic fabric on macroscopic mechanical properties [10]. Since Oda et al. [11–13] put forward the definition of fabric tensors, the study on the mechanical properties of granular materials has gone from macroscopic to microscopic, and several constitutive models and strength criteria based on fabric tensors have been established. Guo [14] and Yao and Kong [15] established the strength criterion of granular materials using fabric tensors. Ouadfel and Rothenburg [16] researched the relationship of the stress-force-fabric. Liu et al. [17] presented the relationship between macroscopic stress, microscopic contact force, and anisotropic fabric. Petalas et al. [18] introduced fabric

anisotropy parameters into the constitutive model and studied the influence of fabric anisotropy evolution on mechanical properties. Pouragha et al. [19] combined the contact force, contact direction, and strength criterion between particles. Hu et al. [20] presented a boundary surface model containing fabric tensors, in which the anisotropy was represented by introducing back stress opposite to the contact normal direction and contrasted the predicted results of the model between simulation results by DEM. The author of this paper also established the potential theory [21] and the strength criterion [22] using the fabric tensor [23].

The above research results enrich the description performance and scope of the existing constitutive models and strength criteria based on fabric tensors. However, the characteristics of macroscopic and microscopic connections and their evolutions under complex stress conditions need to be further studied, such as the relationship between the evolution of contact fabric and macroscopic stress-strain change [24], and the relationship with the evolution of stress-induced anisotropy [25]. In the loading process, the evolution of the particle contact normal determines the evolution direction of macroscopic deformation to a certain extent. Liu et al. [26] studied the influence of stress path on fabric evolution by analyzing the evolution of partial fabric. Zheng et al. [27] studied the relationship between strength and fabric evolution. Hu et al. [28] studied the relationship between strain rate and fabric evolution. Nie et al. [29] believed that particle shape was also one of the factors affecting the evolution of fabric. Ng [30] and Oda et al. [31, 32] found that the contact normal direction between particles tended to be consistent with the maximum principal stress direction. Gu et al. [33] analyzed the evolutions of mechanical quantities such as contact number, contact force, and anisotropic parameters between particles. Vijayan et al. [34] studied the evolution of fabric and the average coordination number in the shearing process of granular materials. Wang et al. [35] and Zhou et al. [36] believed that the initial fabric influenced the evolutions of fabric.

The true-triaxial test can determine the macroscopic mechanical properties of granular materials in the 3D space and combine them with the measurement of the materials' microscopic particle information. We can explain the mechanism of the macro-microscopic relations. Under the true-triaxial condition, the granular materials in the stress state of nonhydrostatic pressure lead to stress-induced anisotropy [37–40], which is helpful in studying the loading influences on contact fabric anisotropy [41–44]. In practice, granular materials are composed of many irregular particles and voids. It is difficult to quantify their contact properties, especially during loading. DEM is a widely used discontinuous method [45–47], which can better simulate the macroscopic mechanical response of different particle morphology materials under complex loading conditions and, at the same time, can extract the microscopic characteristics of the contact in real time. Therefore, it is more suitable for studying the mechanical properties of granular materials from the macroscopic and microscopic perspectives [48–50]. Suhr and Six [51] studied the relationship between particle shapes and fabric evolution by DEM.

Dorostkar et al. [52], Yuan et al. [53], and Sazzad and Suzuki [54] used DEM to simulate a triaxial test and believed that loading with different ratios in three orthogonal directions had a significant influence on the evolution of anisotropic fabric. He and Jiang [55] conducted a true-triaxial simulation and analyzed the influence of intermediate principal stress coefficient (b) for fabric tensor. The above research has laid an excellent foundation for granular materials' macro-microscopic relations and evolutions.

In this paper, the influence of the four particle shapes on the macroscopic and microscopic properties of granular materials and the evolution trend of anisotropic fabric will be studied under the condition of true three-dimensional. Based on the author's research on fabric tensor, the contact fabric tensor will be defined by the normal vector of the contact point, and three amplitude parameters of the orthogonal direction can be defined with the invariant of the fabric tensor. Then, the expression of the orthotropic contact fabric with scalar parameters can be derived. The influence of particle shapes on the strength of granular materials will be analyzed by extracting the stress-strain relationship, peak internal friction angle, and other mechanical parameters. The evolution of anisotropic fabric and the relationship between microscopic fabric and macroscopic stress can be explored by extracting contact fabric, contact number of points, contact force, and other statistics of the contact points.

2. Contacts Fabric

As one of the three granular material fabrics, the contact fabric describes the statistical characteristics of the normal direction at the contact points. The force inside the material is transmitted by the contact point on the microscopic scale, for the complexity of the spatial distribution of the contact points caused different forces in a different direction, which shows anisotropy on a macroscopic scale. The degree of anisotropy is related to the contact direction between particles.

2.1. The Definition of Fabric. To describe the pattern of particle-to-particle contact direction, Oda et al. [11–13] and Tobita and Kuhn [56] have defined the expression of the second-order fabric tensor as

$$F_{ij} = \frac{1}{2N} \sum_{k=1}^{2N} n_i^{(k)} n_j^{(k)}, \quad (i, j = 1, 2, 3), \quad (1)$$

where N is the number of the particle, and $n_i^{(k)}$ and $n_j^{(k)}$ are the components of the unit contact normal vector on the coordinate axis, respectively.

2.2. Definition of Amplitude Parameters of Orthogonal Planes. Two independent angles can represent the components of the contact normal vector on three orthogonal axes. Take a certain contact point as an example, at the contact point, one angle between the contact normal vector and the x_1 axis is $\theta_1^{(k)}$, the other between the projection on the horizontal

plane and the x_3 axis is $\alpha^{(k)}$, and then the direction vector of equation (1) is

$$n = \{\cos(\theta_1^{(k)}), \sin(\theta_1^{(k)})\sin(\alpha^{(k)}), \sin(\theta_1^{(k)})\cos(\alpha^{(k)})\}. \quad (2)$$

It is difficult to analyze the three-dimensional fabric of sand, so it is necessary to use two-dimensional graph analysis and then carry out reasonable three-dimensional. According to equations (1) and (2), the expression on the orthogonal plane is

$$\bar{F}_{ij} = \begin{bmatrix} \bar{F}_{11} & \bar{F}_{13} \\ \bar{F}_{31} & \bar{F}_{33} \end{bmatrix} = \begin{bmatrix} \frac{1}{2N} \sum_{k=1}^{2N} \sin^2(\theta^{(k)}) & \frac{1}{2N} \sum_{k=1}^{2N} \cos(\theta^{(k)})\sin(\theta^{(k)}) \\ \frac{1}{2N} \sum_{k=1}^{2N} \cos(\theta^{(k)})\sin(\theta^{(k)}) & \frac{1}{2N} \sum_{k=1}^{2N} \cos^2(\theta^{(k)}) \end{bmatrix}, \quad (4)$$

where \bar{F}_{ij} is a second-order plane-symmetric tensor, and $\theta^{(k)}$ is the angle between the x_1 - x_3 plane and the x_3 axis projection. As the properties of plane-symmetric stress, the plane fabric tensor can also be described by its invariant. The two principal values of the \bar{F}_1 and \bar{F}_3 can be expressed as

$$\bar{F}_{1,3} = \frac{1}{2} (\bar{F}_{11} + \bar{F}_{33}) \pm \left[\frac{1}{4} (\bar{F}_{11} - \bar{F}_{33})^2 + \bar{F}_{13}^2 \right]^{1/2} = \frac{1}{2} \pm \frac{a_1}{2}, \quad (5)$$

$$F_{ij} = \frac{1}{2N} \sum_{k=1}^{2N} n_i^{(k)} n_j^{(k)} \quad (i, j = 1, 2). \quad (3)$$

In the interior of granular materials, the particles are in contact with each other, and the directions of the contact normal vector are normally positively distributed. The two angles can also represent the projection components of particles onto three orthogonal planes. For example, on the plane of x_1 - x_3 , the 2D fabric tensor can be expressed as

where, according to the fabric tensor definition, the trace of F_{ij} is equal to 1, so the direction vector describes a scalar parameter a_1 in equation (5) as

$$a_1 = \frac{1}{2N} \sqrt{\left(\sum_{k=1}^{2N} (\cos^2(\theta_1^{(k)}) - \sin^2(\theta_1^{(k)})\cos^2(\alpha^{(k)})) \right)^2 + \left(\sum_{k=1}^{2N} \sin(2\theta_1^{(k)})\cos(\alpha^{(k)}) \right)^2}, \quad (6)$$

where a_1 is the anisotropic amplitude parameter of contact normal fabric, which describes the statistical probability distribution of the normal direction of the contact point. According to the theoretical definition, a_1 value range is $[0, 1]$.

Similarly, the amplitude parameters of x_1 - x_2 plane and x_2 - x_3 plane can be obtained as follows:

$$a_2 = \frac{1}{2N} \sqrt{\left(\sum_{k=1}^{2N} (\cos^2(\theta_1^{(k)}) - \sin^2(\theta_1^{(k)})\sin^2(\alpha^{(k)})) \right)^2 + \left(\sum_{k=1}^{2N} \sin(2\theta_1^{(k)})\sin(\alpha^{(k)}) \right)^2}, \quad (7)$$

$$a_3 = \frac{1}{2N} \sqrt{\left(\sum_{k=1}^{2N} \sin^2(\theta_1^{(k)})\cos(2\alpha^{(k)}) \right)^2 + \left(\sum_{k=1}^{2N} \sin^2(\theta_1^{(k)})\sin(2\alpha^{(k)}) \right)^2}. \quad (8)$$

As shown in Figure 1, a_1 , a_2 , and a_3 are the anisotropic amplitude parameters on three orthogonal planes, such as

F_{x1} - F_{x3} , F_{x1} - F_{x2} , and F_{x2} - F_{x3} . Three parameters can be determined by the normal vector of all particle contact

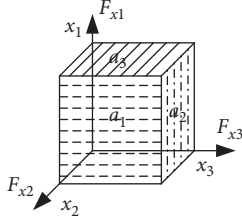


FIGURE 1: The schematic diagram for determining the amplitude parameters of orthogonal fabrics.

points from equations (6)–(8), and the range of the three parameters is 0~1, describing the anisotropy degree of materials on each surface.

According to the fabric definition, the trace of the fabric tensor is equal to 1. There are only two independent variables among the three amplitude parameters on the orthogonal planes. Hence, the fabric tensor F_{ij} ($i, j = 1, 2, 3$) can be derived from any two of three amplitude parameters defined by equations (6)–(8). This paper uses the orthotropic fabric tensor derived from reference [20]. For a detailed derivation process, refer to reference [57].

$$F = \begin{bmatrix} \frac{1 + a_1 + a_2 + a_1 a_2}{3 + a_1 + a_2 - a_1 a_2} & 0 & 0 \\ 0 & \frac{1 + a_1 - a_2 - a_1 a_2}{3 + a_1 + a_2 - a_1 a_2} & 0 \\ 0 & 0 & \frac{1 - a_1 + a_2 - a_1 a_2}{3 + a_1 + a_2 - a_1 a_2} \end{bmatrix}, \quad (9)$$

$$F = \begin{bmatrix} \frac{1 + a_1 - a_3 - a_1 a_3}{3 - a_1 - a_3 - a_1 a_3} & 0 & 0 \\ 0 & \frac{1 - a_1 + a_3 - a_1 a_3}{3 - a_1 - a_3 - a_1 a_3} & 0 \\ 0 & 0 & \frac{1 - a_1 - a_3 + a_1 a_3}{3 - a_1 - a_3 - a_1 a_3} \end{bmatrix}. \quad (10)$$

In equation (9), when $\alpha^{(k)} = \pi/4$, $\sin \alpha^{(k)} = \cos \alpha^{(k)}$, then $a_1 = a_2$. The amplitude parameters of vertical planes and in the horizontal direction are equal. Then, the materials are shown as transversely isotropic, and then equation (9) is degraded to transversely isotropic fabric:

$$F_{ij} = \frac{1}{3 - a_1'} \begin{bmatrix} 1 + a_1' & 0 & 0 \\ 0 & 1 - a_1' & 0 \\ 0 & 0 & 1 - a_1' \end{bmatrix}, \quad (11)$$

where

$$a_1' = \frac{1}{2N} \sqrt{\left(\sum_{k=1}^{2N} \left(\cos^2(\theta_1^{(k)}) - \frac{\sin^2(\theta_1^{(k)})}{2} \right) \right)^2 + \frac{1}{2} \left(\sum_{k=1}^{2N} \sin(2\theta_1^{(k)}) \right)^2}, \quad (12)$$

where a_1' is the amplitude parameter after degradation of a_1 and a_2 , and the a_1' value range is [0, 1].

In equation (10), an amplitude parameter is obtained according to any one of the two planes that can be used to describe the transverse isotropy of natural soil, and the amplitude parameter value can be obtained by equation (12). In equation (10), if $\theta_1^{(k)} = \pi/2$ in equation (6) and $\alpha^{(k)} = 0$ in equation (8), then $a_1 = a_3$. Equation (10) has degenerated into the transversely isotropic form.

$$F_{ij} = \frac{1}{3 + a_3'} \begin{bmatrix} 1 + a_3' & 0 & 0 \\ 0 & 1 + a_3' & 0 \\ 0 & 0 & 1 - a_3' \end{bmatrix}, \quad (13)$$

where

$$a_3' = \frac{1}{2N} \sqrt{\left(\sum_{k=1}^{2N} \cos(2\theta^{(k)}) \right)^2 + \left(\sum_{k=1}^{2N} \sin(2\theta^{(k)}) \right)^2}, \quad (14)$$

where a_3' is the amplitude parameter after degradation of a_1 and a_3 .

Equation (14) is the same as the formula proposed by Oda [13, 58] if the variable satisfies $\theta^{(k)} = \pi/2 - \theta_1^{(k)}$. Equation (13) is the only expression that quantitatively describes the fabric tensor of particle orientation at present. It has been widely used in both quantitative tests and macro-microscopic mechanical models. The difference is that equation (13) is derived from the 3D definition of fabric, while the expression of Oda [13, 58] is derived directly from the assumption of transverse isotropy.

3. True-Triaxial Test Simulations by PFC^{3D}

3.1. Generation of Nonspherical Particles. In DEM, spherical particle (3D) with different diameters is used, which is too ideal to describe the natural geometry of granular materials, especially when the microscopic particle characteristics are used to describe the influence of their fabric on macroscopic mechanism. Therefore, the four particle shapes, that is, spheres, elongate clump, pyramid clump, and cube clump (Figure 2), are used to establish a true-triaxial specimen, respectively, and bonding 1~4 spherical particles generate the clumps. In order to distinguish the differences in the geometric shapes of particles, Yang and Luo [59] defined the overall regularity value to describe the geometric characteristics of the particles. The smaller the value is, the more complex the particle morphology is. The overall regularity values for spherical, ellipsoid, pyramidal, and cubic particles are 1, 0.91, 0.88, and 0.89, respectively.

Elongate, pyramid, and cube clumps are used to replace spherical particles with clamp function. Figure 3 shows replacing a single spherical particle with an elongate clump. It should be pointed out that particle replacement is carried out one by one in which particles are arranged. In the process of particle replacement, only the particle shape is changed, but other material parameters of the particle are not changed, and the volume of the DEM model is constant during the process of generation irregular particles.

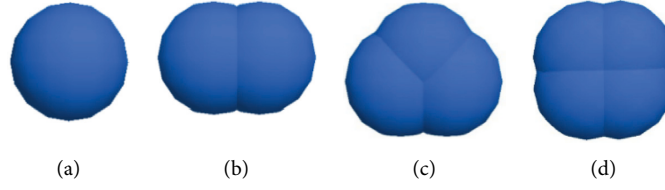


FIGURE 2: The four particle shapes in the specimens. (a) Spherical. (b) Elongate clump. (c) Pyramid clump. (d) Cube clump.

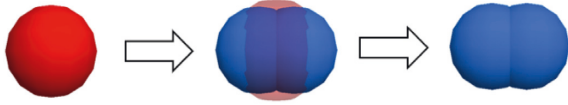


FIGURE 3: Particle replacement process.

3.2. Simulation Processes. In this paper, the rectangular models are established with a ratio of length, width, and height of 1 : 1:2 (Figure 4). Rigid walls are set on six faces of the models (the boundaries are the rigid boundaries) [60, 61]. The contact model is linear. The friction coefficient between particles is 0.4, and the friction coefficient between particles and the rigid walls is 0. According to the target porosity of 0.35, 12000 spherical particles are generated in the model with the random distribution method. The spherical particle parameters are adopted in Table 1.

In true-triaxial test simulations, intermediate principal stress coefficient $b = (\sigma_2 - \sigma_3)/(\sigma_1 - \sigma_3)$ and mean normal stress $p = (\sigma_1 + \sigma_2 + \sigma_3)/3$ are required to be kept constant throughout the loading process, and then the loading path in the three principal directions is

$$\begin{cases} d\sigma_1 = d\sigma_1, \\ d\sigma_2 = \frac{1-2b}{b-2}d\sigma_1, \\ d\sigma_3 = \frac{1+b}{b-2}d\sigma_1, \end{cases} \quad (15)$$

where $d\sigma_1$, $d\sigma_2$ and $d\sigma_3$ are the increments of σ_1 , σ_2 , and σ_3 respectively. For ease of understanding, Figure 5 is the schematic of the loading.

In the true-triaxial simulation test, isotropic consolidation is applied earlier, and then shearing is conducted. For isotropic consolidation, 500 kPa confining pressure σ_c ($\sigma_c = p$) is applied to the six rigid walls. The model gradually achieved stress equilibrium under the confining pressure, and the first figure in Figure 5 shows the isotropic consolidation. Then, the vertical downward velocity is applied to the rigid wall at the top of the model, and compressive stress is increased on the rigid walls at the four sides of the model. In other words, under the condition of $\sigma_c = 500$ kPa, $d\sigma_1$ is loaded in the vertical direction, and then four lateral stress increments are obtained by the relationship between $d\sigma_2$, $d\sigma_3$ and $d\sigma_1$ (equation (15)). The shearing process ended when the vertical strain ε_1 reached 20%. The shearing process can be shown in the second picture of Figure 5. The test

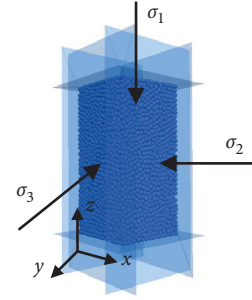


FIGURE 4: Schematic of the true-triaxial specimen.

schemes are shown in Table 2. The stress paths of the tests are constant p and b .

3.3. Influences of Particle Shapes on the Strength. For obtaining the influences of the particle shapes on macroscopic strength, a true-triaxial test is carried out by PFC^{3D}. Figure 6 shows the stress-strain relationships of the specimens of the four particle shapes under the same b . The purpose is to get the variation of generalized shear stress $q = \sqrt{((\sigma_1 - \sigma_2)^2 + (\sigma_2 - \sigma_3)^2 + (\sigma_3 - \sigma_1)^2)}/2$. The horizontal axis of the curves is the vertical strain ε_1 of the specimens in Figure 6.

It can be seen from Figure 6 that the strain softening and hardening characteristics of the same particle shape increase with the increase of b . The more complex the particle shape is under the same b , the greater the stress-strain relationship's influence is. The spherical particle specimen has the most significant slope in the strain softening process, and the pyramids have the slightest slope. This law is consistent with the experimental and simulation results carried out by Yang and Luo [59], Jerves et al. [62], and Lashkari et al. [63].

Figures 7 and 8 show the relationships between the peak strength (q_{\max}) and peak internal friction angle (φ_{\max}) of the four particle shapes with different b , respectively. The peak strength and the peak internal friction angles are the maximum values of the generalized shear stress and the internal friction angle, which can be expressed as $\sin \varphi = (\sigma_1 - \sigma_3)/(\sigma_1 + \sigma_3)$. The results of all the specimens in Figure 7 show a monotonous decreasing trend of q_{\max} with the increase of b , which is consistent with the true-triaxial test trend of granular materials. Moreover, with the complexity of particle shapes increasing, the q_{\max} is greater at the same b . Similarly, the relationships between the φ_{\max} and b in Figure 8 are also consistent with the test results of granular materials. The φ_{\max} increases and then decreases.

TABLE 1: The parameters used in DEM simulation.

Density/ ρ (kg/m ³)	Modulus of elasticity E (MPa)	Normal contact stiffness K_n (N/m)	Normal to tangential stiffness ratio	Damping coefficient	Particle radius d (mm)
1600	20	1×10^8	2.00	0.7	1.8~2.5

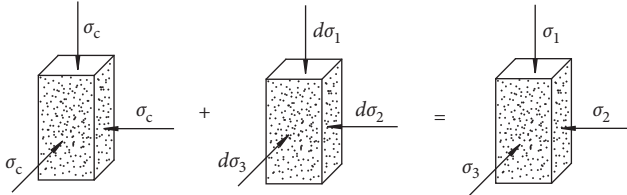


FIGURE 5: Schematic illustration of the loading process.

TABLE 2: Schemes of true-triaxial simulation.

Particle shapes	Intermediate principal stress coefficient b	Mean normal stress p (kPa)
Spherical		
Elongate clump	0, 0.2, 0.4, 0.6, 0.8, 1	500
Pyramid clump		
Cube clump		

With the particle shapes becoming complex, this trend became more apparent. Some existing research has also reached similar conclusions. The specimens of spherical particles have a lower friction angle and shear strength [64]. Some experiments and simulations revealed that granular materials comprising irregular particles usually have higher macroscopic shear strength at a given stress path [65, 66].

3.4. Stress Path and Fabric Variations. The evolution of the fabric in three principal directions is extracted during the test under the true-triaxial stress path. From shear to failure, F_{11} first increases, decreases, and then stabilizes. The rules are the same as the pattern of stress-strain relationship from hardening, peaking to softening, finally. Oda et al. [32] conclude that the contact normal tends to align in the maximum principal stress direction to resist greater external forces during the shearing. Ultimately, the main direction of the fabric will be consistent with the direction of principal stress. Due to space limitations, this article only gives the data at the critical state.

Figure 9(a) shows the true-triaxial stress path of pressure control, and Figure 9(b)~9(e) shows the evolutions of the principal fabric components of the four particle shapes at the peak state. With the variations of b , F_{11} and F_{33} gradually decrease, while F_{22} increases. The evolutions of contact fabric at the peak state are consistent with the true-triaxial test of stress path under the constant b and p . The varying degree of the principal fabric with spherical particles is far less than that of other nonspherical particles, and the contact fabric changes continuously as the stress. The more complex

the particle shape is, the greater the discontinuity of the fabric is when $b = 1$. It can be found that the complexity of particle shapes directly affected the evolutions of the contact normal vector.

It can be seen from Figure 6 that the strain softening and hardening characteristics of the same particle shape increase with the increase of b . The more complex the particle shape is under the same b , the greater the stress-strain relationship's influence is. The spherical particle specimen has the most significant slope in the strain softening process, and the pyramids have the slightest slope. This law is consistent with the experimental and simulation results carried out by Yang and Luo [59], Jerves et al. [62], and Lashkari et al. [63].

Figures 7 and 8 show the relationships between the peak strength (q_{\max}) and peak internal friction angle (φ_{\max}) of the four particle shapes with different b , respectively. The peak strength and the peak internal friction angles are the maximum values of the generalized shear stress and the internal friction angle, which can be expressed as $\sin \varphi = (\sigma_1 - \sigma_3) / (\sigma_1 + \sigma_3)$. The results of all the specimens in Figure 7 show a monotonous decreasing trend of q_{\max} with the increase of b , which is consistent with the true-triaxial test trend of granular materials. Moreover, with the complexity of particle shapes increasing, the q_{\max} is greater at the same b . Similarly, the relationships between the φ_{\max} and b in Figure 8 are also consistent with the test results of granular materials. The φ_{\max} increases and then decreases. With the particle shapes becoming complex, this trend became more apparent. Some existing research has also reached similar conclusions. The specimens of spherical particles have a lower friction angle and shear strength [64]. Some experiments and simulations revealed that granular materials comprising irregular particles usually have higher macroscopic shear strength at a given stress path [65, 66].

3.5. Evolutions of Fabric. Both inherent anisotropy and stress-induced anisotropy are closely related to the microscopic properties of the granular materials. Casagrande and Carillo [67] first discriminate the difference between them. The sedimentation of a particle will trigger inherent anisotropy, while the induced anisotropy is mainly caused by nonelastic deformation [68]. Oda et al. [32] revealed that induced anisotropy is mainly produced by changing the distribution of internal contact normal of materials. The four particle shapes can make different inherent anisotropic specimens in our simulation. Changing the loading ratio of the three main directions of the specimen can simulate stress-induced anisotropy. The relationships between the two anisotropies can be explored by analyzing the particle contact evolution data.

Based on the simulation results above, it is considered that F_{ij} evolutions of granular materials are the function of

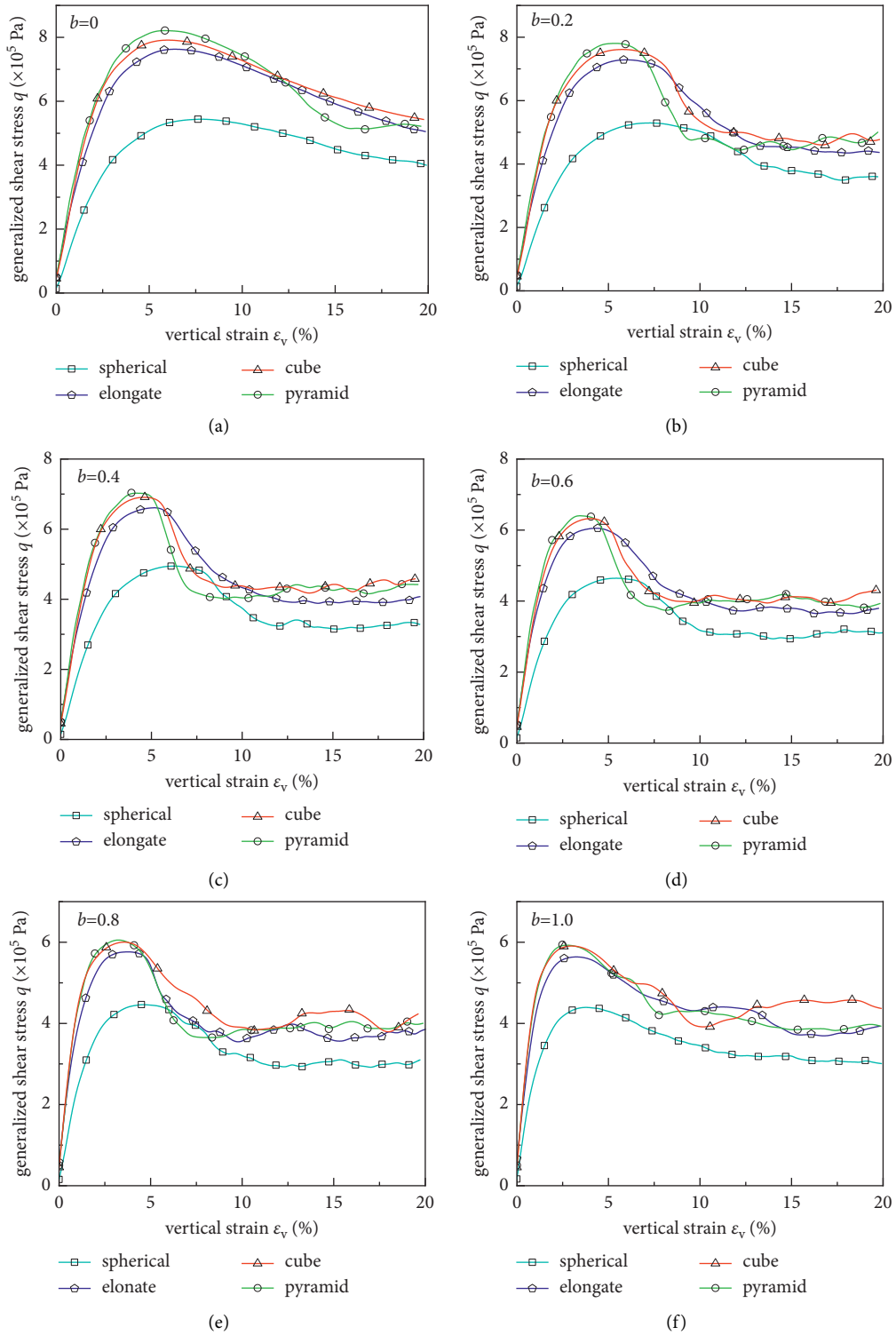


FIGURE 6: Stress-strain relationships with the four particle shapes under different intermediate principal stress coefficients. (a) $b=0$ (b) $b=0.2$ (c) $b=0.4$ (d) $b=0.6$ (e) $b=0.8$ (f) $b=1.0$.

principal stress. Hu et al. [69] and Lashkari and Norouzi [70] all established the relationship between stress ratio and fabric evolution in order to analyze the distribution of fabric evolution and anisotropy. In this paper, the relationship between the fabric tensor and the deviatoric stress ratio

suggested by Guo et al. [14] is used to analyze the law of fabric evolution. Guo [14] supposed that F_{ij} is proportional to the components of the deviatoric stress ratio tensor:

$$dF_{ij} = \lambda d\eta_{ij}, \quad (16)$$

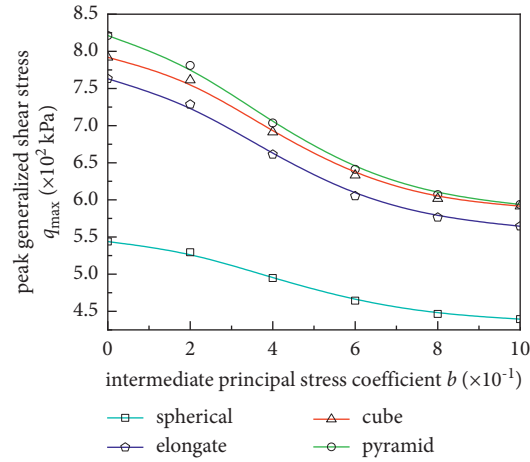


FIGURE 7: Relationships between peak strength and intermediate principal stress coefficient with the four particle shapes.

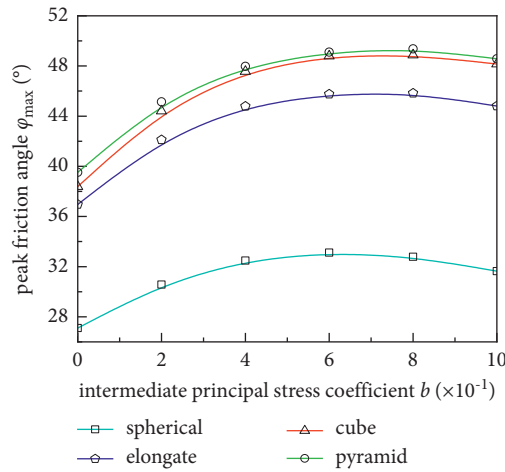


FIGURE 8: Evolutions of peak friction angle with intermediate principal stress coefficient with the four particle shapes.

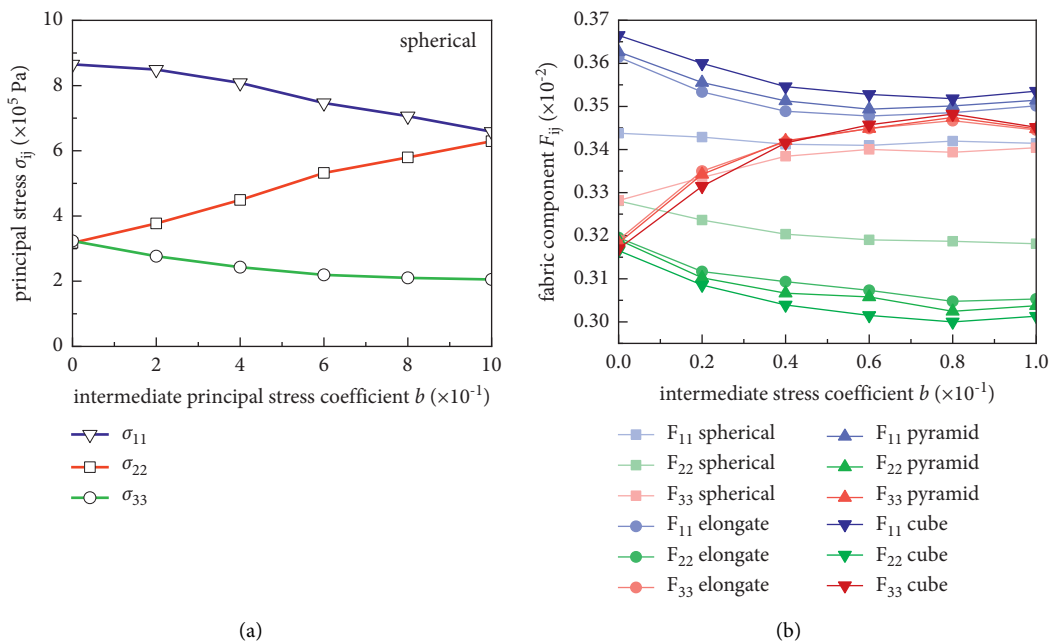


FIGURE 9: Evolutions of principal stresses and fabric components with intermediate principal stress coefficient. (a) The stress of true triaxial test at the critical state. (b) The fabric of the true triaxial test at the critical state.

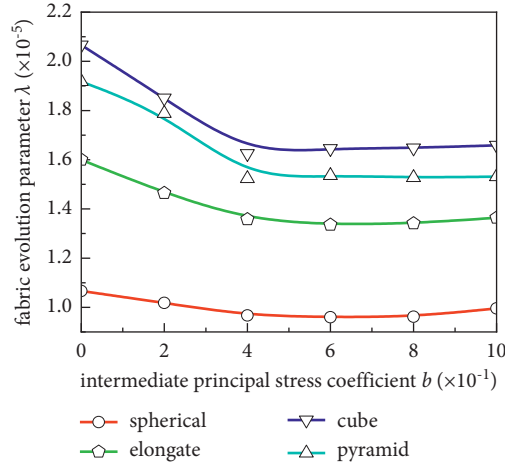


FIGURE 10: Evolutions of fabric evolution parameter with the intermediate principal stress coefficient.

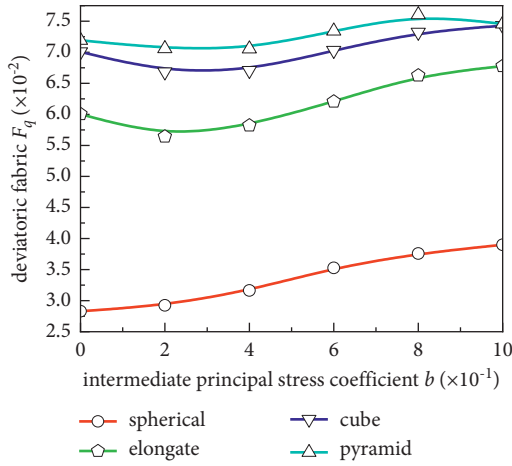


FIGURE 11: Evolutions of deviatoric fabric with intermediate principal stress coefficient.

where λ is a fabric evolution parameter that could describe the stress-fabric relationship, $d\eta_{ij}$ denotes deviatoric stress ratio, $d\eta_{ij} = d(s_{ij}/p)$, s_{ij} is deviatoric stress tensor, and $s_{ij} = \sigma_{ij} - p\delta_{ij}$, δ_{ij} is Kronecker notation. Under constant p loading, p is a constant, so equation (16) can be turned into

$$dF_{ij} = \lambda d \frac{\sigma_{ij} - p}{p} = \lambda \frac{d\sigma_{ij}}{p}. \quad (17)$$

We can get the fabric-stress evolution relationship by integrating equation (17):

$$F_{ij} = \frac{\lambda}{p} \sigma_{ij} + C, \quad (18)$$

where C is an arbitrary constant. Assume that the sample has an initial fabric $F_{ij}|_0$ in the isotropic state, and then equation (18) can be written as

$$F_{ij} = \frac{\lambda}{p} \sigma_{ij} + F_{ij}|_0. \quad (19)$$

For the initial isotropic sample, the initial fabric is equal to $1/3$. The fabric evolution parameter λ of granular material can be calculated by substituting $F_{ij}|_0 = 1/3$ into equation (19). The experimental evidence by Oda et al. [32] revealed that induced anisotropy is mainly produced by changing the distribution of internal contact of materials. To describe the effect of fabric evolution on anisotropy, we used the invariant of fabric tensor as a reference quantity as follows:

$$F_q = \frac{\sqrt{2}}{2} \sqrt{(F_{11} - F_{22})^2 + (F_{22} - F_{33})^2 + (F_{11} - F_{33})^2}. \quad (20)$$

Figure 10 shows the variation of λ of the four particle shapes with different b at the peak state. When the b is small, the change rate of the λ - b curve of spherical particles is small, while the change rate of cubic and pyramidal particles is larger. When the b is larger, the rate of change of λ - b curves of different shapes is approximately constant. The overall change of λ is smaller and around 1. For the nonspherical particle, λ decreased first as b increased, and it decreased slowly after $b=0.6$; then, the rate of change tends to be constant. The more irregular the particle shape is, the more considerable the λ is, and the more significant the reduction when $b < 0.6$. It can be seen that the spherical particle is easy to rotate in the loading process, but due to the regular shape, the spatial probability and distribution probability of the particle contact point tend to be even. However, for the nonspherical particles, with the change of particle shapes and principal stress loading ratio, the spatial distribution of the contact points is different, and the variation rules of fabric evolution parameters are quite different.

Figure 11 shows the evolutions of F_q with b of the four particle shapes in the peak state. The expression of F_q is the same as the expression of q , which is the second invariant of fabric and stress partial tensor, respectively. F_q can describe the degree of anisotropy of contact fabric. The greater the F_q is, the higher the degree of anisotropy is. For the spherical particles, F_q increases monotonously with b , which is contrary to the evolution that q changed with b in Figure 7. When the particle morphology becomes complicated, F_q

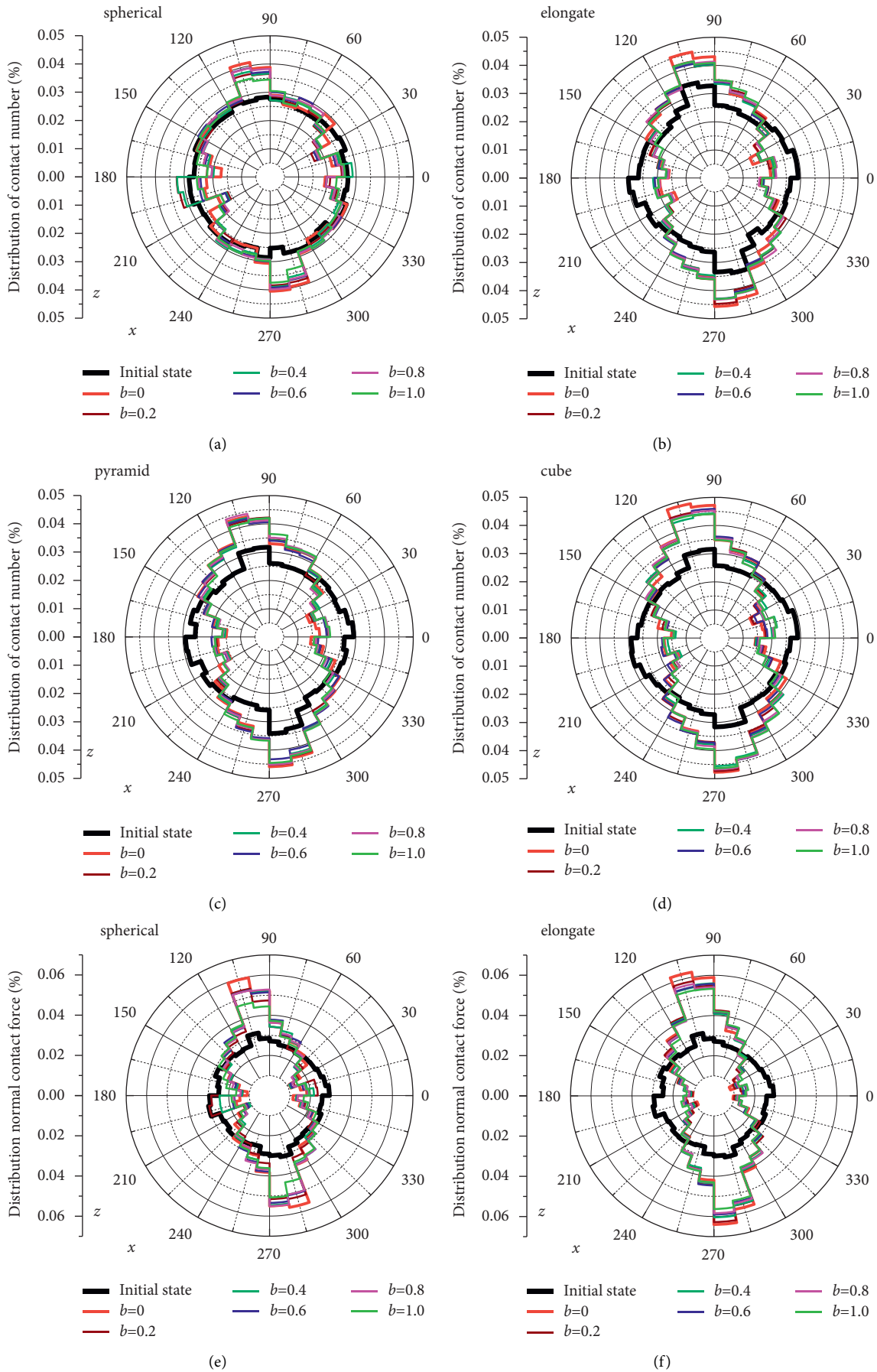


FIGURE 12: Continued.

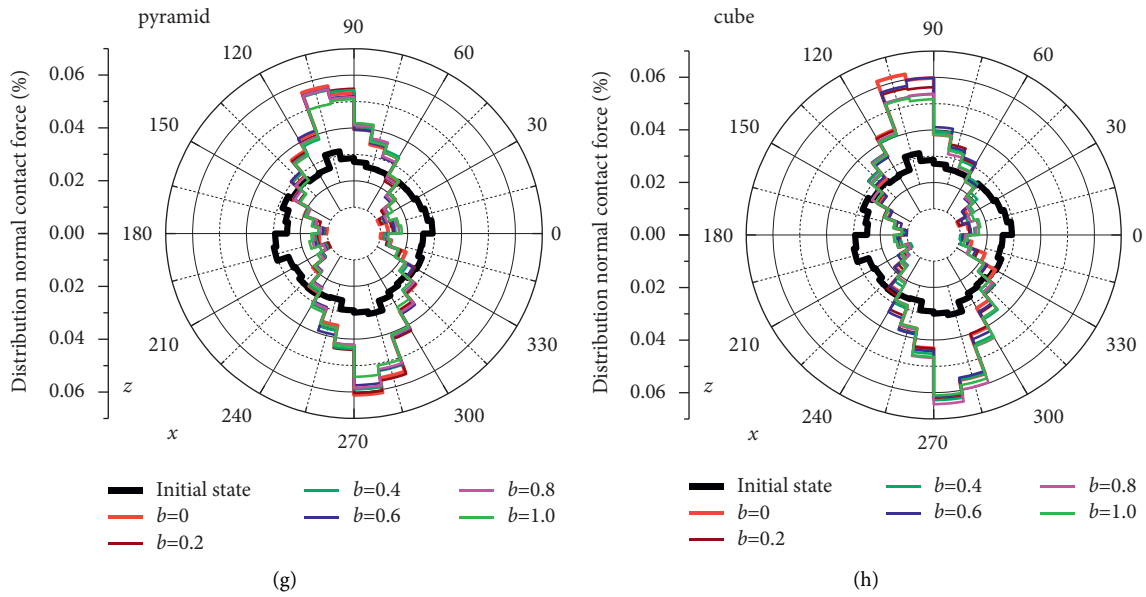


FIGURE 12: Rose diagrams of contact number and contact force. (a) Distribution of contact number of spherical. (b) Distribution of contact number of the elongate. (c) Distribution of contact number of the pyramid. (d) Distribution of contact number of the cube. (e) Distribution of contact force of the spherical. (f) Distribution of contact force of the elongate. (g) Distribution of contact force of the pyramid. (h) Distribution of contact force of the cube.

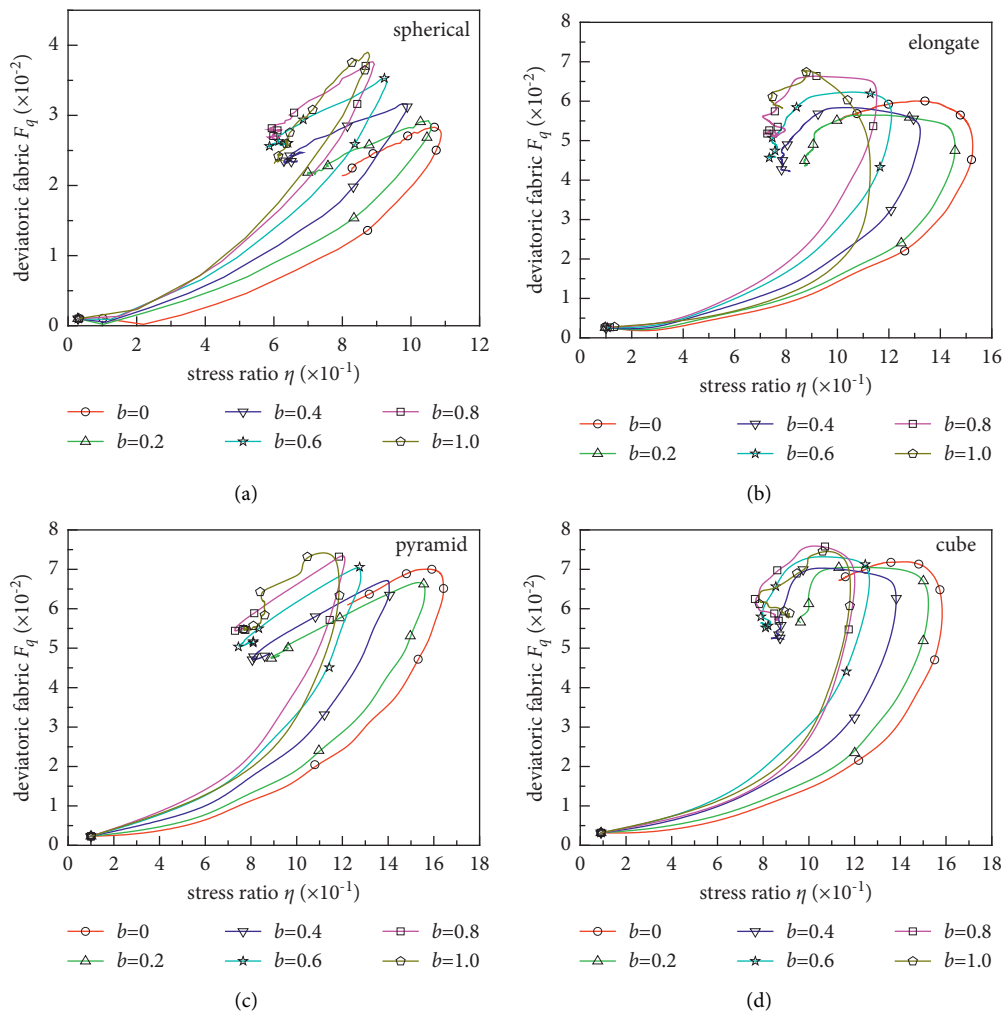


FIGURE 13: Evolutions of deviatoric fabric with stress ratio. (a) Evolutions of F_q with η of spherical specimens. (b) Evolutions of F_q with η of elongate specimens. (c) Evolutions of F_q with η of pyramid specimens. (d) Evolutions of F_q with η of cube specimens.

does not increase monotonously with b but shows a different anisotropy. Therefore, F_q can be used to quantify the evolution of fabrics caused by stress-induced anisotropy.

Figure 12 shows the rose diagram on the XZ plane of the distribution of contact number and contact force with the different b . The black curves in the figure are the distribution of contact characteristics after isotropic consolidation, and it can be seen that the curve is close to the isotropic distribution. Other curves show apparent anisotropy distribution, indicating that the contact fabric shows different degrees of anisotropy distribution under the conditions of different proportions, and that can directly reflect the stress-induced anisotropy. The distribution of contact numbers in Figure 12(a) and contact force in Figure 12(b) are similar for spherical particles, but the anisotropic degrees are different. There is a similar rule for other irregular particles, only to a different degree. This rule indicates that the magnitude of the force on the contact points aggravate the degree of anisotropy in the distribution direction of the same contact number. Therefore, a more reasonable method to describe the contact fabric is to consider the distribution of contact points' numbers and the contact force's magnitude.

Figure 13 shows the evolutions of F_q with stress ratio ($\eta = q/p$) of the four particle shapes. The results show that F_q and η are increased to peak point first and then reduced to a critical state under the stress path of constant p . F_q increases with the increase of b , and η decreases with the increase of b , which is consistent with the research results of Yuan and Yu [53]. As the irregularity of the particles increases, η and F_q will also gradually increase. The micro-macroscopic mechanical interpretation can be given as follows. Due to the uniform distribution of the fabric and the smoothness of spherical particle specimens, the particles are easy to rotate, so the shear stress is relatively lower, while for irregular particles, the spatial distribution of fabric is more complex, and particle movement requires greater stress. It is consistent with the observation that interlocking between spherical particles is more unstable than between angular particles in reference [71].

4. Conclusions

The normal direction of particle contact substantially influences the macroscopic mechanical properties of granular materials. In this paper, the true-triaxial tests with four particle shapes are simulated by DEM, the microscopic evolutions of a particle are studied using the novel defined fabric tensor, and the relationships between the evolution of contact fabric and the macroscopic mechanical behaviors are explored. The main conclusions are as follows:

- (1) The contact fabric tensor is defined by the contact normal vector, which describes the probabilistic and statistical laws of the contact characteristics of microscopic particles. Three amplitude parameters in the orthogonal direction are defined using the invariant of the plane fabric tensor, by which the scalar expression of orthotropic fabric is derived. With the change of the geometric relationship of the contact

points, the orthotropic fabric can naturally degenerate into different forms of transverse isotropy. The fabric tensor defined in this paper can be directly applied to the macroscopic constitutive equation.

- (2) The four particle shapes are constructed using PFC^{3D} software. Under the condition of the same parameters and loading paths of the true-triaxial test, simulation results show that particle morphology changes directly affect the anisotropy of the stress-strain relationship and the strength. The more complex the particle shape is, the more significant the influence on the anisotropy is. These showed the influence of particle morphology on the macro-mechanics of granular materials.
- (3) The contact characteristics of particles directly affect their macroscopic mechanical response. The contact fabric can be used to describe the contact characteristics and the evolution of particles. Under the true-triaxial loading path, the spherical particles are easy to rotate, the distributions of contact points are uniform, and the variations of fabric evolution parameters are small. Even if the three principal stress directions are loaded in different proportions, the effect on anisotropy is small. Irregular particles greatly influence the spatial distributions of contact points, and the more pronounced the fabric evolution is, the more the anisotropy changes. The distribution of contact points, contact force, and the evolution of the four particle shapes show that the distribution of particle contact points and the magnitude of the contact forces should be considered in the fabric tensor.

Abbreviations

F_{ij} ($i, j = 1, 2, 3$):	Second-order fabric tensor
N :	Number of the particle
$n_i^{(k)}, n_j^{(k)}$ ($i, j = 1, 2, 3$):	Components of the unit contact normal vector
x_1, x_2 , and x_3 :	Three orthogonal axes
$\theta_1^{(k)}$:	One angle between the contact normal vector and the x_1
$\alpha^{(k)}$:	One angle between the projection on the horizontal plane and the x_3
n :	Contact normal vector
\bar{F}_{ij} :	Second-order plane-symmetric tensor
$\theta^{(k)}$:	One angle between the x_1 - x_3 plane and the x_3 axis projection
\bar{F}_1, \bar{F}_3 :	Invariant of plane fabric tensor
a_1, a_2 , and a_3 :	Anisotropic amplitude parameter of contact normal fabric
F_{x1}, F_{x2} , and F_{x3} :	Three orthogonal axes of fabric
F :	Fabric tensor
a_1' :	Amplitude parameter after degradation of a_1 and a_2
ρ :	Density
E :	Modulus of elasticity
K_n :	Normal contact stiffness
d :	Particle radius

b :	Intermediate principal stress coefficient
p :	Mean normal stress
$d\sigma_1, d\sigma_2$ and $d\sigma_3$:	Increment of σ_1, σ_2 , and σ_3
σ_1, σ_2 , and σ_3 :	Maximum, intermediate, and minimum principal stress
σ_c :	Confining pressure
q :	Generalized shear stress
ε_i :	Vertical strain
q_{\max} :	Peak strength
φ_{\max} :	Peak internal friction angle
$\sigma_{ij} (i, j = 1, 2, 3)$:	Principal stress
$dF_{ij} (i, j = 1, 2, 3)$:	Deviatoric stress ratio tensor
λ :	Fabric evolution parameter
$d\eta_{ij} (i, j = 1, 2, 3)$:	Deviatoric stress ratio
$s_{ij} (i, j = 1, 2, 3)$:	Deviatoric stress tensor
$\delta_{ij} (i, j = 1, 2, 3)$:	Kronecker notation
C :	Arbitrary constant
$F_{ij} _0$:	Initial fabric
F_q :	Invariant of fabric tensor
η :	Stress ratio.

Data Availability

The data used to support the findings of this study are available from the corresponding author upon request.

Conflicts of Interest

The authors declare that there are no conflicts of interest regarding the publication of this paper.

Acknowledgments

The Projects that financially supported this work are Leading Talents of Science and Technology Innovation of Ningxia (No. KJT2019001), the National Natural Science Foundation of China (Nos. 12162028 and 51669027), and the Technology Innovation Team-Ningxia Hui Autonomous Region (Innovation Team - Multi-scale Mechanics and Engineering Applications), and these supports are gratefully acknowledged.

References

- [1] J. Zheng and R. D. Hryciw, "Cross-anisotropic fabric of sands by wavelet-based simulation of human cognition," *Soils and Foundations*, vol. 58, no. 4, pp. 1028–1041, 2018.
- [2] J. Fei, Y. Jie, X. Sun, and H. Xiong, "Physical interpretation of shear-rate behaviour of soils and geotechnical solution to the coefficient of start-up friction with low inertial number," *Scientific Reports*, vol. 10, no. 1, 2020.
- [3] M. Wiebicke, E. Andò, E. Salvatore, G. Viggiani, and L. Herle, "Experimental Measurement of Granular Fabric and its Evolution under Shearing," in *Proceedings of the EPJ web of conferences*, June 2017.
- [4] Y. Zhu, Z. Nie, J. Gong, J. Zou, L. Zhao, and L. Li, "An Analysis of the Effects of the Size Ratio and Fines Content on the Shear Behaviors of Binary Mixtures Using DEM," *Computers and Geotechnics*, vol. 118, 2020.
- [5] X. S. Li and Y. F. Dafalias, "Anisotropic critical state theory: role of fabric," *Journal of Engineering Mechanics*, vol. 138, 2012.
- [6] X. S. Li and Y. F. Dafalias, "Noncoaxiality between two tensors with application to stress rate decomposition and fabric anisotropy variable," *Journal of Engineering Mechanics*, vol. 146, 2020.
- [7] T. Qu, Y. T. Feng, Y. Wang, and M. Wang, "Discrete Element Modelling of Flexible Membrane Boundaries for Triaxial Tests," *Computers and Geotechnics*, vol. 115, 2019.
- [8] M. Jiang, A. Zhang, and C. Fu, "3-D DEM simulations of drained triaxial tests on inherently anisotropic granulates," *European Journal of Environmental and Civil Engineering*, vol. 22, pp. 37–56, 2017.
- [9] Y. Tobita, "Fabric tensors in constitutive equations for granular materials," *Soils and Foundations*, vol. 29, no. 4, pp. 91–104, 1989.
- [10] Y. Li, J. Li, T. Zhu, and K. Han, "Size effect on contact behavior in DEM simple shear tests," *Scientific Reports*, vol. 1, 2021.
- [11] M. Oda, I. Koishikawa, and T. Higuchi, "Experimental study of anisotropic shear strength of sand by plane strain test," *Soils and Foundations*, vol. 18, no. 1, pp. 25–38, 1978.
- [12] M. Oda and J. Konishi, "Microscopic deformation mechanism of granular material in simple shear," *Soils and Foundations*, vol. 14, no. 4, pp. 25–38, 1974.
- [13] M. Oda, S. Nematnasser, and M. M. Mehrabadi, "A statistical study of fabric in a random assembly of spherical granules," *International Journal for Numerical and Analytical Methods in Geomechanics*, vol. 6, 2010.
- [14] P. Guo, *Modelling Granular Materials with Respect to Stress-Dilatancy and Fabric: A Fundamental Approach*, Calgary, Canada, 2000.
- [15] Y. P. Yao and Y. X. Kong, "Study on strength and failure criterion of cross-anisotropic soil," *Journal of Hydraulic Engineering*, vol. 42, 2012.
- [16] H. Ouaifel and L. Rothenburg, "'Stress-force-fabric' relationship for assemblies of ellipsoids," *Mechanics of Materials*, vol. 33, no. 4, pp. 201–221, 2001.
- [17] Y. Liu, D. Zhang, X. Wang, P. Yu, and W. Hu, "Anisotropic Strength of Granular Material Considering Fabric Evolution," *Latin American Journal of Solids and Structures*, vol. 16, 2019.
- [18] A. L. Petalas, Y. F. Dafalias, A. G. Papadimitriou, and Sani-sand-F, "Sand constitutive model with evolving fabric anisotropy," *International Journal of Solids and Structures*, vol. 188–189, 2020.
- [19] M. Pouragha, M. Eghbalian, and R. Wan, "Micromechanical Correlation between Elasticity and Strength Characteristics of Anisotropic Rocks," *International Journal of Rock Mechanics and Mining Sciences*, vol. 125, 2020.
- [20] N. Hu, H. S. Yu, D. S. Yang, and P. Z. Zhuang, "Constitutive modelling of granular materials using a contact normal-based fabric tensor," *Acta Geotechnica*, vol. 15, no. 5, pp. 1125–1151, 2019.
- [21] X. F. Li, L. Kong, and M. S. Huang, "Property-dependent plastic potential theory for geomaterials," *Yantu Gongcheng Xuebao/Chinese Journal of Geotechnical Engineering*, vol. 35, pp. 1722–1729, 2013.
- [22] X. F. Li, M. S. Huang, and J. G. Qian, "Failure criterion of anisotropic sand with the method of macro-micro incorporation," *Chinese Journal of Rock Mechanics and Engineering*, vol. 29, pp. 1885–1892, 2010.

- [23] X. F. Li, Z. G. Ma, and F. C. Meng, "Quantitative description for sand void fabric with the principle of stereology," *Applied Sciences*, vol. 11, 2021.
- [24] M. R. Kuhn, "Micro-mechanics of fabric and failure in granular materials," *Mechanics of Materials*, vol. 42, 2010.
- [25] J. Shi and P. Guo, "Modelling fabric evolution of granular materials along proportional strain paths," *Springer Series in Geomechanics and Geoengineering*, vol. 46, pp. 373–379, 2017.
- [26] Y. Liu, D. Zhang, S. Wu, and Y. Pengqiang, "Investigation on the evolution of fabric under true triaxial conditions in granular materials," *International Journal of Geomechanics*, vol. 20, 2020.
- [27] J. Zheng, H. He, and Z. Li, "Explanations of Anisotropic Strength and Fabric Evolution in Granular Soils by DEM Simulations and Buckling Failure Theory," *Geomechanics and Geoengineering*, vol. 17, no. 2, 2020.
- [28] N. Hu, P. Zhuang, D. Yang, and H. Yu, "On the evolution law of a contact normal-based fabric tensor for granular materials," *Computers and Geotechnics*, vol. 132, 2021.
- [29] J. Y. Nie, Z. J. Cao, D. Q. Li, and Y. F. Cui, "3D DEM insights into the effect of particle overall regularity on macro and micro mechanical behaviours of dense sands," *Computers and Geotechnics*, vol. 132, 2021.
- [30] T. T. Ng, "Discrete element method simulations of the critical state of a granular material," *International Journal of Geomechanics*, vol. 9, 2009.
- [31] M. Oda, J. Konishi, and S. Nemat-Nasser, "Some experimentally based fundamental results on the mechanical behaviour of granular materials," *Géotechnique*, vol. 30, pp. 479–495, 1981.
- [32] M. Oda, S. Nemat-Nasser, and J. Konishi, "Stress-induced anisotropy in granular masses," *Soils and Foundations*, vol. 25, no. 3, pp. 85–97, 1985.
- [33] X. Gu, J. Hu, and M. Huang, "Anisotropy of elasticity and fabric of granular soils," *Granular Matter*, vol. 19, 2017.
- [34] A. Vijayan, Y. Gan, and R. K. Annabattula, "Evolution of fabric in spherical granular assemblies under the influence of various loading conditions through DEM," *Granular Matter*, vol. 22, 2020.
- [35] R. Wang, W. Cao, and J. M. Zhang, "Dependency of dilatancy ratio on fabric anisotropy in granular materials," *Journal of Engineering Mechanics*, vol. 145, 2019.
- [36] W. H. Zhou, X. Y. Jing, Z. Y. Yin, and X. Geng, "Effects of particle sphericity and initial fabric on the shearing behavior of soil-rough structural interface," *Acta Geotechnica*, vol. 14, no. 6, pp. 1699–1716, 2019.
- [37] H. Ochiai and P. V. Lade, "Three-dimensional behavior of sand with anisotropic fabric," *Journal of Geotechnical Engineering*, vol. 109, 1983.
- [38] D. S. Yang, *Microscopic Study of Granular Material Behaviours under General Stress Paths*, Nottingham, UK, 2014.
- [39] L. Cui, S. Bhattacharya, G. Nikitas, and A. Bhat, "Macro- and micro-mechanics of granular soil in asymmetric cyclic loadings encountered by offshore wind turbine foundations," *Granular Matter*, vol. 21, 2019.
- [40] O. Dorostkar and A. Mirghasemi, "Micro-mechanical study of stress path and initial conditions in granular materials using DEM," *Computational Particle Mechanics*, vol. 3, no. 1, pp. 15–27, 2016.
- [41] C. O'Sullivan, A. Wadee, K. J. Hanley, and D. Barreto, "Use of DEM and elastic stability analysis to explain the influence of the intermediate principal stress on shear strength," *Géotechnique*, vol. 63, 2013.
- [42] X. Huang, K. J. Hanley, C. O'Sullivan, C. Y. Kwok, and M. A. Wadee, "DEM analysis of the influence of the intermediate stress ratio on the critical-state behaviour of granular materials," *Granular Matter*, vol. 16, no. 5, pp. 641–655, 2014.
- [43] D. Phusing, K. Suzuki, and P. Srirat, "Evolutions of fabric and contact forces of granular materials under continuously varying b value using DEM," in *Proceedings of the International Conference on Discrete Element Methods Springer Proceedings in Physics*, pp. 81–90, Dalian, China, August 2016.
- [44] T. Foroutan and A. A. Mirghasemi, "CFD-DEM Model to Assess Stress-Induced Anisotropy in Undrained Granular Material," *Computers and Geotechnics*, vol. 119, 2020.
- [45] S. Zhao, N. Zhang, X. Zhou, and L. Zhang, "Particle shape effects on fabric of granular random packing," *Powder Technology*, vol. 310, pp. 175–186, 2017.
- [46] J. D. de Bono and G. R. McDowell, "Investigating the effects of particle shape on normal compression and overconsolidation using DEM," *Granular Matter*, vol. 18, pp. 1–10, 2016.
- [47] J. Liu, W. Zhou, G. Ma, S. Yang, and X. Chang, "Strong contacts, connectivity and fabric anisotropy in granular materials: a 3D perspective," *Powder Technology*, vol. 366, 2020.
- [48] R. Wang, Y. F. Dafalias, P. Fu, and J. M. Zhang, "Fabric evolution and dilatancy within anisotropic critical state theory guided and validated by DEM," *International Journal of Solids and Structures*, vol. 188–189, 2020.
- [49] M. Pouragha, N. P. Kruyt, and R. Wan, "Fabric Evolution in Granular Materials under Strain Probing," in *Proceedings of the Desiderata Geotechnica*, pp. 151–161, Vienna, Austria, August 2018.
- [50] A. Lashkari, M. Khodadadi, S. M. Binesh, and M. M. Rahman, "Instability of particulate assemblies under constant shear drained stress path: DEM approach," *International Journal of Geomechanics*, vol. 19, 2019.
- [51] B. Suhr and K. Six, "Simple particle shapes for DEM simulations of railway ballast: influence of shape descriptors on packing behavior," *Granular Matter*, vol. 22, 2020.
- [52] O. Dorostkar and A. A. Mirghasemi, "On the micromechanics of true triaxial test, insights from 3D DEM study," *Iranian Journal of Science and Technology, Transactions of Civil Engineering*, vol. 42, no. 3, pp. 259–273, 2018.
- [53] R. Yuan, H. S. Yu, D. S. Yang, and N. Hu, "On a fabric evolution law incorporating the effects of b -value," *Computers and Geotechnics*, vol. 105, pp. 142–154, 2019.
- [54] M. M. Sazzad and K. Suzuki, "Density dependent macro-micro behavior of granular materials in general triaxial loading for varying intermediate principal stress using DEM," *Granular Matter*, vol. 15, no. 5, pp. 583–593, 2013.
- [55] J. He and M. J. Jiang, "Macro-micro mechanical property of pore-filling type methane hydrate-bearing sediment in true triaxial tests based on distinct element analysis," *Rock and Soil Mechanics*, vol. 37, pp. 3026–3034, 2016.
- [56] Y. Tobita and E. Yanagisawa, "Contact tensor in constitutive model for granular materials," *Studies in Applied Mechanics*, vol. 20, 1988.
- [57] X. F. Li, Q. Wang, J. F. Liu, W. Wu, and F. C. Meng, "Quantitative description of microscopic fabric based on sand particle shapes," *China Journal of Highway and Transport*, vol. 29, 2016.
- [58] M. Oda, "Fabric tensor and its geometrical meaning," in *Soils and Foundations*, vol. 22, pp. 27–35, A. A. Balkema, 1999.
- [59] J. Yang and D. X. Luo, "Exploring the relationship between critical state and particle shape for granular materials,"

- Journal of the Mechanics and Physics of Solids*, vol. 84, pp. 196–213, 2015.
- [60] S. M. Binesh, E. Eslami-Feizabad, and R. Rahmani, “Discrete element modeling of drained triaxial test: flexible and rigid lateral boundaries,” *International Journal of Civil Engineering*, vol. 16, no. 10, pp. 1463–1474, 2018.
- [61] T. Qu, Y. Feng, Y. Wang, and M. Wang, “Discreteelement modelling of flexible membrane boundaries for triaxial tests,” *Computers and Geotechnics*, vol. 115, 2019.
- [62] A. X. Jerves, R. Kawamoto, and J. Andrade, “Effects of grain morphology on critical state: a computational analysis,” *Acta Geotechnica*, vol. 11, no. 3, pp. 493–503, 2015.
- [63] A. Lashkari, S. R. Falsafizadeh, P. T. Shourijeh, and M. J. Alipour, “Instability of loose sand in constant volume direct simple shear tests in relation to particle shape,” *Acta Geotechnica*, vol. 15, no. 9, pp. 2507–2527, 2020.
- [64] A. Tsomokos and V. N. Georgiannou, “Effect of grain shape and angularity on the undrained response of fine sands,” *Canadian Geotechnical Journal*, vol. 47, no. 5, pp. 539–551, 2010.
- [65] B. Sukumaran and A. K. Ashmawy, “Quantitative characterisation of the geometry of discret particles,” *Géotechnique*, vol. 51, no. 7, pp. 619–627, 2001.
- [66] S. Liu and H. Matsuoka, “Microscopic interpretation on a stress-dilatancy relationship of granular materials,” *Soils and Foundations*, vol. 43, no. 3, pp. 73–84, 2003.
- [67] A. Casagrande and N. Carillo, *Shear Failure of Anisotropic Materials*, pp. 122–135, *Contribut Soil Mech (BSCE)*, 1944, https://www.researchgate.net/publication/285811278_Shear_failure_of_anisotropic_materials/citations.
- [68] M. Oda and H. Nakayama, “Yield function for soil with anisotropic fabric,” *Journal of Engineering Mechanics*, vol. 115, no. 1, pp. 89–104, 1989.
- [69] N. Hu, H. Yu, D. Yang, and P. Zhuang, “Constitutive modelling of granular materials using a contact normal-based fabric tensor,” *Acta Geotechnica*, vol. 15, pp. 1–27, 2020.
- [70] A. Lashkari and N. Norouzi, “An Anisotropic Critical State Plasticity Model with Stress Ratio-dependent Fabric Tensor,” *Iranian Journal of Science and Technology - Transactions of Civil Engineering*, vol. 45, pp. 2577–2594, 2020.
- [71] P. Guo and X. Su, “Shear strength, interparticle locking, and dilatancy of granular materials,” *Canadian Geotechnical Journal*, vol. 44, no. 5, pp. 579–591, 2007.

Review Article

Remote Sensing Image Classification: A Comprehensive Review and Applications

Maryam Mehmood,^{1,2} Ahsan Shahzad,² Bushra Zafar ,³ Amsa Shabbir,¹ and Nouman Ali ¹

¹Department of Software Engineering, Mirpur University of Science and Technology (MUST), Mirpur AJK 10250, Pakistan

²Department of Computer and Software Engineering, National University of Sciences and Technology, Islamabad, Pakistan

³Department of Computer Science, Government College University, Faisalabad 38000, Pakistan

Correspondence should be addressed to Nouman Ali; nouman.ali@live.com

Received 31 March 2022; Accepted 20 June 2022; Published 2 August 2022

Academic Editor: Afaq Ahmad

Copyright © 2022 Maryam Mehmood et al. This is an open access article distributed under the Creative Commons Attribution License, which permits unrestricted use, distribution, and reproduction in any medium, provided the original work is properly cited.

Remote sensing is mainly used to investigate sites of dams, bridges, and pipelines to locate construction materials and provide detailed geographic information. In remote sensing image analysis, the images captured through satellite and drones are used to observe surface of the Earth. The main aim of any image classification-based system is to assign semantic labels to captured images, and consequently, using these labels, images can be arranged in a semantic order. The semantic arrangement of images is used in various domains of digital image processing and computer vision such as remote sensing, image retrieval, object recognition, image annotation, scene analysis, content-based image analysis, and video analysis. The earlier approaches for remote sensing image analysis are based on low-level and mid-level feature extraction and representation. These techniques have shown good performance by using different feature combinations and machine learning approaches. These earlier approaches have used small-scale image dataset. The recent trends for remote sensing image analysis are shifted to the use of deep learning model. Various hybrid approaches of deep learning have shown much better results than the use of a single deep learning model. In this review article, a detailed overview of the past trends is presented, based on low-level and mid-level feature representation using traditional machine learning concepts. A summary of publicly available image benchmarks for remote sensing image analysis is also presented. A detailed summary is presented at the end of each section. An overview regarding the current trends of deep learning models is presented along with a detailed comparison of various hybrid approaches based on recent trends. The performance evaluation metrics are also discussed. This review article provides a detailed knowledge related to the existing trends in remote sensing image classification and possible future research directions.

1. Introduction

Deep learning and computer vision are used in various applications such as image classification, object detection in industrial production, medical image analysis, action recognition, and remote sensing [1–4]. Satellite images are considered the main source of acquiring geographic information [5], and there are many applications of satellite image analysis in the field of civil engineering such as design, construction, urban planning, and water resource management. The data obtained from satellite sources are huge

and are growing exponentially; to handle these large data, there is a need to have efficient techniques for data extraction purpose. Through image classification, these large number of satellite images can be arranged in semantic orders. The satellite image classification is a multilevel process that starts from extracting features from images to classifying them into categories [6]. Image classification is a step-wise process that starts with designing scheme for classification of desired images. After that, the images are preprocessed which include image clustering, image enhancement, scaling, and so on. At third step, the desired areas of those images are

selected and initial clusters are generated. After that, the algorithm is applied on the images to get the desired classification, and corrective actions are made after that algorithm phase which is also called postprocessing. The final phase is to assess the accuracy of this classification, as shown in Figure 1.

Recent research is focused on the use of mid-level features and deep learning models to build robust decision support systems for smart vehicles, Internet of Things (IoT), and remote sensing images [7–9]. To get the geographical data on large scales, remote sensing plays a significant role, and efficient land use could be achieved through aerial images of Earth [10]. Some are supervised techniques while some of them are unsupervised. Similarly, while keeping in focus the parameters, there are parametric and non-parametric approaches; another type is fuzzy classification [11]; besides this, classification can also be performed on prepixels or subpixels. The latest research in remote image classification is towards hybrid approaches, where two or more techniques are combined to get better classification [3, 12, 13]. The most recent research is focused towards scene-based classification. The whole remote sensing image classification process is divided into three kinds of basic division: supervised learning, unsupervised learning, and deep learning approaches. Supervised learning techniques are further divided into distributed and statistical learning [14–16]. There are many types of distributed learning like logistic regression, decision trees, support vector machine (SVM), ensemble methods, and so on, whereas statistical learning techniques are further divided into parametric and non-parametric approaches. Similarly, different types of unsupervised learning techniques like K-means clustering, spectral clustering, fuzzy C-means, and reinforcement learning are discussed in detail. Moving towards the third division, that is, deep learning approaches, they are further divided into three categories: generative methods, hybrid methods, and discriminative methods. Deep belief network (DBN), network autoencoder, and deep Boltzmann machine (DBM) are discussed in generative methods, whereas deep neural network (DNN) and grey wolf optimization (GWO) are discussed in hybrid methods. In discriminative methods, transfer learning, convolutional neural network (CNN), AlexNet, VGG, GoogLeNet, MobileNet, ResNet, artificial neural network (ANN), and so on are discussed, as shown in Figure 2.

There are basically three types of remote image classifications that are mainly pixel-based classification, object-based classification, and scene-based classification, and the recent research is focused towards scene-based classification [17, 18]. Figure 3 shows that due to the improved research, spatial resolution of images is increased drastically [19]. There is no need to classify remote images on the basis of pixels, and research trend changed towards the object-based classification of images. By objects of remotely sensed images, we mean semantics or scene units [20]. During the last two decades, processing visual features of an image was a time consuming and computationally expensive task, which

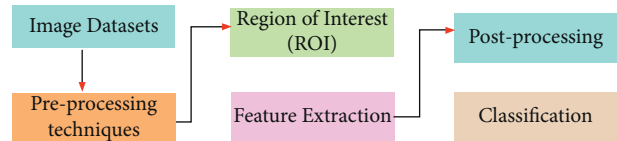


FIGURE 1: Remote sensing image classification process.

required lots of effort and resources. According to the literature in recent years, scale invariant feature transform (SIFT), textual descriptors (TD), color histogram (CH), histogram of oriented gradients (HOG), and global image descriptor (GIST) [21] were proposed by human engineers. After a while, some improvements were made and improved Fisher kernel, spatial pyramid matching (SPM), and bag of visual words (BoVW) were introduced [22]. These encoding techniques were relatively more efficient than the existing techniques [23].

In simple words, we can differentiate between supervised and unsupervised learning as follows: supervised learning algorithms are trained using labeled data, whereas unsupervised learning algorithms are trained using unlabeled data. In case of unsupervised learning, principal component analysis (PCA), sparse coding, and K-means clustering were introduced later on. The benefit of these techniques is that they are able to automatically learn the features. But these unsupervised learning techniques were not doing justice when there are larger datasets [24]. Due to advancement in deep learning techniques and parallel computing, these remote images can be easily classified by initializing weights in training layers so that the prediction of scene could be more accurate in later deep learning layers [25]. There are many deep learning models that exist in literature like AlexNet, GoogLeNet, VGG, and ResNet [26]. AlexNet was proposed in 2012, and it has 60M parameters and is 8 layers deep [27]. GoogLeNet was proposed in 2015, and it has 4M parameters and has 22 layers. It also comes under the category of spatial exploitation [28]. After that, VGGNet was proposed in 2015, and it has 138M parameters and is 16 and 19 layers deeper [26]; it has two types: VGG16 and VGG19. Later ResNet was proposed, and it has various variants like ResNet18, ResNet34, ResNet50, ResNet101, ResNet110, ResNet152, ResNet164, and ResNet1202, and it has 25.6M parameters [29]. The above-mentioned models come under the category of spatial exploitation. Comprehensive reviews relevant to remote sensing image classifications are published in recent years. In [30], we can see a detailed review of multimodel remote sensing image classification. Also, in another article before 2016, all the remote sensing classification techniques were discussed in detail in [31]. In 2017, a detailed review about process of remote sensing image classification was discussed in [32]. The details about the resources for remote sensing research are enlisted in this article [32]. In 2017, a detailed comparison of existing deep learning techniques for hyperspectral classification was given in [33]. In 2017, a review about support vector machine (SVM) techniques relevant to remote sensing was

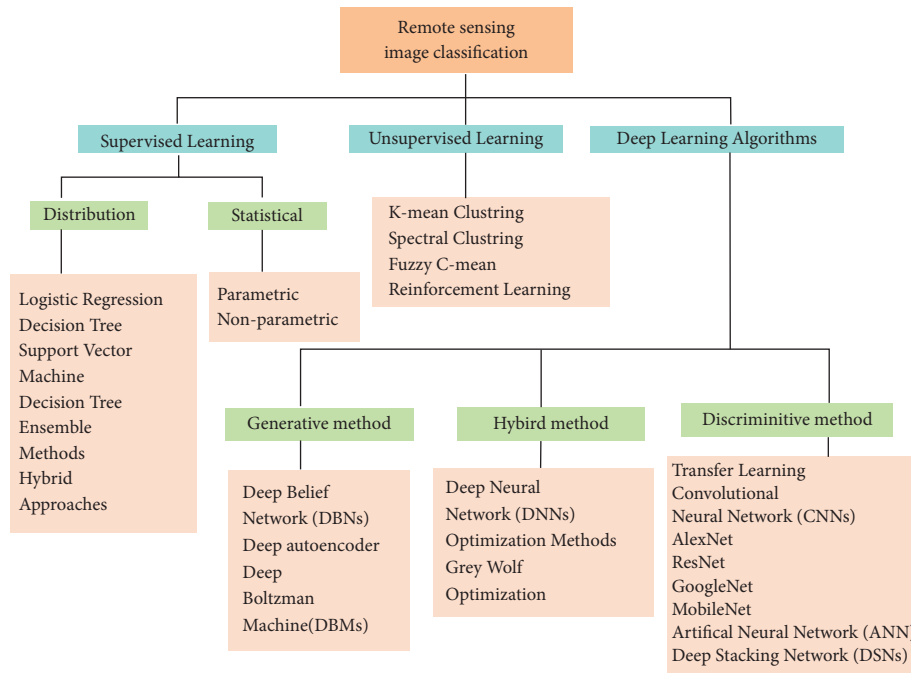


FIGURE 2: Supervised and unsupervised learning techniques.

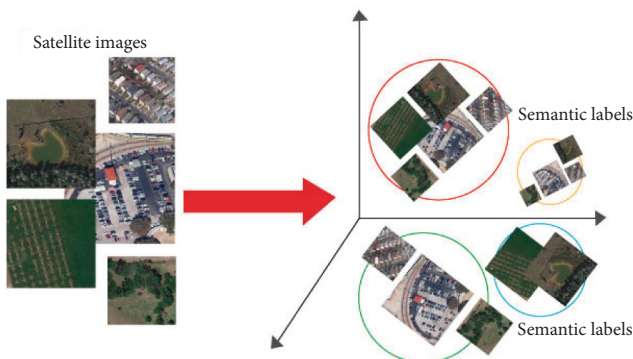


FIGURE 3: Introduction to remote sensing image classification.

discussed in [34]. In [35], AID dataset was proposed, and it also includes remote sensing image classification surveys before 2017. A review of multiple remote sensing techniques and also NWPU-RESISC45 dataset was proposed in [36]. In recent years, comprehensive reviews relevant to hyper-spectral and spatial-spectral images analysis are published [20, 37]. A detailed summary about deep learning in remote sensing applications, current challenges relevant to deep learning methods, benchmarks, and possible future research directions are referred to the following review articles [38–40].

The article is organized as follows: there is a basic introduction about remote sensing image classification in the start. Section 2 is about machine learning. Section 3 contains the detailed description of CNN models and their applications. Section 4 deals with existing deep learning techniques. Section 5 is about the datasets commonly used for

remote sensing image classification which are discussed in detail. Section 6 deals with unsupervised learning techniques. Section 7 is about optimization techniques. Sections 8, 9, and 10 are about feature fusion techniques. Section 11 deals with hybrid approaches. Section 12 is about performance evaluation criterion for classification. In the last section, a conclusion of the proposed research is presented.

2. Machine Learning

Machine learning (ML) is the field of computer science which incorporates both supervised and unsupervised learning techniques [41–43]. It covers both regression and classification problems [44]. In machine learning, a detailed dataset is constructed that covers maximum of system parameters. ML is useful in the scenarios where theoretical knowledge is not sufficient to predict some information out of it [45, 46]. It has a huge number of applications in many areas like land use and cover concerns [47] disaster management, atmosphere changes, and many more [48]. ML is the subdivision of artificial intelligence (AI) [49]. ML basically designs an algorithm to be able to learn from the data to predict something out of it. There are many algorithms present in the field of machine learning that are doing exceptional job like support vector machine, Bayesian network, decision trees, ensemble methods, random forest, neural networks, genetic programming, and many more. ML has a huge impact on remote sensing and geosciences. It automatically extracts features from the data using statistical techniques [50, 51]. At the start, the classification of remote sensing images was considered to be “shallow structures.” To perform remote sensing classification, there exist different

techniques like decision trees, SVM, artificial neural network, bag of visual words, and many more [52–54]. Another important application of ML techniques is to detect the change from the normal scenarios. Images are captured through satellites or drones and then ML techniques are applied to predict the behavior or change [55]. SVM and GA are combined to detect the change. Both supervised learning approaches and unsupervised learning techniques are combined to get the association of adjacent pixels of images, while using SVM, radial basis kernel is used and its parameters like C and Ω are optimized using genetic algorithm (GA); this optimization process increased the efficiency of the process. The authors have performed experimentation while using Mexico dataset and Sardinia image datasets. The results are validated with existing results and the proposed approach outperforms when compared to the existing results [56]. In early years of ML, the accuracy of only high spectral images was high [57]. To overcome this issue, a new 3-D approach was used in combination with spatial and spectral images. The experimentation was performed on Pavia University (PU), Pavia Center (PC), and Kennedy Space Center (KSC) datasets, and the results show that the proposed methods achieve better accuracy with low computational cost [58]. It has many applications in different fields of life like speech recognition systems, search engines, and other AI-based applications like robotics [59]. There are many ML techniques available in literature like K-means clustering and PCA for classification tasks, and to perform regression, there are techniques like SVM, decision trees, ANN, ensemble methods, random forest, and so on [60, 61]. Remote sensing image classification can be performed using existing CNN methods, but they require high computational power and a big labeled dataset for better performance. There are freely available datasets. We can use pretrained networks to get better accuracy. There exist strategies to avoid overfitting and dropouts which also play an important role. The training time of CNN models is quite long, but GPUs help us to solve this issue [62]. Remote images captured from satellite images have a huge importance, but there are some issues in the clarity of images when weather conditions are not so clear which affect the feature selection part of ML process and thus performance degrades [63]. The article described below fills this gap by using a specially designed toolbox. In the first step, gaps between spatial relationships and pixels are filled, while remaining gaps of temporal dynamics of each pixel are filled in the second phase. The experimentation of above algorithm was performed on two datasets Sentinel-3 SLSTR and Terra MODIS. Data were collected in different seasonal conditions. Also, the experimentation was performed on GNU GPL3 which is a public repository [64].

3. Convolutional Neural Network

Convolutional neural networks are useful in many multimedia applications where we need to classify images without human interference. In this article, four different deep learning models: AlexNet, VGG19, GoogLeNet, and ResNet50, were used for feature extraction. The

experimentations were performed on different datasets: SAT4, SAT6, and UCMD, where images for the datasets SAT4 and SAT6 were extracted from NAIP dataset which has around 330000 scene images of all over US. SAT4 and SAT6 have 4 and 6 classes, respectively, and labels are trees, grassland, barren land, building, road, water, and so on, whereas for UCMD dataset, images were extracted from a large dataset named USGS. It has 20 classes in it. Training and testing ratio for SAT datasets is selected as 80:20, respectively, whereas for UCMD, it is 70:30 [65, 66]. Figure 4 shows the basic process of image classification for CNN.

ResNet50 gives better accuracy on all the three above-mentioned datasets. Accuracy on UCM is 98% and that on SAT4 is 95.8%, whereas that on SAT6 is 94.1%. Satellite image classification is a challenging task due to its variability. Due to this issue, existing approaches are not feasible for object detection in satellite images. In this article, a new model DeepSat V2 is proposed which is basically an augmented version of CNN. The first phase is feature extraction phase where 50 features were extracted and then statistical approaches were used for feature ranking to extract the useful features. It has 2 convolutional layers with RELU layer attached. After convolutional layers, there is a max-pooling layer with dropout layer at the end. After that, feature concatenation layer is present followed by fully connected layers. Last layer is softmax layer based on cross entropy loss function. The optimizer used in this model is Adadelta. All the experimentation was performed on SAT4 and SAT6 datasets. This proposed model has achieved accuracy of 99.9% and 99.84% on SAT4 and SAT6, respectively [67].

4. Deep Learning-Based Methods and Approaches

Satellite images have high importance in many fields of life. This article is about the available datasets on remote sensing and the techniques used to classify satellite images. The existing image classification techniques can be divided into four categories: manual feature extraction, unsupervised feature extraction, supervised feature extraction, and object-based classification, as shown in Figure 5.

Dataset used in this article for classification is UCM land use which has 21 classes and 2100 images. Experimentation was performed using AlexNet. Images used for training are about 10%, and after eight iterations, accuracy reached at 94%. By comparing GoogLeNet and CaffeNet, GoogLeNet gives better accuracy, that is, 97%, on UCM dataset. But AlexNet is almost 4 times faster. Deep learning methods perform better in image classification as compared to other feature extraction techniques [68]. The article is about useful methods for feature extraction using deep learning techniques. AlexNet, VGG19, GoogLeNet, and ResNet50 were used here, whereas experimentation is performed on 3 different datasets: SAT4, SAT6, and UC Merced. The accuracy of UCM dataset on multiple deep learning models is summarized in Table 1.

Performance of the proposed ResNet50 on SAT6 is better as compared to previous models, whereas accuracy on SAT4 is degraded. Classification accuracy of the proposed

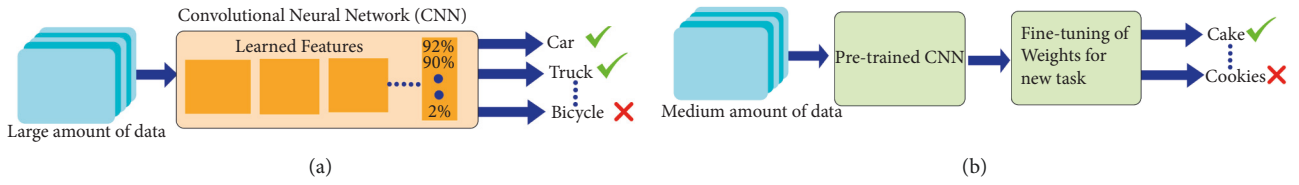


FIGURE 4: Convolutional neural network.

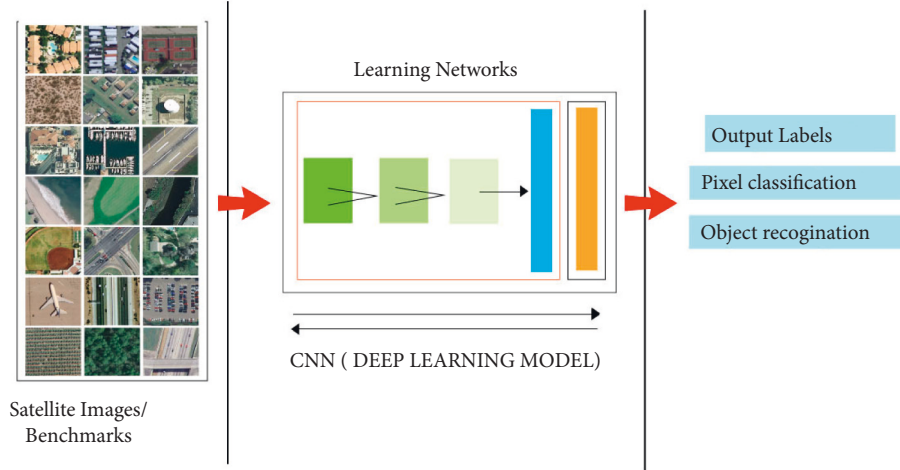


FIGURE 5: Image classification through deep learning.

TABLE 1: Classification accuracy of UCM on different CNN models.

Algorithm	Year	Publication	Accuracy (%)
MCNN [69]	2018	IEEE trans	99.76
ARCNet-VGG16 [19]	2018	IEEE trans	99.12
FACNN [70]	2019	IEEE trans	99.05
SF-CNN [71]	2019	IEEE trans	99.05
CNN-CapsNet [22]	2019	Remote sensing	99.05
D-CNN [72]	2018	IEEE trans	98.93
ADSSM [73]	2018	IEEE trans	98.81
RSFJR [71]	2019	IEEE trans	98.57
GBN [74]	2019	IEEE trans	98.57
MSCP [19]	2018	IEEE trans	98.36
ADFF [75]	2019	IEEE trans	97.53
VGG-VD-16 [76]	2017	IEEE trans	95.21
CaffeNet [76]	2017	IEEE trans	95.02
GBRCN [77]	2015	IEEE trans	94.53
GoogLeNet [76]	2017	IEEE trans	94.31
AlexNet [78]	2021	Journal of Geosciences	94.20
Feature RCGSVM [22]	2019	PLOS ONE	93.81
Inception-V3 [78] [2]	2021	Journal of Geosciences	91.10
LPCNN [79]	2016	IEEE trans	89.90

ResNet50 on SAT4 is 95.8%, that on SAT6 is 94.1%, and that on UCM is 98% [80]. In this article, a new CNN model known as deep convolutional neural network (DCNN) is proposed which works in twofold. In the first phase, multiple filters were introduced to minimize variance, whereas in the 2nd phase, best suited hyperparameters were selected from the pool. Based on these found parameters, a new convolutional neural network (DCNN) model is built and experimentation is performed. The results are validated using

DeepSat model, whereas datasets used are SAT4 and SAT6. Table 2 summarizes the accuracy of RSSCN dataset on different CNN models. Classification accuracy of SAT4 using convolutional neural network (DCNN) is 98.408%, whereas that of SAT6 using convolutional neural network (DCNN) is 96.037% which is better than the model used for validation [83]. In satellite image classification, the process of scale selection is very important task. The remote image datasets are in larger number, and it is very important to

TABLE 2: Classification accuracy of RSSCN on different CNN models.

Algorithm	Year	Publication	Accuracy (%)
CaffeNet [81]	2019	Journal of Geovisualization and Spatial Analysis	88.25
VGG-VD-16 [82]	2018	Applied Sciences	87.18
Inception-V3 [81]	2019	Journal of Geovisualization and Spatial Analysis	87
AlexNet [78]	2021	Journal of Geosciences	85.25
GoogLeNet [82]	2018	IEEE	84.84
POVH [22]	2019	PLOS ONE	84.07
RGSIR [22]	2019	PLOS ONE	81.44

select the relevant techniques for the selection process. In [84], an enhanced technique of CNN model is used and experimentation is performed on WHU-RS, UC Merced, and Brazilian coffee scene datasets. Here classification accuracies of all three datasets are presented. For UCM dataset, the accuracy is better at stage 2, whereas for WHU-RS datasets, the accuracies are measured after stage 1, stage 2, and stage 4 of image scaling. After scales 1 and 2, the accuracy is improved, but after scales 3 and 4, the improvement in accuracy is very small. Land cover land use has a great link between human and nature, and many research studies are available on one-class extraction, but there is a need to focus on multiclass classification. Here in this article, to overcome the issue of low-resolution loss, a new model HR-net is introduced. Comparison was performed on DeepLab and U-Net. The proposed model performs better, test accuracy is 95.7%, mean I/U value is 88.01%, and kappa value is 94.55% [85]. There are datasets available on remote sensing and also techniques used to classify satellite images. The existing image classification techniques can be divided into four categories: manual feature extraction, unsupervised feature extraction, supervised feature extraction, and object-based classification. Dataset used in this article for classification is UCM land use which has 21 classes and 2100 images. Experimentation was performed using AlexNet. 10% images were used for training, and after eight iterations, the accuracy reached at 94%. By comparing GoogLeNet and CaffeNet, GoogLeNet gives better accuracy, that is, 97%, on UCM dataset, but AlexNet is almost 4 times faster. Deep learning methods perform better in image classification as compared to other feature extraction techniques [86]. Xia et al. [76] used google net algorithm and reported a classification accuracy of 94.31% while using UCM image benchmark. Zhang et al. [77] performed scene classification using gradient boosting random convolutional network framework and reported classification accuracy as 94.53% while using UCM image benchmark. Zhong et al. [79] used large patch convolutional neural networks and reported a classification accuracy value as 89.90% for UCM image benchmark. The classification accuracies of AID dataset on different CNN models are summarized in Table 3.

While using the same dataset, the experimentation was performed on CaffeNet, and the accuracy noted in this experimentation is 95.31%. In the third run using same dataset with a different algorithm, i.e., VGG-VD-16, the classification accuracy is 95.21% for UCM dataset. In 2nd run for AID dataset, the experimentation was performed using GoogLeNet and Inception-V3 algorithm, and the accuracies mentioned in

the article are 86.39% and 93%, respectively [76]. Experimentation was performed using ARCNet-VGG16 in scene classification with recurrent attention of VHR remote sensing images reaching the accuracy up to 99.12%. The same experimentation was performed on AID dataset and the accuracy achieved is 93.10% using UCM dataset [19]. In [19], it is stated that they have performed the experimentation using minimum sum coloring problem (MSCP) algorithm and the classification accuracy achieved is 98.36% for UCM dataset. Again the experimentation was performed on AID dataset using three algorithms MSCP, DCNNS, and HW-CNN, whereas the accuracies are 94.42%, 96.89%, and 96.98%, respectively. Zhu et al. [69] reported a value of classification accuracy as 99.76% while using UCM image benchmark. Lu et al. [73] used feature aggregation convolutional neural networks and reported the classification accuracy as 98.81% while using UCM image benchmark. Experimentation performed using feature aggregation convolutional neural network (FACNN) algorithm has achieved accuracy of 99.05%, and the dataset used for experimentation is UCM [70]. Spatial frequency (SF-CNN) has reached the accuracy of 99.05% using UCM dataset. The same algorithm was used for AID dataset and accuracy achieved was 96.66%, whereas using feature aggregation convolutional neural network (FACNN) algorithm on AID dataset, the classification accuracy mentioned in the same article was 95.45% [71].

In [71], it is stated that using robust space-frequency joint representation (RSFJR) algorithm, they have achieved classification accuracy of 98.57% using UCM dataset. In another research, it is stated that they have achieved classification accuracy of 98.57% using GBN algorithm for UCM dataset [74]. ADFE algorithm gave an accuracy of 97.53% in another research using UCM dataset. The same experimentation was performed on AID dataset, and the accuracy achieved is 94.75% [75]. Another research achieved the accuracy of 99.05% using CNN-Caps Net algorithm using UCM dataset. In another article, they achieved accuracy of 93.81% using feature RCGSVM for UCM dataset [22]. AlexNet and inception algorithms gave an accuracy of 94.2% and 911.1%, respectively, using the UCM dataset. Again using AID dataset, the experimentation was performed on VGG-VD-16, and the accuracy achieved is 89.64% [78]. In the article, the author performed experimentation using SCCOV, and the accuracy achieved is 96.10%, and the dataset used for experimentation is AID [89]. Using AID dataset, accuracy achieved is 96.81%, and the algorithm used for experimentation is RSFJR [71]. Using ResNet, another research claimed that they have achieved accuracy of 89.1%

TABLE 3: Classification accuracy of AID on different CNN models.

Algorithm	Year	Publication	Accuracy (%)
CNNS-WD [72]	2019	IEEE trans	97.24
HW-CNN [87]	2018	IEEE trans	96.98
DCNNS [87]	2018	IEEE trans	96.89
RSFJR [71]	2019	IEEE trans	96.81
SF-CNN [70]	2019	IEEE trans	96.66
CNN-CAPSNET [88]	2019	Remote sensing	96.32
SCCOV [89]	2019	IEEE trans	96.10
GBN [70]	2019	IEEE trans	95.48
FACNN [70]	2019	IEEE trans	95.45
ADFF [74]	2019	IEEE trans	94.75
MSCP [87]	2018	IEEE trans	94.42
ARCNet-VGG16 [19]	2017	IEEE trans	93.10
Inception-V3 [76]	2017	IEEE trans	93
MCNN [16]	2018	IEEE trans	91.80
VGG-VD-16 [78]	2021	Journal of Geosciences	89.64
CaffeNet [81]	2019	Journal of Geovisualization and Spatial Analysis	89.10
GoogLeNet [76]	2017	IEEE trans	86.39

TABLE 4: Classification accuracy of SIRI-WHU on different CNN models.

Algorithm	Year	Publication	Accuracy (%)
ResNet50 [22]	2019	PLOS ONE	94.03
AlexNet [81]	2019	Journal of Geovisualization and Spatial Analysis	90.20
GoogLeNet [78]	2021	Journal of Geosciences	89.30
Inception-V3 [78]	2021	Journal of Geosciences	89
VGGNet [78]	2021	Journal of Geosciences	86.60
POVH [81]	2019	Journal of Geovisualization and Spatial Analysis	80.14

using AID dataset. From the literature, we have extracted accuracies of different datasets on different CNN models. In Table 4, the datasets with their respective accuracies are mentioned. Similarly, the classification accuracies of SIRI-WHU dataset on different CNN models are also summarized in Table 4.

5. Datasets

The details about different remote sensing datasets are described below:

5.1. SAT4 and SAT6. National Agriculture Imagery Program (NAIP) dataset was used to extract the images to the dataset. SAT4 consists of total of 500,000 image patches while SAT6 consists of 405,000 image patches, as shown in Figure 6.

5.2. Brazilian Coffee Scenes. Dataset is taken from four countries with the size of 64×64 pixels. There are 600 images in 4 different kinds of dataset while the fifth kind has 476 images. Table below summarizes details regarding the total number of classes, images per class, number of images per class and total number of images in the benchmark, image spatial resolution, and dimensions. Figure 7 summarizes the details about coffee dataset images and other dimensions.

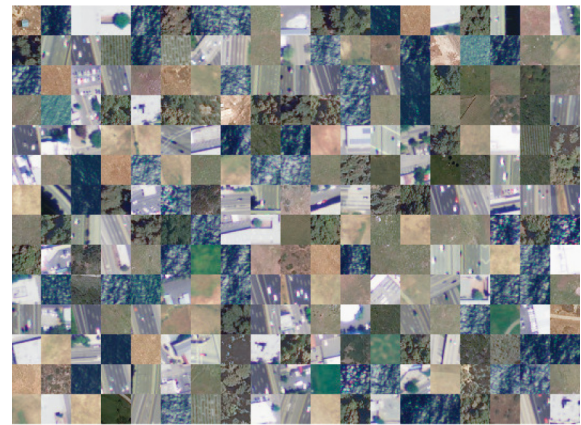


FIGURE 6: Picture gallery taken from all classes of SAT dataset.

5.3. RSSCN. The remote sensing image classification dataset comprises images gathered from Google Earth Engine and covers widespread areas. RSSCN consists of 7 classes of quintessential scene images having a size of 400×400 pixels. Further description about this image benchmark is discussed in the dataset description table. Figure 8 shows the picture gallery of all the classes of RSSCN dataset.

5.4. SIRI-WHU. The description such as image size, total number of images, images per class, and date of creation is referred to the following research article [22]. The images



FIGURE 7: Picture gallery taken from all classes of coffee dataset.

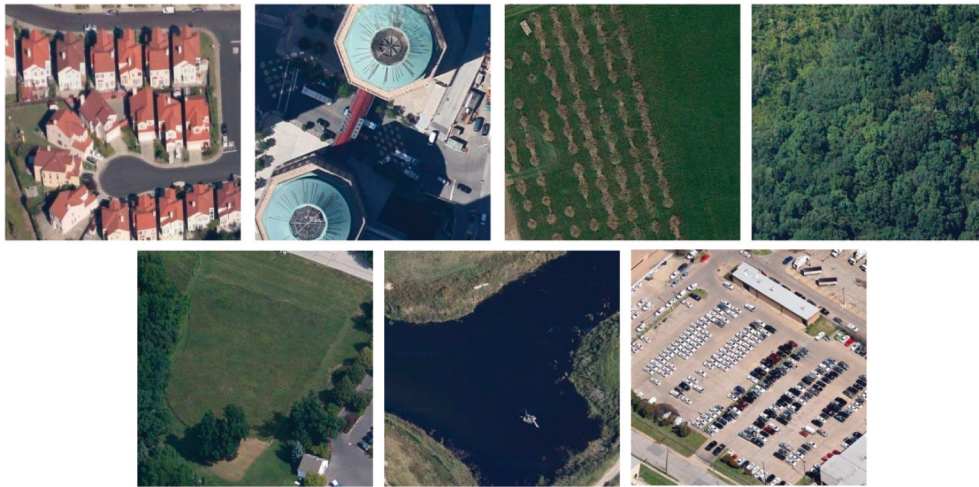


FIGURE 8: Picture gallery taken from all classes of RSSCN dataset.

have a spatial resolution of 2 m with image size of 200×200 pixels. Figure 9 shows randomly selected images taken from each class of SIRI-WHU dataset.

5.5. UC Merced Land Use. The description such as image size, total number of images, images per class, and date of creation is referred to [65]. There are a total of 21 distinctive scene categories with 100 images per class and dimensions of 256×256 pixels, as shown in dataset description table. Figure 10 shows the indiscriminately selected examples of each category included in the dataset (Table 5).

5.6. AID Dataset. AID dataset has 10000 images with 30 different classes. Figure 11 shows the photo gallery of AID dataset.

5.7. DIOR Dataset. The DIOR dataset includes 23,463 images and 192,472 object. Figure 12 shows the photo gallery of

DIOR dataset. Table 5 shows some of the existing datasets with image quantity and other descriptions.

6. Unsupervised Learning Approaches

Due to the advancement of space and satellite technologies, remote sensing has reached a new height [90]. Due to these high-resolution satellites, it has become easier to perform land use land cover surveys, to detect change, to recognize objects, and so on [91]. It has become easier to automatically interpret the image acquaintances due to the advancement in image classification techniques. Using these satellite data efficiently and in effective manner is still challenging. CNNs plays an important role in this image classification process. The article discussed below presents a framework called unsupervised restricted de-convolution neural network (URDNN). The main idea behind this framework is to get unsupervised restricted de-convolution using neural networks. It learns the pixel to pixel and end to end classification and then passes it to CNN model for assigning labels. Due to this, the issue of over and underfitting has been



FIGURE 9: Picture gallery taken from all classes of SIRI-WHU dataset.

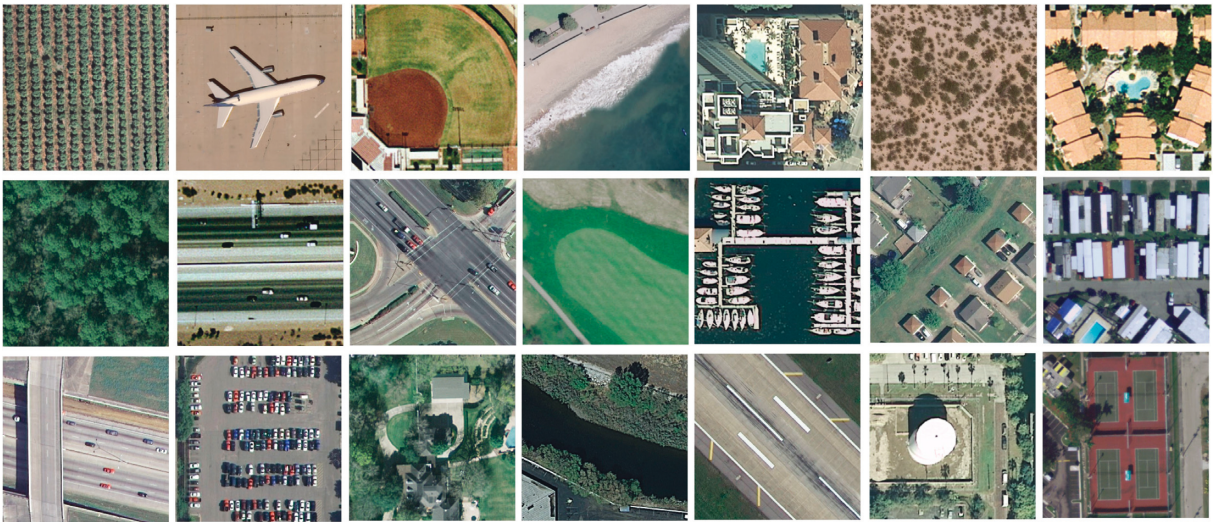


FIGURE 10: Picture gallery taken from all classes of UCM dataset.

TABLE 5: Dataset description.

Dataset	Total number of images	Total number of classes	Image size	Year
UCM [1]	2100	21	256×256	2010
SIRI-WHU	2400	12	200×200	2016
RSSCN7	2800	7	400×400	2015
Brazilian coffee scene	2876	2	64×64	2015
SAT4/SAT6	500000/405000	4 and 6	28×28	2015
AID	10000	30	600×600	2017
NWPU-RESISC45	31500	45	256×256	2017
OPTIMAL	1860	31	256×256	2018
WHU-RS19	1005	19	600×600	2012
NWPU VHR-10 dataset	800	10	VHR	2014
DIOR and DIOR-R datasets	23,463	20	VHR	2020
IKONOS	1000	10	64×64	2008
In-house dataset	606	6	4500×6000	2011
SPOT image dataset	912	3	512×512	2013
ORNL dataset	690	5	512×512	2014

reduced which occurs due to the large number of labeled data. The experimentation was performed on two datasets Geoeye and Quick-bird sensors [92]. The results are better than the previous models. The accuracy achieved is 97% and

98.9%, respectively [92]. Remote sensing image classification using unsupervised deep learning techniques is introduced here. In the first step, CNN extracts features using unsupervised techniques. After that, parameters of the network



FIGURE 11: Picture gallery taken from all classes of AID dataset.

are trained, which are then passed to the classifier. The cost of computation decreased due to unsupervised learning. SVM classifier was used in the process while spatio-spectral information was efficiently extracted with this technique. Adding new layers in the network improves efficiency, but the problem of overfitting is introduced [93]. While discussing unsupervised remote sensing image classification, the concepts of scale invariant feature transform and histogram-oriented gradient are very important [94]. Image is converted into feature vector by encoding; as compared to hand-engineered image representation, unsupervised learning techniques have achieved a new height [95]. We can get image features right from the start of raw pixels of an image. Gabor filters can be applied to those image patches to get the image features out of those pixels. Bags of word (BOW) is another concept of image classification and image retrieval [96]. To get the best results in terms of accuracy, we need to add SVM with non-linear kernel. While keeping

remote sensing in mind, both color feature and intensity are important while classification. But most of the existing algorithms cannot handle this at a time. The article discussed below discussed this issue. The authors have considered the quaternion of color features and then proposed an unsupervised learning technique with the help of this quaternion concept, and they have jointly considered the color and intensity. The experimentation was performed on UCM and Brazilian coffee datasets. The proposed model has given better accuracy than the existing techniques [97]. With the enhancement of deep learning techniques, we are able to classify remotely sensed images using unsupervised learning techniques, more accurately. When available labeled data samples are limited, it becomes difficult to perform image classification using supervised learning techniques [98]. Scene image classification is a hot topic these days; with these classification and analysis techniques, we are able to perform land cover and land use surveys, urban area planning,



FIGURE 12: Picture gallery taken from all classes of DIOR dataset.

disaster management and planning, crop analysis, weather prediction, and so on much easily and with high accuracy [99]. Previously BOW was the unsupervised learning technique that was used for remote sensing image classification. The article discussed below mentions a new technique. To overcome the issue of less labeled data, a new technique is proposed, and it is multilayered feature matching technique. The model uses both discriminative and generative models for learning unlabeled data. The experimentation was performed on two datasets: UCM and coffee, and as compared to other existing techniques, this proposed model MARTA GAI_{ns} outperforms with the classification accuracy of 94.86% and 89.86%, respectively [100].

6.1. Reinforcement Learning. Reinforcement learning is the concept of training a model for classification purpose where we reward the correct behavior and punish the undesired behavior. Reinforcement learning is the subbranch of machine learning which is quite similar to unsupervised learning where there are no labels assigned to the image. In reinforcement learning, agents learn the parameters and predict the outcomes [101]. On that prediction, there is a reward and punishment, and this process carries on till the game ends. Mostly reinforcement learning is used in gaming

and in AI and robotics where you need to teach a robot some new tricks. There are subelements of reinforcement learning that include policy, reward, value function, and environment as a model [102]. The reinforcement learning has achieved a new height as it is really helpful in minimizing the gap between training loss and matrix evaluation [103]. Captioning image is a challenging and most needed task of remote sensing. Most of the existing ML models suffer from the problem of overfitting. Below mentioned article has overcome this issue by proposing a two-stage model, one stage is for autoencoding variations while in stage 2, reinforcement learning is introduced. CNN is fine-tuned in stage 1, and in stage 2, it generates image captions. Reinforcement learning is then applied to improve the accuracy of the model. The experimentation was performed on NWPU-RESISC45 dataset. The results are far better than the previously mentioned results. But there exists a problem of overfitting, which should be addressed in future [104]. Fully polarized radar has the advantage to capture images throughout the time regardless of weather conditions. They are useful for land cover land use type applications, crop management, forest estimation, disaster prevention, recognition of targets, and many more. The article discussed below proposed a new model called deep Q network (DQN) that is basically a deep neural network model for polarized SAR image classification. The data are first preprocessed to

reduce noise and extract features. The data are then fed into deep neural network for classification purpose where the concept of reinforcement learning is introduced. The experimentation was performed on two PolSAR image datasets and the researchers claim that their model outperforms on many existing models [105].

7. Optimization Techniques for Remote Sensing Image Classification

Optimization is the process of finding those input values that best find the output, and there should be a well-defined objective function. This is a very critical task for which there exist multiple machine learning algorithms. Optimization means to minimize operational cost and improve accuracy. An optimization algorithm tries different solutions until it gets the best suitable result which gives the most optimal solution to that problem [106]. In remote sensing image classification, selection of features is basically the most crucial task and it depends on number of available labeled samples. Feature selection is the process of selecting more important features out of the pool of features and excluding correlated features. In the article discussed below, there is a solution proposed for this feature selection task. For this purpose, the stochastic method is introduced for selection of relevant and important features.

The experimentation was performed on two datasets: AVIRIS and ROSIS, and the results show that the proposed method gives better accuracy than the existing approaches [107]. Feature selection is one of the most important tasks in remote sensing image classification. Due to huge amount of data and correlated features, it becomes very tricky. To overcome this issue, a new methodology is introduced, and it has added the concept of wavelet analysis. Threefold strategy is introduced in this framework: in the first phase, the resolution technique is modified, and in the second phase, 3-D discrete wavelet transformation is introduced. In the last phase, CNN is introduced, and the performance of this new model is tested on three different datasets: Indian Pines, University of Pavia, and Salinas datasets. The accuracy achieved using this model is 99.4%, 99.85%, and 99.8%, respectively [108].

When dealing with hyperspectral remote sensing, we usually have limited samples for training. Using the conventional techniques, it has become difficult to achieve high accuracy. SVM gives the better accuracy as it has good generalization and least structural risk, and it overcomes the issue of high time consumption and less optimized parameters. The article discussed below uses EO-1 Hyperion to optimize the parameters. The proposed model is tested, and the authors claimed that they have reached the accuracy of 91.3% which is quite higher than that of the existing approaches [109]. Remote sensing image classification has a huge benefit for land use land cover cases which is a latest research area. Existing classification methods have the issue of low efficiency and they usually have larger datasets. To overcome this issue, a new method is proposed where the concept of extreme programming is introduced. Ensemble methods along with full use of features and deep learning

methods are introduced into the proposed model. All the three methods give better accuracy in terms of classification and efficiency, and the experimentation was performed on multiple datasets; classification accuracy depends upon the type of dataset. The optimization technique combined with deep learning outperforms as compared to other methods [110]. There are many optimization techniques covering different aspects of image classification task: the summary of the techniques is described in later section.

7.1. Grey Wolf Optimization. Grey wolf optimization (GWO) is a new metaheuristic technique, and it mimics the leadership quality of grey wolves [111]. There are four types of grey wolves, namely, alpha, beta, omega, and delta. The fittest solution is called as alpha, second best is called beta, 3rd one is called delta, and the last one is omega. There are three steps of hunting: searching for prey, encircling prey, and attacking prey; these three steps are implemented to get the optimized performance. This technique is basically a feature selection-based technique [112, 113]. In HSI, there are many consecutive and narrow spectral bands that give information about various land covers. Due to number of features, the time complexity increases. Selecting the best features out of the pool of features is a difficult and challenging task. The article discussed below proposed a new technique for feature selection of HSI, and it reduces redundant features. Fuzzy C-means algorithm is used for the decomposition of feature subset, whereas wolf optimization and max entropy are used for feature selection. The experimentation was performed on three known datasets: Indian Pines, Pavia University, and Salinas. The proposed methods outperform in terms of classification accuracy of existing techniques [114]. Image processing and analysis is an emerging field of computer vision. It has many different applications like image classification, segmentation, medical imaging, compression of image, and many more. There exist multiple algorithms to solve these issues like GA, GP, grey wolf algorithm, bat algorithm, and so on. The article discussed below is a review of multiple optimization techniques, their usage, and their real-world applications [115]. Grey wolf is one of the recent trends which comes under the umbrella of swarm intelligence. It has better performance than swarm intelligence and hence is used more effectively than swarm intelligence, and it is simpler to implement and easy to understand. The article discussed below is a review of multiple applications of grey wolf techniques and its applications [116]. We can summarize these optimization algorithms as follows:

- (i) Grey wolf algorithm can handle large data efficiently, but it ignores smaller details which need to be addressed.
- (ii) Grey wolf divides the features into four groups; in future, there should be a direction where more or less than four groups are formed.
- (iii) Effectiveness of grey wolf should be checked in combination of different optimization algorithms.
- (iv) There should be a focus on solving dynamic problems using GWO.

- (v) Parameter tuning of GWO could also be focused in future.

Table 6 shows the summary of some of the optimization techniques described in literature.

8. Fusion of Deep Learning with Spectral Features

Classification accuracy of hyperspectral images (HSI) has increased drastically when using in combination with CNNs. To perform better, it is needed to have denser network which as a result causes overfitting, degradation of accuracy, and also gradient vanishing. To overcome these issues, a new framework hierarchical feature fusion network (HFFN) is proposed. The main idea behind this model is to fuse the output of all the layers which results in increase of accuracy. The experimentation was performed on three real HSI datasets: AVIRIS Indian Pines image, ROSIS-03 University of Pavia image, and AVIRIS Salinas image. The experimental results were compared with DCNN, SVM, and DRN. The results showed that the proposed method outperforms as compared to existing DL methods [117].

CNNs are known as most powerful methods when talking about hyperspectral image classification. Usually pooling layers and sampling features of CNNs are fixed, so they cannot be used for downsampling of features. A research article proposed a deformable HIS. The proposed method is evaluated on two real HSI datasets: University of Pavia and Houston University, and they have 12 and 15 classes, respectively. 1st experiment was performed on Pavia dataset where training samples (45, 55, and 65) are randomly selected from each class. The results showed that the proposed method accurately classifies pixels in the near edge regions. The 2nd experiment was performed on Houston dataset where training samples (30, 40, and 50) were also randomly selected from each class. It has been observed that the proposed method performs better than other existing methods [118].

A deeper network with 9 layers is proposed called as contextual deep CNN, and the idea behind this research is to have a model that can accurately find local contextual interactions by jointly exploiting local spatio-spectral relationships of neighboring individual pixel vectors, as shown in Figure 13

In the first step, multiscale joint exploitation of the spatio-spectral information is obtained through filter bank which is then combined in a map. The experimentation is performed on three datasets: the Indian Pines dataset, the Salinas dataset, and the University of Pavia dataset. Indian Pines dataset has 12 classes but only 8 were used as there were so many images. Pavia dataset has 16 classes, and all of them were considered for experimentation. The accuracy of Indian Pines using proposed technique is 93.6%, that of Salinas is 95.07%, and that of Pavia is 95.97% [119].

Hyperspectral image (HSI) is a new research area. In this article, a special CNN model is proposed that performs the desired classification by using lesser training and fine-tuning of data. To perform this task, the pixels can be pulled from the same class closer, while pushing the different class pixels farther away. The experimentation is performed on three

TABLE 6: Optimization techniques.

Application	Techniques
Segmentation	Grey wolf optimizer
	Genetic programming
	Genetic algorithm
	Particle swarm optimization
	Cuckoo search algorithm
Classification	Bat algorithm
	Grey wolf optimizer
	Genetic programming
Medical imaging	Particle swarm optimization
	Grey wolf optimizer
	Differential optimization
Compression	Bat algorithm

HSI datasets: Indian Pines, Pavia, and Salinas. The results were validated on AlexNet, VGG-CNN-S, and GoogLeNet. The previous accuracies were 88.45%, 85.5%, and 88.8%, respectively, whereas the proposed model gives accuracies of 96.21%, 86.46%, and 88.48%, respectively [120].

In [121], a new model SAFF is proposed. In the 1st phase, multiple labels were identified by using pretrained CNNs and then a self-attention layer is added for channel-based and spatial-based weight assigning. At the end, SVM was used for classification. The experimentation was performed on three different datasets: (1) UC Merced Land Use Dataset having 2100 images and 21 classes; (2) Aerial Image Dataset having 10000 images and 30 classes; and (3) NWPU-RESISC45 Dataset with 31,500 images and 45 classes. The overall accuracy of UCM dataset is 97.02%, that of AID dataset is 90.25%, and that of NWPU dataset is 84.38%.

9. Feature Fusion

Earlier in the literature, we have seen that for image retrieval, one technique was used; later on, it was observed that fusion of more than one techniques can give better accuracy [122]. In this article, a new model weight feature convolutional neural network (WFCNN) is proposed that performs segmentation and extraction of information from images. The WFCNN model first performs encoding and then classification is performed. The proposed model is trained by using stochastic gradient decent (SGD) algorithm. The experimentation was performed on two datasets: Gaofen 6 images and aerial images. The results are validated using SegNet, U-Net, and RefineNet models. GF-6 datasets give accuracy of 94.13%, and aerial image dataset gives accuracy of 96.9% [123]. Ren et al. [124] proposed a full CNN based on multiscale feature fusion for the class imbalance for remote sensing image classification. The authors named the proposed research model as DeepLab V3+, with loss function based solution of samples imbalance [124]. Experimentation was performed on 2 datasets: sentinel-2 and sentinel-3. When compared with U-Net, PSPNet, and ICNet, the proposed method gives accuracy up to 97% [124]. This article proposed a new technique where large image is divided into small-scale images. To divide the samples into classes, support vector machine (SVM) is used. After this phase, a new module called active learning is added. The proposed model

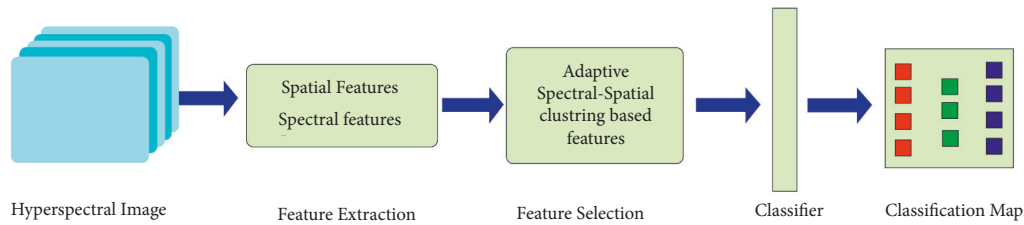


FIGURE 13: Block diagram representing details about spectral feature extraction.

(SSFFSC-AL) performs better in terms of classification accuracy and also gives results in lesser time. The experimentation was performed on two datasets: Indian Pines and Pavia [125]. Feature fusion has two basic methods: local feature fusion and global feature fusion.

Zhu et al. [126] claimed about local and global feature fusion for high-resolution spatial images for scene classification. They have merged two different techniques for feature fusion: local and global fusion. The datasets used for the experimentation are 21-class UC Merced and 12 class Google dataset of SIRI-WHU. Google dataset reached the accuracy of 99.76%, whereas the other one has 96.37%. Future directions identified from this article are

- (1) To use social media data for this training purpose.
- (2) To improve classification accuracies of remote sensing images.
- (3) To implement this research on non-optical data.

Li et al. [127] discussed about scene image classification by fusion strategy to integrate multilayer features using CNN for pretrained data. CNN was used for feature extraction process and then fully connected layers were used for deep feature extraction; then, these extracted features were fused using PCA; after that, classification process was performed. The datasets used for the experimentation are WHU-RS and UCM, and the authors claim that they have achieved better accuracy than previously implemented classification processes. The gap identified in this article is to reduce computational time and to improve classification accuracy [127].

Yuan et al. in [128] discussed scene image classification which was performed by global rearrangement of local features, and the rearrangement of local features helped to get spatial information of the image. The experimentation was performed on four different datasets: UCM, WHU-RS19, Sydney, and AID, and they claimed that the performance was satisfactory. In future, there should be a focus towards improvement of classification accuracy.

In [128], the multilayer covariance pooling technique was used for extraction of features; then, these features were stacked to form a covariance matrix, and finally support vector machine was used for classification. The experimentation was performed on UCM, AID, and NWPU-RESISC45 datasets, and the proposed method outperforms existing methods of classification. In future, there should be an end to end CNN model which is able to classify with better accuracy using lesser features maps at each layer.

A research article discussed feature aggregation to learn about scene classification. This model unites feature

learning, aggregation, and classification into CNN during training process. Fine-tuning is performed to alleviate the training process, and it works for insufficient data as well. The experimentation was performed on three datasets: AID, UCM, and WHU-RS19. The limitation of this research is that there should be a technique that can get semantic information of images without cropping or resizing of images [87].

Figure 14 shows the complete process of how features are extracted and image classification process is completed. Another article is an unsupervised feature fusion technique for training of CNN. Due to this, training becomes easier and more efficient; after that, feature fusion was performed to classify images. The experimentation was performed on UCM and Brazilian coffee datasets, and the proposed model gives better accuracy of 87.83%. There should be a focus on different feature fusion strategies to check their effect [73]. Table 7 summarizes the above-explained research articles.

10. Texture Features

Feature selection and extraction are the most important tasks in content-based image retrieval. There could be two types of features: global and local features. Global features include color, texture, shape, and spatial information, whereas local features have the information about image segmentation, edge detection, corners and blobs, and so on [129].

Texture features are considered to be most powerful features among all. They are the most visible and noticeable patterns in any image. But we cannot use texture features separately. Among low-level visual features, texture of an image is considered as a distinguishable image representation. They are the considered as the visible and noticeable pattern of an image. Different fusions of texture features have shown good results in different application of remote sensing and image retrieval [130].

With these pros, there are also some cons of texture feature extraction. Complexity increases while processing and extracting texture feature [131]. To overcome these issues, different forms of texture features extraction methods are reported in literature such as wavelet transform [132] and Gabor filter [133], and Table 8 presents a detailed summary about texture features.

In this article [134], a new technique is proposed for classification and extraction of features from SAR images. The method is divided into three phases. In the 1st phase,

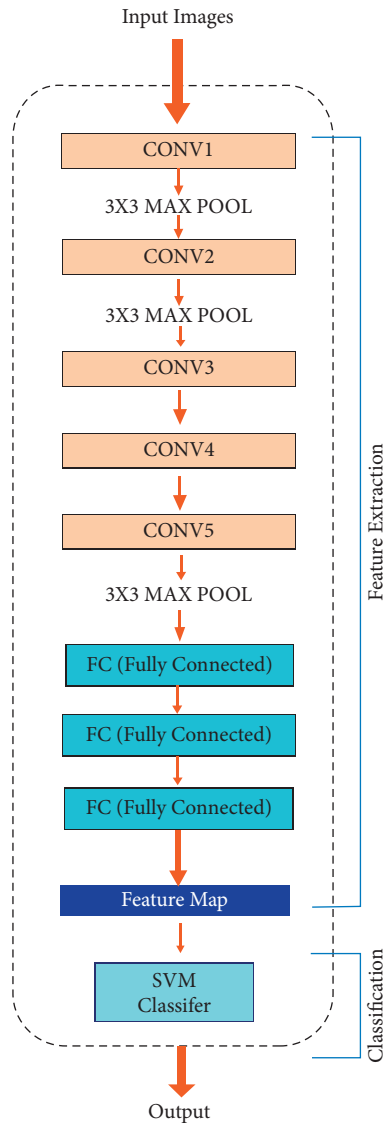


FIGURE 14: Deep learning model.

two types of features were extracted: grey level co-occurrence matrix and Gabor filter. In phase 2, dimensionality is reduced, and at final phase, SVM is introduced for image classification. The experiments showed that this model gives better classification accuracy and is also good for dimensionality reduction. SAR image dataset is used for experimentation, and accuracy is 87.5% [134].

Speckle effect is a very common issue of PolSAR. To overcome this issue, a special technique is proposed that first extracts the features and then classifies them. Real PolSAR images were used for experimentation process and then validated using existing techniques. This article claims that they have reached the accuracy up to 99.8% [135].

Hyperspectral sensors can collect huge amount of data now. But it is still challenging to classify HSIs accurately. The technique used in previous research was spatio-spectral classification, but these were not able to classify images accurately. In this article, the author proposed a new technique to classify images, and this technique is the process that is carried out in three

phases. In the 1st phase, feature extraction is performed, and in the 2nd phase, images were classified using probabilistic SVM, while in the 3rd and last phase, probabilities were calculated to find the results. The experimentation was performed on two different HSI datasets: Indian Pines and Pavia. The results showed that the classification accuracy of the proposed model is better as compared to previously used techniques [136].

Kai et al. [137] claimed that they extracted texture features using the Gabor method. The datasets used for the experimentation are Corel, Li, and Caltech 101. They managed to improve accuracy. The results showed 83%, 88%, and 70% accuracy of each dataset, respectively. The main limitation identified in this research is the increase in computational cost while feature extraction. In [138], Sajjad et al. reported that texture features could be extracted efficiently using the wavelet method. They have claimed high accuracy of 99%, 56%, and 35% on Corel 1K, Corel 5K, and Corel 10K, respectively. Using wavelet methods of texture feature extraction, we can increase accuracy but computation cost also increases as a result. In another article [139], Sajjad et al. extracted texture features using the histogram method. The experimentation was performed on Corel 1K and Corel 5K datasets. Classification accuracy was 87%. In 2018, it is reported in their research that texture features extracted using the edge detection method give better accuracy, i.e., 98%. The dataset used for the experimentation is NUSWIND. The limitation of this research is the increase in computation cost.

Wang et al. [140] found that texture features extracted using Canny edge detector give better accuracy of 68%. The dataset used for experimentation is Corel 10K. The drawback of this research is increase in running cost as the number of input images was very large.

Nazir et al. [141] stated in their article that texture features extracted through discrete wavelet transform (DWT) and edge histogram descriptor (EDH) have better accuracy than those of other methods. The experimentation was performed on Corel dataset. The accuracy reported in this article is 73.5%. The drawback of this research is that no machine learning methods were used for classification or extraction of features.

In [142], Thusnavis Bella and Vasuki used the ranklet transformation method for texture feature extraction. They claimed that they have increased the accuracy. The datasets used in their experimentation are Corel 5k and Corel 10K. Accuracies measured in the article are 67.4% and 67.9%, respectively. The limitation of this research is that due to many dimensions of texture features, the computation cost increased.

Bella et al. [142] performed texture feature extraction using the grey level co-occurrence matrix (GLCM) method. The dataset used in this experiment was Corel 5K, and they achieved accuracy of 66.9%. The computation accuracy is very high, as there was no algorithm used in their experimentation to reduce computational cost.

In [143], Ashraf et al. [143] claimed that using Gabor filter they have extracted texture features. The accuracy achieved in this experimentation was 79% while dataset was Corel 5K. The limitation of this research is also the increase

TABLE 7: Feature fusion.

Title	Year	Methods	Datasets	Limitations
Integrating multilayer features of convolutional neural networks for remote sensing scene classification [127]	2017	Fisher kernel coding	WHU_RS dataset, UCM dataset	To reduce computational time and to improve classification accuracy.
A deep-local-global feature fusion framework for high spatial resolution imagery scene classification [126]	2018	Deep-local-global feature fusion	21-class UC Merced dataset, 12-class Google dataset of SIRI-WHU	Same process could be implemented on non-optical images.
Remote sensing scene classification using multilayer stacked covariance pooling [129]	2018	Multilayer stacked covariance pooling (MSCP)	UC Merced land use dataset, AID30, NWPU-RESISC45 dataset	There should be an end to end CNN model which is able to classify with better accuracy using lesser features maps at each layer.
Remote sensing image scene classification using rearranged local features [128]	2019	Global and rearranged local features	UC Merced, WHU-RS19, Sydney, AID	To explore more techniques for feature fusion.
A feature aggregation convolutional neural network for remote sensing scene classification [130]	2021	Feature aggregation convolutional neural network (FACNN)	AID, UC Merced, WHU-RS19	There should be a technique that can get semantic information of images without cropping or resizing of images.

in computational accuracy as there are many feature dimensions.

In [144], Alsamadi et al. [144] reported that they have extracted texture features using the DWT method. The dataset used in the experimentation was Corel, and they achieved accuracy of 90%. The limitation of this research is high computational time.

11. Hybrid Approaches

In this article, a hybrid approach is used to accurately classify remotely sensed aerial images. SVM and KNN were combined in this article. First SVM was trained to classify images into different classes. In the testing phase, newly tested samples were entered, and average distance between the test samples for each class was calculated using the distance formula. Lastly, the images are placed to their respected classes where there is minimum average distance. This process is repeated till all the images are sorted into their respective classes. The experimentation was performed on two datasets: the ALOS data of the Yitong River and PMS sensor. The results are quite impressive, i.e., 92.44% and 97.8%, respectively [148].

In an article, both parametric and non-parametric approaches were combined to classify the remote sensing images especially land cover land use data. Also, a new dataset was proposed in this article for this purpose which can also be used in other related research. The data of land were captured for both dry and wet conditions. The proposed model is basically the combination of ISODATA clustering and decision trees. The accuracy achieved for dry conditions is 84.54%, whereas for wet weather conditions, the accuracy is measured as 91.10%, which is better than existing deep learning models [149].

In an article, the authors combined two algorithms: kernel-internal value fuzzy C-means clustering and multi-value C-means clustering; by comparing the results with conventional fuzzy C-means clustering, it was observed that

the proposed methods outperform the existing methods. They have constructed a new dataset: LANDSAT-7 Ba Ria area and Hanoi area. The accuracy noted in this research was 98.2% and 94.13%, respectively [11].

An article explains the phenomenon of sparse code that is used to reduce the calculation time for feature extraction. SC is commonly used for aerial images as it performs better in this particular case. With the help of existing approach, accuracy of local feature extraction is increased as compared to existing techniques. The experimentation was performed on UAS operating system data that are recorded for nearly 2 hours without flight interruptions. The accuracy achieved is 85.7% [150].

An article states that the combination of two techniques: pixel-based multilayer perceptron and CNN. This combined algorithm is applied on a dataset that is obtained through aerial photography and satellite. The dataset contains images of both urban and rural lands of different land uses of Southampton. The proposed method outperforms the existing deep learning methods. The accuracies achieved from this proposed model are 90.93% for urban and 89.64% for rural lands [151].

It states the hybrid approach that combines two techniques, SVM and ANN, for LULC classification of images captured through satellite. The fuzzy hierarchal clustering approach is used for classification purpose as shown in Figure 15.

The dataset "Landsat-8 satellite images" is also proposed in this research. All the data are obtained from lands of Hyderabad and its surroundings. The accuracy achieved in this article are 93.159% for SVM and 89.925% for ANN. The authors claim that the proposed method gave better results than existing methods [153].

Yang et al. [134] proposed an efficient classification technique for agricultural lands that is based on spatial and spectral image features. Here a hybrid approach was used for classification purposes of healthy and non-healthy plants. Unmanned aerial vehicle (UAV) images of rice fields in Chianan Plain and Taibao City, Chiayi County, were collected. The accuracy achieved in this research is 90.67% [154].

TABLE 8: Texture feature-based models.

Title	Methods	Datasets	Accuracy	Limitations
Alexey et al. [145]	Gabor	Corel, Li, Caltech101	83%, 88%, 70%	Increase in computational cost
Song et al. [117]	Wavelet	Corel 1K, Corel 5K, Corel 10k	99%, 56%, 35%	Increase in computational cost
Zhu et al. [118]	Histogram	Corel 1K, Corel 5K	87%	-
Phadikar et al. [146]	MPEG-7 edge detector	NUSWIND	98%	Computational cost increased by using GA
Sharmila and Sharmila [147]	Canny edge detector	Corel10K	68%	Running cost increased due to large image input
Cao et al. [121]	DWT,EDH	Corel	73.50%	No ML used in experimentation
Deselaers et al. [122]	Ranklet transformation	Corel 5K, Corel 10K	67.4%, 67.9%	Computational cost increased due to multiple dimensions of features
Zhang et al. [123]	GLCM	Corel 5K	66.90%	No optimization algorithm is used to reduce computational complexity
Ren et al. [124]	Gabor filter	Corel 5K	79%	Computational cost increased because of feature dimensions
Mu et al. [125]	DWT	Corel	90%	High computational time

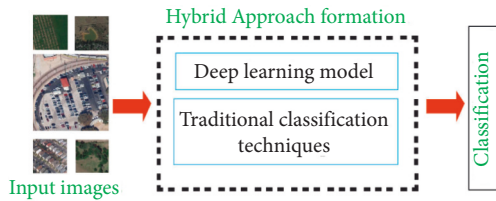


FIGURE 15: Hybrid approaches.

Another article explains the research of a hybrid approach used for classification of remote sensing images. SVM and KNN were combined in this research for better results. Two datasets were used for experimentation: dataset-1 contains “ALOS data of the Yitong River in Changchun,” whereas dataset-2 contains “the ortho image of a factory region in Jiangsu Province.” The accuracies achieved are DS-1: 92.4% and DS-2: 97.9% [155].

An article explains a disaster scenario of southern India which was hit by flood. Data captured in this research were 200 flooded and non-flooded images. The approach used for research is the combination of SVM and K-means clustering. The accuracy achieved was 92%. Bitner et al. [157] extracted automatic building footprint by extracting multiresolution remote sensing images using a hybrid approach. The data of World View-2 imagery of Munich, Germany, were collected through satellite. The experimentation is performed by combining approaches, i.e., U-Net on top of the Caffe deep learning framework. The new hybrid technique performs better than existing techniques. The accuracy achieved is 97.4% [157]. The summary of all the hybrid approaches explained in the above section is given in Table 9.

12. Performance Evaluation Criteria

To evaluate the performance of classification, there are many ways that exist in the literature [65, 158]. The selection of performance measure purely depends upon the type of classification we are going to perform and what type of results are

required. The selection of algorithm for classification purpose also plays an important role for the selection of performance metrics. Following are the performance metrics used to check the accuracy of classification:

True positive (TP): number of images that are correctly labeled

True negative (TN): number of images that are incorrectly labeled

False positive (FP): assigning label to an image when it does not belong to that class

False negative (FN): not assigning label to the image when it really belongs to that class

Below mentioned are some of the types to measure performance of content-based image retrieval:

- (i) Precision/predictive value: it is the ratio of relevant output to the total number of output image.

$$\text{Precision} = \frac{TP}{TP + FP} \quad (1)$$

- (ii) Average precision: it can be defined as the mean of all the related queries.

$$\text{Avg.Precision} = \sum_{k=1}^{nNRI} p(k) \times \frac{R(k)}{NRI} \quad (2)$$

- (iii) Mean average precision: it is defined as the mean of average mean of all the relevant queries.

$$\text{MAP} = \sum_{(q=1)}^S AP \frac{(q)}{S} \quad (3)$$

where S is the no. of queries.

TABLE 9: Hybrid approaches.

Ref.	Approaches	Datasets	Accuracy
Kantakumar et al. [149]	Maximum likelihood supervised, decision tree, and ISODATA clustering technique	Landsat-8's dataset for dry period and wet period	Dry: 84.54%; wet: 91.10%
Nguyen et al. [11]	Fuzzy C-means clustering and multiple kernel interval-valued fuzzy C-means clustering	LANDSAT-7 Ba Ria area and Hanoi area	98.2% and 94.13%
Qayyum et al. [150]	DRT hybrid dictionary with Ricker wavelet function	UAS operating system recorded data for nearly 2 h without flight interruptions	85.70%
Zhang et al. [151]	CNN and MLP (multilayer perceptron)	Urban and rural scenes of aerial imagery of Southampton	90.93% for urban and 89.64% for rural
Nijhawan et al. [152]	Hybrid of CNN integrated with handcrafted (LBP + GIST) features	Satellite images of Uttarakhand, northern part of India	88.43%
Prasad et al. [153]	Landsat-8 satellite images	SVM and ANN	SVM: 93.15%; ANN: 89.92%
Yang et al. [154]	UAV images of rice fields in Chianan Plain and Taibao City, Chiayi County	DSM and texture information	90.67%
Alimjan et al. [148]	SVM and KNN	DS-1: ALOS data of the Yitong River in Changchun DS-2: the ortho image of a factory region in Jiangsu Province	DS-1: 92.4%; DS-2: 97.9%
Akshya et al. [155]	SVM and K-means	A dataset containing 200 flooded and non-flooded images	92%
Hua et al. [156]	Class-wise attention-based convolutional and bidirectional LSTM network	UCM and DFC15 multilabel datasets	
Schuegraf et al. [157]	U-Net on top of the Caffe deep learning framework	World View-2 imagery of Munich, Germany	97.40%

(iv) Precision recall curve: it is the trade-off between precision and recall under different thresholds.

(v) Recall/sensitivity: it is the ratio of relevant output to all the input and output queries.

$$\text{Recall} = \frac{TP}{TP + FN}. \quad (4)$$

(vi) F -measure: it is the harmonic mean between precision and accuracy.

$$F - \text{measure} = 2 \left(\frac{P \times R}{P + R} \right). \quad (5)$$

(vii) Negative predictive value: it can be defined as the ratio between correctly labeled negative images to total number of negatively labeled images.

$$\text{Negative predictive value} = \frac{TN}{TN + FN}. \quad (6)$$

(viii) Specificity: it is the ratio between correctly labeled negative images to total number of negative images.

$$\text{Specificity} = \frac{TN}{TN + FP}. \quad (7)$$

(ix) Accuracy: it is the ratio of all the results either rightly labeled or falsely labeled to total number of labels that exist.

$$\text{Accuracy} = \frac{TP + TN}{TP + FP + FN + TN}. \quad (8)$$

(x) Overall accuracy: it is defined as the sum of overall accuracy of total correctly labeled images to all the existing images.

$$w = \sum_{i=0}^{nc} e \frac{ii}{NT}, \quad (9)$$

$$NT = \sum_{i=1}^{nc} \sum_{j=1}^{nc} eij,$$

where w = overall accuracy, NT = sum of all non-diagonal elements in confusion matrix, and eij = total correct cells.

(xi) Mean square error: the most popular metric used for measuring the error is mean square error. It computes the average of the squared difference between the target value and the value predicted by the model.

$$\text{MSE} = \frac{1}{N} \sum_{j=1}^N (y_j - y'_j)^2, \quad (10)$$

where N = the last iterations, y_j = true value, and y'_j = value predicted by the model.

(xii) Mean absolute error: when we try to compute the average between the actual value and predicated value we use MAE. The mathematical representation of the metric is given below.

$$\text{MAE} = \frac{1}{N} \sum_{j=1}^N |y_j - y'_j|, \quad (11)$$

where N = the last iterations, y_j = true value, and y'_j = value predicted by the model.

- (xiii) Root mean square error: it is easy to compute and gives a better idea of how well the model is performing. We just have to take the square root of average of the squared difference between the target value and the value predicted. Mathematically, it is pictured as

$$D = \sqrt{\frac{1}{N} \sum_{j=1}^N (y_j - y'_j)^2}. \quad (12)$$

- (xiv) Area under the receiver operating characteristic curve (AUROC): this is a very interesting metric and is also known as AUC-ROC score/curves. While computing AUROC, true positive rate (TPR) and false positive rate (FPR) are used. Mathematically, it is represented as follows:

$$\text{TRP} = \frac{TP}{TP + FN}, \quad (13)$$

$$\text{FRP} = \frac{FP}{FP + TN}.$$

13. Conclusion and Future Directions

Remote sensing image analysis is used in various real-time applications such as monitoring of Earth, urban development, town planning, water resources engineering, providing construction requirements, and agriculture planning. Image analysis and classification is an open research problem for the research community working on remote sensing applications. Due to recent development in imaging technology, there is an exponential increase in the number and size of multimedia contents such as number of videos and digital images. Due to this increase in this volume of digital images, the automatic classification of images is an open research problem for computer vision research community. Various research models are proposed in recent years, but there is still a research gap between human understanding and machine perception. Due to this reason, the research community working on remote sensing image analysis is exploring the possible research directions that can bridge this gap. The earlier approaches for remote sensing image analysis are based on low-level feature extraction and mid-level feature representation. These approaches have shown good performance on small-scale image benchmarks with limited training and testing samples. The use of discriminating feature representation with multiscale features can boost the performance of the learning model. These approaches can mainly assign single labels to images, while in existing era, it is a requirement to assign multiple labels to

single image on the basis of contents. One of the main requirements of a deep learning model is to build a large-scale image benchmark that can be helpful to train a complex deep network. The creation of a large-scale image benchmark with all possible classes of remote sensing images is one of the main requirements and an open research problem in this domain. Most of the current research models based on deep learning are mainly using the fine-tuning and data augmentation techniques to enhance learning. If a large-scale image benchmark is available, it will assist the learning model to learn parameters in a more effective way. The available large-scale image benchmarks are used through supervised learning, and this is a time consuming process and such fully supervised learning models are computationally expensive. Exploring the possible learning capabilities based on unsupervised and semi-supervised learning is a possible future research direction. The deep learning models use extensive computational power for training, and mostly, the research models are using GPUs as high-performance computing. Designing a deep learning model with less computations is also a possible research direction, and such model can be used on a device with less computation powers. The use of few-shot/zero-shot learning approaches can be explored in the field of remote sensing image classification.

Data Availability

The details about the data used is mentioned and cited within this manuscript.

Conflicts of Interest

The authors declare that they have no conflicts of interest.

References

- [1] C. Shi, X. Zhang, J. Sun, and L. Wang, "Remote sensing scene image classification based on self-compensating convolution neural network," *Remote Sensing*, vol. 14, no. 3, p. 545, 2022.
- [2] S. Karimi Jafarbigloo and H. Danyali, "Nuclear atypia grading in breast cancer histopathological images based on cnn feature extraction and lstm classification," *CAAI Transactions on Intelligence Technology*, vol. 6, no. 4, pp. 426–439, 2021.
- [3] X. Zhang and G. Wang, "Stud pose detection based on photometric stereo and lightweight yolov4," *Journal of Artificial Intelligence and Technology*, vol. 2, no. 1, pp. 32–37, 2022.
- [4] A. Shabbir, A. Rasheed, H. Rasheed et al., "Detection of glaucoma using retinal fundus images: a comprehensive review," *Mathematical Biosciences and Engineering*, vol. 18, no. 3, pp. 2033–2076, 2021.
- [5] W. Zhang, P. Du, P. Fu et al., "Attention-aware dynamic self-aggregation network for satellite image time series classification," *IEEE Transactions on Geoscience and Remote Sensing*, vol. 60, pp. 1–17, 2022.
- [6] N. Hamid and J. R. Abdul Hamid, "Multi level image segmentation for urban land cover classifications," *IOP Conference Series: Earth and Environmental Science*, vol. 767, no. 1, Article ID 012024, 2021.

- [7] S. Fatima, N. Aiman Aslam, I. Tariq, and N. Ali, "Home security and automation based on internet of things: a comprehensive review," *IOP Conference Series: Materials Science and Engineering*, vol. 899, no. 1, Article ID 012011, 2020.
- [8] Q. Zou, K. Xiong, Q. Fang, and B. Jiang, "Deep imitation reinforcement learning for self driving by vision," *CAAI Transactions on Intelligence Technology*, vol. 6, no. 4, pp. 493–503, 2021.
- [9] M. Arsalan Aslam, M. Naveed Salik, F. Chughtai, N. Ali, S. Hanif Dar, and T. Khalil, "Image classification based on mid-level feature fusion," in *Proceedings of the 15th International Conference on Emerging Technologies (ICET)*, pp. 1–6, IEEE, Peshawar, Pakistan, February 2019.
- [10] Z. Y. Lv, W. Shi, X. Zhang, and J. A. Benediktsson, "Landslide inventory mapping from bitemporal high-resolution remote sensing images using change detection and multiscale segmentation," *Ieee Journal of Selected Topics in Applied Earth Observations and Remote Sensing*, vol. 11, no. 5, pp. 1520–1532, 2018.
- [11] D. D. Nguyen, L. T. Ngo, L. T. Pham, and W. Pedrycz, "Towards hybrid clustering approach to data classification: multiple kernels based interval-valued fuzzy c-means algorithms," *Fuzzy Sets and Systems*, vol. 279, pp. 17–39, 2015.
- [12] M. Sajid, N. Ali, S. H. Dar et al., "Data augmentation-assisted makeup-invariant face recognition," *Mathematical Problems in Engineering*, vol. 2018, pp. 1–10, Article ID 2850632, 2018.
- [13] M. Saqlain, S. Rubab, M. M. Khan, N. Ali, and S. Ali, "Hybrid approach for shelf monitoring and planogram compliance (hyb-smpc) in retails using deep learning and computer vision," *Mathematical Problems in Engineering*, vol. 2022, pp. 1–18, Article ID 4916818, 2022.
- [14] N. Ali, B. Zafar, F. Riaz et al., "A hybrid geometric spatial image representation for scene classification," *PLoS One*, vol. 13, no. 9, Article ID 0203339, 2018.
- [15] A. Latif, A. Rasheed, U. Sajid et al., "Content-based image retrieval and feature extraction: a comprehensive review," *Mathematical Problems in Engineering*, vol. 2019, pp. 1–21, Article ID 9658350, 2019.
- [16] K. Yadav, M. Yadav, and S. Saini, "Stock values predictions using deep learning based hybrid models," *CAAI Transactions on Intelligence Technology*, vol. 7, no. 1, pp. 107–116, 2022.
- [17] Ke Li, G. Wan, G. Cheng, L. Meng, and J. Han, "Object detection in optical remote sensing images: a survey and a new benchmark," *ISPRS Journal of Photogrammetry and Remote Sensing*, vol. 159, pp. 296–307, 2020.
- [18] M. Asif, M. Bin Ahmad, S. Mushtaq, K. Masood, T. Mahmood, and A. Ali Nagra, "Long multi-digit number recognition from images empowered by deep convolutional neural networks," *The Computer Journal*, vol. 117, 2021.
- [19] Qi Wang, S. Liu, J. Chanussot, and X. Li, "Scene classification with recurrent attention of vhr remote sensing images," *IEEE Transactions on Geoscience and Remote Sensing*, vol. 57, no. 2, pp. 1155–1167, 2019.
- [20] S. Li, W. Song, L. Fang, Y. Chen, P. Ghamisi, and J. A. Benediktsson, "Deep learning for hyperspectral image classification: an overview," *IEEE Transactions on Geoscience and Remote Sensing*, vol. 57, no. 9, pp. 6690–6709, 2019.
- [21] Si B. Chen, Q. S. Wei, W.-Z. Wang, J. Tang, B. Luo, and Zu. Y. Wang, "Remote sensing scene classification via multi-branch local attention network," *IEEE Transactions on Image Processing*, vol. 31, pp. 99–109, 2022.
- [22] N. Ali, B. Zafar, M. K. Iqbal et al., "Modeling global geometric spatial information for rotation invariant classification of satellite images," *PLoS One*, vol. 14, no. 7, Article ID 0219833, 2019.
- [23] X. Wang, S. Wang, C. Ning, and H. Zhou, "Enhanced feature pyramid network with deep semantic embedding for remote sensing scene classification," *IEEE Transactions on Geoscience and Remote Sensing*, vol. 59, no. 9, pp. 7918–7932, 2021.
- [24] M. M. Elkholy, M. S. Mostafa, H. M. Ebeid, and M. Tolba, "Unsupervised hyperspectral band selection with deep autoencoder unmixing," *International Journal of Image and Data Fusion*, vol. 13, no. 3, pp. 244–261, 2021.
- [25] A. Vali, S. Comai, and M. Matteucci, "Deep learning for land use and land cover classification based on hyperspectral and multispectral earth observation data: a review," *Remote Sensing*, vol. 12, no. 15, p. 2495, 2020.
- [26] H. Yang and W. Yang, "Gscctl: a general semi-supervised scene classification method for remote sensing images based on clustering and transfer," *International Journal of Remote Sensing*, pp. 1–25, 2022.
- [27] P. K. Sethy, "Identification of wheat tiller based on alexnet feature fusion," *Multimedia Tools and Applications*, vol. 81, pp. 8309–8316, 2022.
- [28] D. Wang, C. Zhang, and M. Han, "Mlfc net: a multi level feature combination attention model for remote sensing scene classification," *Computers & Geosciences*, vol. 160, Article ID 105042, 2022.
- [29] O. Kechagias-Stamatis and N. Aouf, "Automatic target recognition on synthetic aperture radar imagery: a survey," *IEEE Aerospace and Electronic Systems Magazine*, vol. 36, no. 3, pp. 56–81, 2021.
- [30] L. Gomez-Chova, D. Tuia, G. Moser, and G. Camps-Valls, "Multimodal classification of remote sensing images: a review and future directions," *Proceedings of the IEEE*, vol. 103, no. 9, pp. 1560–1584, 2015.
- [31] L. Zhang, L. Zhang, and Bo Du, "Deep learning for remote sensing data: a technical tutorial on the state of the art," *IEEE Geoscience and remote sensing magazine*, vol. 4, no. 2, pp. 22–40, 2016.
- [32] X. X. Zhu, D. Tuia, L. Mou et al., "Deep learning in remote sensing: a comprehensive review and list of resources," *IEEE Geoscience and Remote Sensing Magazine*, vol. 5, no. 4, pp. 8–36, 2017.
- [33] P. Ghamisi, J. Plaza, Y. Chen, J. Li, and A. J. Plaza, "Advanced spectral classifiers for hyperspectral images: a review," *IEEE Geoscience and Remote Sensing Magazine*, vol. 5, no. 1, pp. 8–32, 2017.
- [34] U. Chakraborty and D. Chakraborty, "Remote sensing image classification: a survey of support-vector-machine-based advanced techniques," *IEEE Geoscience and Remote Sensing Magazine*, vol. 5, no. 1, pp. 33–52, 2017.
- [35] W. Zhou, S. Newsam, C. Li, and Z. Shao, "Patternnet: a benchmark dataset for performance evaluation of remote sensing image retrieval," *ISPRS Journal of Photogrammetry and Remote Sensing*, vol. 145, pp. 197–209, 2018.
- [36] G. Cheng, J. Han, and X. Lu, "Remote sensing image scene classification: benchmark and state of the art," *Proceedings of the IEEE*, vol. 105, no. 10, pp. 1865–1883, 2017.
- [37] L. He, J. Li, C. Liu, and S. Li, "Recent advances on spectral-spatial hyperspectral image classification: an overview and new guidelines," *IEEE Transactions on Geoscience and Remote Sensing*, vol. 56, no. 3, pp. 1579–1597, 2018.

- [38] L. Ma, Yu Liu, X. Zhang, Y. Ye, G. Yin, and B. A. Johnson, "Deep learning in remote sensing applications: a meta analysis and review," *ISPRS Journal of Photogrammetry and Remote Sensing*, vol. 152, pp. 166–177, 2019.
- [39] S. Kumar and D. Kumar, "A review of remotely sensed satellite image classification," *International Journal of Electrical and Computer Engineering*, vol. 9, no. 3, p. 1720, 2019.
- [40] G. Cheng, X. Xie, J. Han, L. Guo, and G. S. Xia, "Remote sensing image scene classification meets deep learning: challenges, methods, benchmarks, and opportunities," *Ieee Journal of Selected Topics in Applied Earth Observations and Remote Sensing*, vol. 13, pp. 3735–3756, 2020.
- [41] M. Govind and S. K. Pandey and Dr, *A Comparative Study on Supervised and Unsupervised Techniques of Land Use and Land Cover Classification*, 2022.
- [42] G. De Luca, "A survey of nisq era hybrid quantum classical machine learning research," *Journal of Artificial Intelligence and Technology*, vol. 2, no. 1, pp. 9–15, 2022.
- [43] M. Alyas Khan, M. Ali, M. Shah et al., "Machine learning-based detection and classification of walnut fungi diseases," *Intelligent Automation & Soft Computing*, vol. 30, no. 3, pp. 771–785, 2021.
- [44] V. Nasiri, A. A. Darvishsefat, H. Arefi, V. C. Griess, S. M. M. Sadeghi, and S. A. Borz, "Modeling forest canopy cover: a synergistic use of sentinel 2, aerial photogrammetry data, and machine learning," *Remote Sensing*, vol. 14, no. 6, p. 1453, 2022.
- [45] D. Cabrera, L. Cabrera, and E. Cabrera, "Perspectives organize information in mind and nature: empirical findings of point-view perspective (p) in cognitive and material complexity," *Systems*, vol. 10, no. 3, p. 52, 2022.
- [46] N. Ali, K. B. Bajwa, R. Sablatnig et al., "A novel image retrieval based on visual words integration of sift and surf," *PLoS One*, vol. 11, no. 6, Article ID 0157428, 2016.
- [47] M. Wang, M. Wander, S. Mueller, N. Martin, and J. B. Dunn, "Evaluation of survey and remote sensing data products used to estimate land use change in the United States: evolving issues and emerging opportunities," *Environmental Science & Policy*, vol. 129, pp. 68–78, 2022.
- [48] R. Jacobsen, C. A. Bernabel, M. Hobbs, N. Oishi, M. Puig-Hall, and Z. Shannon, "Machine learning: paving the way for more efficient disaster relief," *AIAA SCITECH 2022 Forum*, p. 0397, 2022.
- [49] Z. Zheng, S. Du, H. Taubenböck, and X. Zhang, "Remote sensing techniques in the investigation of aeolian sand dunes: a review of recent advances," *Remote Sensing of Environment*, vol. 271, Article ID 112913, 2022.
- [50] D. J. Lary, A. H. Alavi, A. H. Gandomi, and A. L. Walker, "Machine learning in geosciences and remote sensing," *Geoscience Frontiers*, vol. 7, no. 1, pp. 3–10, 2016.
- [51] N. Ali, K. B. Bajwa, R. Sablatnig, and Z. Mehmood, "Image retrieval by addition of spatial information based on histograms of triangular regions," *Computers & Electrical Engineering*, vol. 54, pp. 539–550, 2016.
- [52] A. Ben Hamida, A. Benoit, P. Lambert, and C. Ben Amar, "3 d deep learning approach for remote sensing image classification," *IEEE Transactions on Geoscience and Remote Sensing*, vol. 56, no. 8, pp. 4420–4434, 2018.
- [53] B. Zafar, R. Ashraf, N. Ali et al., "Intelligent image classification-based on spatial weighted histograms of concentric circles," *Computer Science and Information Systems*, vol. 15, no. 3, pp. 615–633, 2018.
- [54] B. Zafar, R. Ashraf, N. Ali, M. Ahmed, S. Jabbar, and S. A. Chatzichristofis, "Image classification by addition of spatial information based on histograms of orthogonal vectors," *PLoS One*, vol. 13, no. 6, Article ID 0198175, 2018.
- [55] M. Jain, M. Bajwa, H. Kumar et al., "Agriculture assistant for crop prediction and farming selection using machine learning model with real-time data using imaging through uav drone," in *Emergent Converging Technologies and Bio-medical Systems*, pp. 311–330, Springer, Singapore, 2022.
- [56] C. Pati, A. K. Panda, A. K. Tripathy, S. K. Pradhan, and S. Patnaik, "A novel hybrid machine learning approach for change detection in remote sensing images," *Engineering Science and Technology, an International Journal*, vol. 23, no. 5, pp. 973–981, 2020.
- [57] Y. Li, J. Ma, and Y. Zhang, "Image retrieval from remote sensing big data: a survey," *Information Fusion*, vol. 67, pp. 94–115, 2021.
- [58] H. Shirmard, E. Farahbakhsh, R. D. Müller, and R. Chandra, "A review of machine learning in processing remote sensing data for mineral exploration," *Remote Sensing of Environment*, vol. 268, Article ID 112750, 2022.
- [59] A. J. Moshayedi, A. S. Roy, A. Kolahdooz, and Y. Shuxin, "Deep learning application pros and cons over algorithm," *EAI Endorsed Transactions on AI and Robotics*, vol. 1, pp. 1–13, 2022.
- [60] K. D. P. Pijush, S. Pal, M. Mukhopadhyay, and S. P. Singh, "Big data classification: techniques and tools," in *Applications of Big Data in Healthcare*, pp. 1–43, Elsevier, Landran, India, 2021.
- [61] M. Sajid, N. Ali, N. I. Ratyal et al., "Deep learning in age-invariant face recognition: a comparative study," *The Computer Journal*, vol. 65, no. 4, pp. 940–972, 2022.
- [62] K. Schulz, R. Hänsch, and U. Sörgel, "Machine learning methods for remote sensing applications: an overview," *Earth resources and environmental remote sensing/GIS applications*, Article ID 1079002, 2018.
- [63] M. Awais, W. Li, S. Hussain et al., "Comparative evaluation of land surface temperature images from unmanned aerial vehicle and satellite observation for agricultural areas using in situ data," *Agriculture*, vol. 12, no. 2, p. 184, 2022.
- [64] M. Sarafanov, E. Kazakov, N. O. Nikitin, and A. V. Kalyuzhnaya, "A machine learning approach for remote sensing data gap-filling with open bsource implementation: an example regarding land surface temperature, surface albedo and ndvi," *Remote Sensing*, vol. 12, no. 23, p. 3865, 2020.
- [65] A. Shabbir, N. Ali, J. Ahmed et al., "Satellite and scene image classification based on transfer learning and fine tuning of resnet50," *Mathematical Problems in Engineering*, vol. 2021, pp. 1–18, Article ID 5843816, 2021.
- [66] M. Kadhim and M. Abed, M. Huk, M. Maleszka, and E. Szczerbicki, "Convolutional neural network for satellite image classification," in *Asian Conference on Intelligent Information and Database Systems*, pp. 165–178, Springer, Cham, 2019.
- [67] Q. Liu, S. Basu, S. Ganguly et al., "Deepsat v2: feature augmented convolutional neural nets for satellite image classification," *Remote Sensing Letters*, vol. 11, no. 2, pp. 156–165, 2020.
- [68] M. A. Shafaey, H. Ebied, M. N. Al-Berry et al., "Deep learning for satellite image classification," in *International Conference on Advanced Intelligent Systems and Informatics*, pp. 383–391, Springer, 2018.
- [69] Q. Zhu, Y. Zhong, L. Zhang, and D. Li, "Adaptive deep sparse semantic modeling framework for high spatial resolution

- image scene classification,” *IEEE Transactions on Geoscience and Remote Sensing*, vol. 56, no. 10, pp. 1–16, 2018.
- [70] J. Xie, N. He, L. Fang, and A. Plaza, “Scale-free convolutional neural network for remote sensing scene classification,” *IEEE Transactions on Geoscience and Remote Sensing*, vol. 57, no. 9, pp. 6916–6928, 2019.
- [71] J. Fang, Y. Yuan, X. Lu, and Y. Feng, “Robust space-frequency joint representation for remote sensing image scene classification,” *IEEE Transactions on Geoscience and Remote Sensing*, vol. 57, no. 10, pp. 7492–7502, 2019.
- [72] Y. Liu, Y. Zhong, and Q. Qin, “Scene classification based on multiscale convolutional neural network,” *IEEE Transactions on Geoscience and Remote Sensing*, vol. 56, no. 12, pp. 7109–7121, 2018.
- [73] X. Lu, H. Sun, and X. Zheng, “A feature aggregation convolutional neural network for remote sensing scene classification,” *IEEE Transactions on Geoscience and Remote Sensing*, vol. 57, no. 10, pp. 7894–7906, 2019.
- [74] R. Zhu, Li Yan, Mo Mo, and Yi Liu, “AttentionBased deep feature fusion for the scene classification of HighResolution remote sensing images,” *Remote Sensing*, vol. 11, no. 17, p. 1996, 2019.
- [75] W. Zhang, P. Tang, and L. Zhao, “Remote sensing image scene classification using cnn-capsnet,” *Remote Sensing*, vol. 11, no. 5, p. 494, 2019.
- [76] G. S. Xia, J. Hu, F. Hu et al., “Aid: a benchmark data set for performance evaluation of aerial scene classification,” *IEEE Transactions on Geoscience and Remote Sensing*, vol. 55, no. 7, pp. 3965–3981, 2017.
- [77] F. Zhang, Bo Du, and L. Zhang, “Scene classification via a gradient boosting random convolutional network framework,” *IEEE Transactions on Geoscience and Remote Sensing*, vol. 54, no. 3, pp. 1793–1802, 2016.
- [78] R. S. A. Kareem, A. G. Ramanjineyulu, R. Rajan et al., “Multilabel land cover aerial image classification using convolutional neural networks,” *Arabian Journal of Geosciences*, vol. 14, no. 17, p. 1681, 2021.
- [79] Y. Zhong, F. Fei, and L. Zhang, “Large patch convolutional neural networks for the scene classification of high spatial resolution imagery,” *Journal of Applied Remote Sensing*, vol. 10, no. 2, Article ID 025006, 2016.
- [80] M. Verma, N. Gupta, B. Tolani, and R. Kaushal, “Explainable custom cnn architecture for land use classification using satellite images,” vol. 6, pp. 304–309, in *Proceedings of the Sixth International Conference on Image Information Processing (ICIIP)*, vol. 6, IEEE, Shimla, India, February 2021.
- [81] M. Wang, X. Zhang, X. Niu, F. Wang, and X. Zhang, “Scene classification of high-resolution remotely sensed image based on resnet,” *Journal of Geovisualization and Spatial Analysis*, vol. 3, no. 2, p. 16, 2019.
- [82] B. Zafar, R. Ashraf, N. Ali et al., “A novel discriminating and relative global spatial image representation with applications in cbr,” *Applied Sciences*, vol. 8, no. 11, p. 2242, 2018.
- [83] Ma Zhong, Z. Wang, C. Liu, and X. Liu, “Satellite imagery classification based on deep convolution network,” *International Journal of Computer and Information Engineering*, vol. 10, no. 6, pp. 1155–1159, 2016.
- [84] N. Laban, B. Abdellatif, M. Ebied, H. A. Shedeed, and M. F. Tolba, “Multiscale satellite image classification using deep learning approach,” *Studies in Computational Intelligence: Machine Learning and Data Mining in Aerospace Technology*, Springer, Cham, pp. 165–186, 2020.
- [85] X. Chang, C. Li, J. Wu, Li Lei, Q. Li, and A. Benjamin, “Land cover extraction of remote sensing images with parallel convolutional network,” in *Proceedings of the International Conference on Agro-Geoinformatics (Agro-Geoinformatics)*, pp. 1–6, IEEE, Shenzhen, China, September 2021.
- [86] H. Ebied, M. Al Berry, and M. Tolba, “Deep learning for satellite image classification,” in *Proceedings of the International Conference on Advanced Intelligent Systems and Informatics*, pp. 383–391, Springer, Cham, Switzerland, March 2018.
- [87] N. He, L. Fang, S. Li, A. Plaza, and J. Plaza, “Remote sensing scene classification using multilayer stacked covariance pooling,” *IEEE Transactions on Geoscience and Remote Sensing*, vol. 56, no. 12, pp. 6899–6910, 2018.
- [88] N. B. Crews and K. A. Crews, “Mapping vegetation morphology types in a dry savanna ecosystem: integrating hierarchical object-based image analysis with random forest,” *International Journal of Remote Sensing*, vol. 35, no. 3, pp. 1175–1198, 2014.
- [89] N. He, L. Fang, S. Li, J. Plaza, and A. Plaza, “Skip-connected covariance network for remote sensing scene classification,” *IEEE Transactions on Neural Networks and Learning Systems*, vol. 31, no. 5, pp. 1461–1474, 2020.
- [90] R. Shofiyati, “The role of remote sensing technology (latest geospatial) for agriculture in Indonesia,” in *2nd International Conference on Smart and Innovative Agriculture (ICoSIA 2021)*, pp. 243–248, Atlantis Press, Holland, Netherlands, 2022.
- [91] H. Jiang, M. Peng, Y. Zhong et al., “A survey on deep learning-based change detection from high-resolution remote sensing images,” *Remote Sensing*, vol. 14, no. 7, p. 1552, 2022.
- [92] Y. Tao, M. Xu, F. Zhang, Bo Du, and L. Zhang, “Unsupervised-restricted deconvolutional neural network for very high resolution remote-sensing image classification,” *IEEE Transactions on Geoscience and Remote Sensing*, vol. 55, no. 12, pp. 6805–6823, 2017.
- [93] A. Romero, C. Gatta, and G. Camps Valls, “Unsupervised deep feature extraction for remote sensing image classification,” *IEEE Transactions on Geoscience and Remote Sensing*, vol. 54, no. 3, pp. 1349–1362, 2016.
- [94] Z. H. Choudhury, “Encryption and encoding of facial images into quick response and high capacity color 2d code for biometric passport security system,” 2022, <https://arxiv.org/abs/2203.15738>.
- [95] Z. Xiong, F. Mo, X. Zhao, F. Xu, X. Zhang, and Y. Wu, “Dynamic texture classification based on 3d ica learned filters and Fisher vector encoding in big data environment,” *Journal of Signal Processing Systems*, vol. 10, pp. 1–15, 2022.
- [96] Y. D. Kwadiki and K. Kwadiki, “Content-based image retrieval using integrated features and multi-subspace randomization and collaboration,” *International Journal of System Assurance Engineering and Management*, pp. 1–11, 2022.
- [97] V. Babic and Z. Babić, “Unsupervised quaternion feature learning for remote sensing image classification,” *Ieee Journal of Selected Topics in Applied Earth Observations and Remote Sensing*, vol. 9, no. 4, pp. 1521–1531, 2016.
- [98] S. Bujwid, A. Pieropan, H. Azizpour, A. Maki, and M. Miquel, “An Analysis of Over-sampling Labeled Data in Semi-supervised Learning with Fixmatch,” 2022, <https://arxiv.org/pdf/2201.00604.pdf>.
- [99] K. Abhas, R. Bloch, and J. Lamond, *Cities and Flooding: A Guide to Integrated Urban Flood Risk Management for the 21st century*, World Bank Publications, 2012.

- [100] D. Lin, K. Fu, Y. Wang, G. Xu, and X. Sun, "Marta gans: unsupervised representation learning for remote sensing image classification," *IEEE Geoscience and Remote Sensing Letters*, vol. 14, no. 11, pp. 2092–2096, 2017.
- [101] P. Ladosz, L. Weng, M. Kim, and H. Oh, *Exploration in Deep Reinforcement Learning: A Survey*, Information Fusion, 2022.
- [102] S. Milani, N. Topin, M. Veloso, and F. Fang, "A Survey of Explainable Reinforcement Learning," 2022, <https://arxiv.org/abs/2005.06247>.
- [103] M. Maroto-Gómez, Á. Castro-González, J. C. Castillo, M. Malfaz, and M. Á. Salichs, "An adaptive decision-making system supported on user preference predictions for human-robot interactive communication," *User Modeling and User-Adapted Interaction*, vol. 554, pp. 1–45, 2022.
- [104] X. Shen, B. Liu, Y. Zhou, J. Zhao, and M. Liu, "Remote sensing image captioning via variational autoencoder and reinforcement learning," *Knowledge-Based Systems*, vol. 203, Article ID 105920, 2020.
- [105] K. Huang, W. Nie, and N. Luo, "Fully polarized sar imagery classification based on deep reinforcement learning method using multiple polarimetric features," *Ieee Journal of Selected Topics in Applied Earth Observations and Remote Sensing*, vol. 12, no. 10, pp. 3719–3730, 2019.
- [106] T. Hermosilla, M. A. Wulder, J. C. White, and N. C. Coops, "Land cover classification in an era of big and open data: optimizing localized implementation and training data selection to improve mapping outcomes," *Remote Sensing of Environment*, vol. 268, Article ID 112780, 2022.
- [107] S. A. Medjahed and M. Ouali, "Band selection based on optimization approach for hyperspectral image classification," *The Egyptian Journal of Remote Sensing and Space Science*, vol. 21, no. 3, pp. 413–418, 2018.
- [108] P. Boggavarapu and P. K. L. N. Boggavarapu, "Improved whale optimization based band selection for hyperspectral remote sensing image classification," *Infrared Physics & Technology*, vol. 119, Article ID 103948, 2021.
- [109] Z. Zhang and G. Zhang, "Genetic algorithm-based parameter optimization for eo 1 hyperion remote sensing image classification," *European Journal of Remote Sensing*, vol. 53, no. 1, pp. 124–131, 2020.
- [110] F. Huang, J. Lu, J. Tao, and L. Li, "Research on optimization methods of elm classification algorithm for hyperspectral remote sensing images," *IEEE Access*, vol. 7, pp. 201970–108089, Article ID 108070, 2019.
- [111] A. Rezaeipanah and M. Mojarad, "Modeling the scheduling problem in cellular manufacturing systems using genetic algorithm as an efficient meta-heuristic approach," *Journal of Artificial Intelligence and Technology*, vol. 1, no. 4, pp. 228–234, 2021.
- [112] A. Rida, A. Hicham, and N. Abderrahim, "Optimization of object-based image analysis with genetic programming to generate explicit knowledge from worldview-2 data for urban mapping," in *Geospatial Intelligence*, pp. 157–169, Springer, Cham, Switzerland, 2022.
- [113] A. Jamshed, B. Mallick, and R. Kumar Bharti, "An Efficient Pattern Mining Convolution Neural Network (Cnn) Algorithm with Grey Wolf Optimization (Gwo)," 2022, <https://arxiv.org/abs/2204.04704>.
- [114] F. Xie, C. Lei, F. Li, D. Huang, and J. Yang, "Unsupervised hyperspectral feature selection based on fuzzy c-means and grey wolf optimizer," *International Journal of Remote Sensing*, vol. 40, no. 9, pp. 3344–3367, 2019.
- [115] A. Kumar and S. Lekhraj, "Grey wolf optimizer and other metaheuristic optimization techniques with image processing as their applications: a review," *IOP Conference Series: Materials Science and Engineering*, vol. 1136, no. 1, Article ID 012053, 2021.
- [116] H. Faris, I. Aljarah, M. A. Al-Betar, and S. Mirjalili, "Grey wolf optimizer: a review of recent variants and applications," *Neural Computing & Applications*, vol. 30, no. 2, pp. 413–435, 2018.
- [117] W. Song, S. Li, L. Fang, and T. Lu, "Hyperspectral image classification with deep feature fusion network," *IEEE Transactions on Geoscience and Remote Sensing*, vol. 56, no. 6, pp. 3173–3184, 2018.
- [118] J. Zhu, L. Fang, and P. Ghamisi, "Deformable convolutional neural networks for hyperspectral image classification," *IEEE Geoscience and Remote Sensing Letters*, vol. 15, no. 8, pp. 1254–1258, 2018.
- [119] H. Kwon and H. Kwon, "Going deeper with contextual cnn for hyperspectral image classification," *IEEE Transactions on Image Processing*, vol. 26, no. 10, pp. 4843–4855, 2017.
- [120] G. Cheng, Z. Li, J. Han, X. Yao, and L. Guo, "Exploring hierarchical convolutional features for hyperspectral image classification," *IEEE Transactions on Geoscience and Remote Sensing*, vol. 56, no. 11, pp. 6712–6722, 2018.
- [121] R. Cao, L. Fang, T. Lu, and N. He, "Self-attention-based deep feature fusion for remote sensing scene classification," *IEEE Geoscience and Remote Sensing Letters*, vol. 18, no. 1, pp. 43–47, 2021.
- [122] T. Deselaers, D. Keysers, and H. Ney, "Features for image retrieval: an experimental comparison," *Information Retrieval*, vol. 11, no. 2, pp. 77–107, 2008.
- [123] C. Zhang, Y. Chen, X. Yang et al., "Improved remote sensing image classification based on multi-scale feature fusion," *Remote Sensing*, vol. 12, no. 2, p. 213, 2020.
- [124] Y. Ren, X. Zhang, Y. Ma et al., "Full convolutional neural network based on multi-scale feature fusion for the class imbalance remote sensing image classification," *Remote Sensing*, vol. 12, no. 21, p. 3547, 2020.
- [125] C. Mu, J. Liu, Yi Liu, and Y. Liu, "Hyperspectral image classification based on active learning and spectral-spatial feature fusion using spatial coordinates," *IEEE Access*, vol. 8, pp. 6768–6781, 2020.
- [126] Q. Zhu, Y. Zhong, Y. Liu, L. Zhang, and D. Li, "A deep-local-global feature fusion framework for high spatial resolution imagery scene classification," *Remote Sensing*, vol. 10, no. 4, p. 568, 2018.
- [127] E. Li, J. Xia, P. Du, and C. Lin, "Integrating multilayer features of convolutional neural networks for remote sensing scene classification," *IEEE Transactions on Geoscience and Remote Sensing*, vol. 55, no. 10, pp. 5653–5665, 2017.
- [128] Y. Yuan, J. Fang, X. Lu, and Y. Feng, "Remote sensing image scene classification using rearranged local features," *IEEE Transactions on Geoscience and Remote Sensing*, vol. 57, no. 3, pp. 1779–1792, 2019.
- [129] L. Kumar Tyagi, R. Kant, and A. Gupta, "A comparative analysis of various local feature descriptors in content-based image retrieval system," *Journal of Physics: Conference Series*, vol. 1854, Article ID 012043, 2021.
- [130] M. J. Alvarez, E. Gonzalez, F. Bianconi, J. Armesto, and A. Fernandez, "Colour and texture features for image retrieval in granite industry," *Dyna*, vol. 77, no. 161, pp. 121–130, 2010.
- [131] M. Ahmed and M. Taha, "A brief survey on modern iris feature extraction methods," *Engineering and Technology Journal*, vol. 39, no. 1, pp. 123–129, 2021.

- [132] Yu-xing Li, S.-bin Jiao, and X. Gao, "A novel signal feature extraction technology based on empirical wavelet transform and reverse dispersion entropy," *Defence Technology*, vol. 17, no. 5, pp. 1625–1635, 2021.
- [133] H. S. Munawar, R. Aggarwal, Z. Qadir, S. I. Khan, A. Z. Kouzani, and M. A. P. Mahmud, "A gabor filter-based protocol for automated image-based building detection," *Buildings*, vol. 11, no. 7, p. 302, 2021.
- [134] A. S. Ismail, X. Gao, and C. Deng, "Sar image classification based on texture feature fusion," in *Proceedings of the IEEE China Summit & International Conference on Signal and Information Processing (ChinaSIP)*, pp. 153–156, IEEE, Xi'an, China, September 2014.
- [135] H. Bi, L. Xu, X. Cao, and Z. Xu, "Polsar image classification based on three-dimensional wavelet texture features and Markov random field," in *Proceedings of the IEEE International Geoscience and Remote Sensing Symposium (IGARSS)*, pp. 3921–3928, IEEE, Fort Worth, TX, USA, December 2017.
- [136] R. Seifi Majdar and H. Ghassemian, "A probabilistic svm approach for hyperspectral image classification using spectral and texture features," *International Journal of Remote Sensing*, vol. 38, no. 15, pp. 4265–4284, 2017.
- [137] X. G. Kai, Q. L. Zhi, J. J. Wang et al., "The effect of cryogenic treatment on the microstructure and properties of ti-6al-4v titanium alloy," *Materials Science Forum*, vol. 747, pp. 899–903, 2013.
- [138] P. Khare and A. Khare, "Integration of wavelet transform, local binary patterns and moments for content-based image retrieval," *Journal of Visual Communication and Image Representation*, vol. 42, pp. 78–103, 2017.
- [139] M. Sajjad, A. Ullah, J. Ahmad, N. Abbas, S. Rho, and S. W. Baik, "Integrating salient colors with rotational invariant texture features for image representation in retrieval systems," *Multimedia Tools and Applications*, vol. 77, no. 4, pp. 4769–4789, 2018.
- [140] X.-yang Wang, Yu-nan Liu, H. Xu, P. Wang, and H.-ying Yang, "Robust copy-move forgery detection using quaternion exponent moments," *Pattern Analysis & Applications*, vol. 21, no. 2, pp. 451–467, 2018.
- [141] A. Nazir, R. Ashraf, T. Hamdani, and N. Ali, "Content based image retrieval system by using hsv color histogram, discrete wavelet transform and edge histogram descriptor," in *Proceedings of the international conference on computing, mathematics and engineering technologies (iCoMET)*, pp. 1–6, IEEE, Sukkur, Pakistan, April 2018.
- [142] M. I. Thusnavis Bella and A. Vasuki, "An efficient image retrieval framework using fused information feature," *Computers & Electrical Engineering*, vol. 75, pp. 46–60, 2019.
- [143] R. Ashraf, M. Ahmed, U. Ahmad, M. A. Habib, S. Jabbar, and K. Naseer, "Mdcbir-mf: multimedia data for content-based image retrieval by using multiple features," *Multimedia Tools and Applications*, vol. 79, no. 13-14, pp. 8553–8579, 2020.
- [144] M. K. Alsmadi, "Content based image retrieval using color, shape and texture descriptors and features," *Arabian Journal for Science and Engineering*, vol. 45, no. 4, pp. 3317–3330, 2020.
- [145] P. Alexey, S. Hitesh, I. Babakov, S. Parkhi, and G. Buddhawar, "Content-based image retrieval using color, texture and shape features," *Key Engineering Materials*, vol. 685, pp. 872–876, 2016.
- [146] B. S. Phadikar, A. Phadikar, and G. K. Maity, "Content-based image retrieval in dct compressed domain with mpeg-7 edge descriptor and genetic algorithm," *Pattern Analysis & Applications*, vol. 21, no. 2, pp. 469–489, 2018.
- [147] L. K. Sharmila and T. S. Sharmila, "An efficient framework for image retrieval using color, texture and edge features," *Computers & Electrical Engineering*, vol. 70, pp. 580–593, 2018.
- [148] G. Alimjan, T. Sun, Yi Liang, H. Jumahun, and Yu Guan, "A new technique for remote sensing image classification based on combinatorial algorithm of svm and knn," *International Journal of Pattern Recognition and Artificial Intelligence*, vol. 32, no. 07, Article ID 1859012, 2018.
- [149] L. N. Neelamsetti and P. Neelamsetti, "Multi temporal land use classification using hybrid approach," *The Egyptian Journal of Remote Sensing and Space Science*, vol. 18, no. 2, pp. 289–295, 2015.
- [150] A. Qayyum, A. Saeed Malik, N. M. Saad et al., "Image classification based on sparse-coded features using sparse coding technique for aerial imagery: a hybrid dictionary approach," *Neural Computing & Applications*, vol. 31, no. 8, pp. 3587–3607, 2019.
- [151] Ce Zhang, X. Pan, H. Li et al., "A hybrid mlp-cnn classifier for very fine resolution remotely sensed image classification," *ISPRS Journal of Photogrammetry and Remote Sensing*, vol. 140, pp. 133–144, 2018.
- [152] R. Nijhawan, H. Sharma, H. Sahni, and A. Batra, "A deep learning hybrid cnn framework approach for vegetation cover mapping using deep features," in *Proceedings of the 13th International Conference on Signal-Image Technology & Internet-Based Systems (SITIS)*, pp. 192–196, IEEE, Jaipur, India, April 2017.
- [153] S. V. S. Prasad, T. S. Savithri, and I. Murali Krishna, "Comparison of accuracy measures for rs image classification using svm and ann classifiers," *International Journal of Electrical and Computer Engineering*, vol. 7, no. 3, p. 1180, 2017.
- [154] M. D. Yang, K. S. Huang, Yi H. Kuo, H. P. Tsai, and L.-M. Lin, "Spatial and spectral hybrid image classification for rice lodging assessment through uav imagery," *Remote Sensing*, vol. 9, no. 6, p. 583, 2017.
- [155] J. Akshya and P. L. K. Priyadarsini, "A hybrid machine learning approach for classifying aerial images of flood-hit areas," in *Proceedings of the International Conference on Computational Intelligence in Data Science (ICCIDS)*, pp. 1–5, IEEE, Chennai, India, October 2019.
- [156] Y. Hua, L. Mou, and X. Zhu, "Recurrently exploring class-wise attention in a hybrid convolutional and bidirectional lstm network for multi-label aerial image classification," *ISPRS Journal of Photogrammetry and Remote Sensing*, vol. 149, pp. 188–199, 2019.
- [157] K. Bitner and K. Bittner, "Automatic building footprint extraction from multi-resolution remote sensing images using a hybrid fcn," *ISPRS International Journal of Geo-Information*, vol. 8, no. 4, p. 191, 2019.
- [158] P. Deepan and L. R. Sudha, *Scene classification of remotely sensed images using ensembled machine learning models*, pp. 535–550, Environmental Science, Springer, Singapore, 2021.

Research Article

Evaluation of the Effectiveness of Collusion Control Policy Implementation by BP Neural Network Based on Annealing Algorithm Optimization

Chongsen Ma , Yun Chen , and Zeyang Lei 

School of Traffic & Transportation Engineering, Changsha University of Science and Technology, 410000 Hunan, China

Correspondence should be addressed to Chongsen Ma; machongsen@stu.csust.edu.cn

Received 16 January 2022; Revised 28 February 2022; Accepted 8 March 2022; Published 23 March 2022

Academic Editor: Afaq Ahmad

Copyright © 2022 Chongsen Ma et al. This is an open access article distributed under the Creative Commons Attribution License, which permits unrestricted use, distribution, and reproduction in any medium, provided the original work is properly cited.

Due to the national economic development form and social development demand, in recent years, the government has been vigorously promoting the control of government-enterprise collusion in the bidding process of government projects in order to promote the standardization of the market. How to predict the vertical collusion behavior under different internal and external environments has become an important research content. Although the prediction of individual behavior is difficult to achieve, the prediction of group behavior has certain possibilities. In this paper, we propose a method for predicting and evaluating the vertical collusion behavior of government investment project bidding based on BP neural network analysis optimized by an annealing algorithm. First, drawing on the traditional evaluation model, the evaluation index system of government-enterprise collusion behavior is constructed from five dimensions: internal environment, external environment, policy development, enforcement effort, and feedback channel. Secondly, a machine learning method based on BP neural network optimized by an annealing algorithm is introduced to evaluate the influence of the change of initial conditions on the bidding collusion behavior. This study has certain significance for government managers to discover the problems and causes in policy formulation, which in turn can support the government in further improving the policy utility.

1. Introduction

Policy formulation and evaluation of management effectiveness is a systematic and complex task, and with the continuous development of China's engineering construction field, the management of corrupt practices in the bidding process of government projects has become increasingly strict [1, 2]. However, the same control policy under different external conditions can lead to different strategies adopted by each participant in the bidding of government investment engineering projects [3]. Therefore, it is of greater practical significance to predict the vertical collusion behavior of each group in the bidding of government investment engineering projects and to carry out targeted control according to the prediction results.

Vertical collusion in bidding for engineering projects can bring high economic benefits to each stakeholder, and all

parties tend to maximize their profit in the process of project execution [4]. At the same time, in the vertical hierarchical relationship, some actors in the information disadvantage have the information demand, while another actor in the information advantage has the information rent-seeking supply, so the information asymmetry motivates the vertical actor to reach the vertical collusion based on information trading [5]. In the absence of additional costs, collusion is likely to occur between stakeholders in bidding for engineering projects regardless of whether the cost of vertical collusion is symmetrical or not; the possibility of collusion is higher when the cost of collusion is symmetrical; in the presence of additional costs, it can promote the occurrence of collusion in the case of asymmetrical cost of collusion [6]. Therefore, the prediction of changes in regional collusion behavior through reasonable external conditions and the environment in

which collusion occurs can help relevant policies and targeted management behavior.

There are many influencing factors that affect the change of vertical collusion behavior. By utilizing these factors, it is possible to effectively remedy the deficiencies in policy formulation, save management efforts, and optimize the implementation to improve the science of policy formulation [7]. For example, taking the number of government project bidding collusion cases in a city as the research object, the BP neural network model and algorithm based on annealing algorithm optimization can be used to analyze the relationship between the changes in the number of cases and the external economic environment, the tension between supply and demand in the market, and the government's enforcement efforts. Meanwhile, by decomposing these relationships into optimization problems, and through the solution of the optimization problems, more adaptive policies can be formulated. The paper is based on the Chinese Comprehensive Social Survey (CCS).

The paper analyzes and mines the data based on the Chinese General Social Survey (CGSS) [8] and the relevant data from the National Bureau of Statistics. The paper provides more governmental governance of collusion between government and enterprises with decision support by evaluating the degree of collusion between government and enterprises in the bidding field of government investment projects and analyzing the degree of change in collusion behavior under different environmental combinations.

The innovation points of this paper are mainly reflected in

- (1) A prediction model about vertical collusion behavior in government investment engineering project bidding based on the BP neural network optimized by the annealing algorithm is established.
- (2) In the evaluation process, evaluation indexes such as market collusion tendency and government integrity degree on collusion behavior are added to make the evaluation model more realistic.

The research in this paper mainly addresses the following issues.

- (1) In the process of policy formulation for the prevention of collusion in bidding, the implementation effects of the same policies in different cities differ greatly. Therefore, how to determine the policies that are more adapted to the local economic development status and actual conditions before the policies are promulgated.
- (2) How to evaluate the effects of policies already promulgated and optimize the relevant policies.

2. Literature Review

2.1. Vertical Collusion in Bidding for Government Investment Projects. Due to information asymmetry among parties, disorderly competition among enterprises, imperfect regulatory mechanisms, and the bidding process, the market is highly competitive and most enterprises cannot obtain fair

competition [9]. The engineering bidding process includes multiple types of participating subjects, such as bidders, agencies, and supervisory bodies [10]. Due to the complex relationship among the participating subjects, collusion in the bidding process has various types [11, 12]. Vertical collusion refers to the existence of hierarchical differences between colluders, similar to those between superiors and subordinates. Vertical collusion mainly includes vertical collusion between bidders, collusion between agencies and bidders, collusion between bid evaluation experts and bidders, collusion between supervisory agencies and bidders, and multiparty collusion. The emergence of vertical collusion has indirectly promoted the proliferation and development of bidding irregularities. Therefore, it is of great significance to predict collusion through the external environment and local market atmosphere. Thus, how to detect and govern this bidding behavior is also a hot issue being studied by many scholars [13]. Due to the strong randomness of individual behavior, the accuracy and significance of predicting individual decision-making behavior are low. However, the prediction of group behavior can effectively reduce the influence of individual random behavior on the results. By predicting the changes of the internal and external environment on the vertical collusion behavior in the bidding process, the collusion behavior can be effectively controlled. Sirui Nie et al. pointed out that the vertical collusion of bidding will lead to a decline in the quality of the project and various negative effects, while the occurrence of collusion [14] is relatively hidden and difficult to identify. Therefore, an effective and rapid method is necessary to measure the tendency of vertical collusion in bidding to discover vertical collusion in bidding [15].

2.2. Factors Influencing Vertical Collusion in Bidding for Government Investment Projects. The collusive behavior of bidding is formed by a combination of influencing factors. The incomplete implementation of the bidding system is an important reason for the prevalence of collusion in government investment projects [16]. This is actually a reflection of the long-standing lack of policy implementation in the bidding field. For a long time, local governments and competent officials have tended to adopt alternative strategies to deal with the implementation of laws and policies. Meanwhile, the implementers choose to adapt the implementation of policies that are not profitable so that indicators such as the level of corruption in the government of the bidding place and the tendency of local collusion have a greater impact on the generation of vertical collusion.

Economic motivation is also one of the important reasons for collusion in the bidding process [17]. The reason for this is that the costs and risks of collusion are low compared to the benefits. The cost includes not only the implementation cost of collusion but also the implementation cost and the risk cost. At the same time, the profit-seeking and competition caused by the market economy also contribute to the creation of power and money transactions and collusion in the bidding process in disguise. The local economic development and the degree of

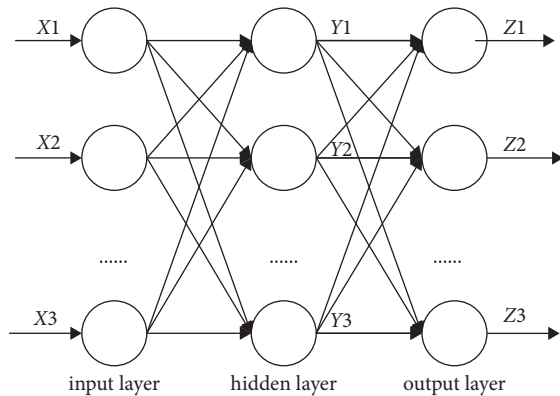


FIGURE 1: Network structure diagram.

competition in the market will have an impact on the collusion. Through research, Henke believes that in the existing bidding model, refusing bribes will increase the participation costs of “honest agents,” has negative externalities and leads to potential corrupt practices [18].

2.3. BP Neural Network and Simulated Annealing Algorithm.

The BP algorithm originated in the 1980s, has the error back propagation training discovered by David Rumelhart et al. [19]. The algorithm is a model that mimics the neurons of the brain to deal with uncertainty problems. The standard BP neural network is trained twice by the error back propagation algorithm and belongs to a three-layer feedforward network that consists of an input layer, a hidden layer, and an output layer. The main features are that the signal is forward propagation and the error is backward propagation. The BP neural network has better prediction results for highly uncertain problems. The BP algorithm takes the square of the network error as the objective function and uses the gradient descent method to calculate the minimum value of the objective function.

BP neural network is essentially a simplified biological model, where the output and input structure on the neural network is a single-layer structure, while the hidden layer is a multilayer structure. All components are connected. The input layer passes the information to the hidden layer after getting the stimulus, and the hidden layer passes the weight information to the output layer according to the calculation rules, and the output layer compares the results and adjusts the weights if the results are incorrect. In other words, the BP neural network uses the backpropagation algorithm to calculate the model for several iterations given the training set D . Finally, the parameters of the training neural network model are determined according to the error requirements. A schematic diagram of the structure of the BP neural network is shown in Figure 1.

2.4. Application of BP Neural Network in the Evaluation Field.

BP neural networks have a wide range of applications in nonlinear modeling, system identification, etc. While general neural networks have a predetermined number of network layers, BP neural networks do not require

predetermination. Two-layer BP networks achieve the fitting of arbitrary functions without limiting the number of hidden nodes. Therefore, in practical applications, BP neural networks are usually selected with 2 layers.

In 2015, Yang Baoan et al. combined BP neural networks with corporate financial analysis and demonstrated the applicability of neural networks in financial analysis [20]. Zeng Zhongdong, on the other hand, found that a neural network model can be useful for establishing a dynamic early warning mechanism for companies in the insurance industry [21]. Fu et al. combined BP neural network with hierarchical analysis to analyze green marketing and found that a high prediction accuracy could be achieved [19]. Yang et al. used a BP neural network to predict the level of teaching management and provide help to improve teaching [22]. Yu et al. found that campus congestion could be better predicted using the BP neural network [23]. Liu Qi et al. found that BP neural networks have high feasibility for application in the field of GEM enterprise value assessment [24]. Wang et al. used the autoregressive integrated moving average (ARIMA) method and the back propagation neural network (BPNN) method to forecast carbon emissions in China, India, the United States, and the European Union in the absence of COVID-19 [25]. Lyu et al. utilized the GANN algorithm predicting the torsional strength of reinforced concrete (RC) beams [26]. In summary, it can be found that BP neural networks have high application value and applicability in the field of multiindustry evaluation. Therefore, the introduction of this method in the field of policy adaptability evaluation has high rationality.

2.5. *Simulated Annealing Algorithm.* The simulated annealing (SA) algorithm is derived from the process of temperature change, and the SA algorithm has a strong local search capability [23]. The process is similar to physical annealing, also known as system temperature, by accepting an increase in the objective function through the standard probability rules of Metropolis. SA obtains the global optimal solution to the problem by repeating the sampling during the decrease of the system temperature.

3. BP Neural Network Optimized by Annealing Algorithm

3.1. *Determination of Relevant Evaluation Indicators.* In the traditional government project bidding process, the evaluation process for the change of collusive behavior usually prefers to select quantitative indicators, but the adoption of quantitative indicators for group behavior prediction does not fully reflect the influence of human subjective factors on behavior. At the same time, in the actual implementation process, the same policy achieves a wide range of effects in different cities. It also indicates that, in addition to the basic external conditions, qualitative indicators also have a certain influence on the implementation effect of the project. Therefore, it is of great practical value to use a more objective method to evaluate the behavior of each decision maker in the bidding collusion process and to optimize it on this basis.

TABLE 1: Table of influencing factors.

Primary indicators	Secondary indicators	Source
Internal environment	Propensity to collude degree	CGSS2017
	Government corruption perception degree	CGSS2015
External environment	Economic development GDP total (billion yuan)	Statistical yearbook
	Development of private economy	Statistical yearbook
	Total construction industry output value	Statistical yearbook
Policy development	Number of relevant laws	Statistical yearbook
	Level of new laws	National laws and regulations database
	Type of policy	
	Main target groups	
Enforcement efforts	Whether there was a special state action in the current year	General office of the CPC central committee website
	Fairness of justice	CGSS2015
	Fairness of trial	CGSS2015
Feedback channels	Monitoring the effectiveness of the process	CGSS2015
Effectiveness evaluation	Rate of increase percentage of decrease percentage of decrease	Judgmental instruments network

By reading the previous literature and analyzing the influencing factors of the bidding collusion process, we finally determined 13 evaluation indexes in 5 categories and selected the number of colluding groups choosing to collude and break the law as the output value to predict the vertical collusion behavior of the groups. Since the implementation of the policy has a certain lag, this paper selects the average growth rate of the first two years of policy implementation, versus the second two years, as evaluation indicators to increase the credibility of the results.

In the external environment, the economic level in the year of policy making in the implementation place is mainly considered, including GDP and the intensity of market competition. The internal environment indicators include the degree of local collusion tendency and the perceived degree of government corruption (data from CGSS2015 and CGSS2017 survey data); the policy making environment needs to be clarified for the level of policy making and the main target group of the policy, etc. The different effects of different levels of policies on the control of collusion also have a large difference. Under the same policy and external conditions, if the government's implementation strength is different, it will also have a certain influence on the behavior of collusion subjects. Therefore, we choose to evaluate the policy implementation strength (i.e., whether special control actions were carried out in the same year) and the degree of judicial impartiality and trial impartiality; the feedback of the implementation process is reflected by the indicators of the effectiveness of supervision procedures. The relevant evaluation indicators are shown in Table 1.

3.2. BP Neural Network Based on Annealing Algorithm Optimization. In the SA-BP algorithm, the neural network structure first needs to be determined and subsequently optimized using a degradation algorithm. After the relevant parameters have been determined, the BP neural network is used to make predictions. It is assumed that the BP neural network has n nodes in the input layer, q nodes in the hidden layer, and m nodes in the output layer, and the weights

between the nodes in the input layer to the nodes in the hidden layer are V_{ij} and the weights between the nodes in the hidden layer to the nodes in the output layer are W_{jk} .

In the forward propagation phase, the hidden layer output O_j and the output O_k of the output layer are

$$\begin{cases} o_j = f(\text{net}_j) f\left(\sum_{i=1}^n v_{ij} x_i - \theta_j\right) \\ o_k = f(\text{net}_k) f\left(\sum_{i=1}^n w_{jk} o_i - \delta_k\right) \end{cases}, \quad (1)$$

where x_i is the input layer sample data, net_j , net_k are the net input data of the j th, k th node of the hidden layer. θ_j , δ_k are the node thresholds. $f(\text{net})$ is the selected training function.

The error back propagation phase with error signals is

$$\begin{cases} \delta_k = -\frac{\partial E}{\partial o_k} \cdot \frac{\partial o_k}{\partial \text{net}_k} \\ \theta_j = f'(\text{net}_j) \sum_{k=0}^{m-1} \delta_k w_{jk} \end{cases}, \quad (2)$$

where E is the total error.

The weighting corrections are

$$\begin{cases} \Delta w_{jk} = \eta o_j (dk - ok) ok (1 - ok) \\ \Delta v_{jk} = o_j (1 - o_j) \sum_{k=0}^{m-1} \delta_k w_{jk} o_i. \end{cases} \quad (3)$$

$\eta \in (0, 1)$ is for learning rates.

The steps of the BP neural network operation based on the optimization of the SA algorithm are as follows:

- (1) *Initialization.* Let us determine the problem domain, select certain values as initial weights, determine the number of nodes in the input layer, hidden layer, and output layer of the BP neural network, and the initial values of the annealing algorithm; initial

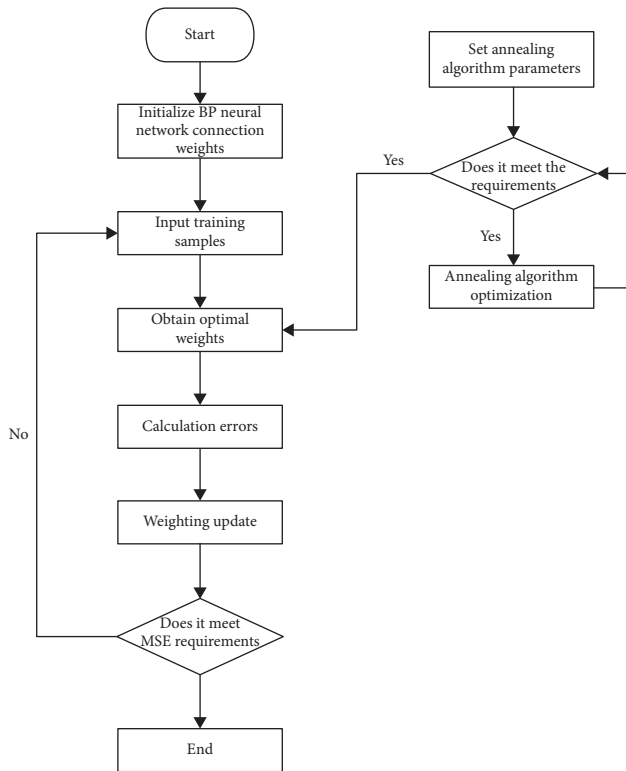


FIGURE 2: Block diagram of the operational flow.

temperature, annealing times, crossover probability, and variation probability, and other related parameters. The initial solution is generated randomly, and the objective function value of this solution is calculated.

- (2) Let us transform the current solution in the solution space according to the generated perturbation function to generate a new solution and calculate the objective function value of the new solution.
- (3) If the new solution outperforms the old solution, then replacement is performed. If not, it is replaced with a certain probability, according to Metropolis.
- (4) The solution is judged by whether the requirements are satisfied or not.
- (5) Let us end if the maximum number of substitutions is reached. If not, an annealing operation is performed to reduce the temperature.
- (6) Let us substitute the optimal node weights obtained by the neural network and train the sample data.
- (7) Then we calculate the mean square error (MSE) of the training results and determine whether the requirements are met.

The block diagram of the operational flow is shown in Figure 2.

4. Empirical Analysis of Predicting Group Behavior of Vertical Collusion in Bidding for Government Investment Projects

4.1. Mixed Stabilisation Strategy for Gaming Subjects. In order to verify the applicability of the algorithm and the effectiveness of the fit to the relevant data, MATLAB simulation was used to simulate the proportional decrease of relevant cases before and after the promulgation of the policy in relevant cities in China. In order to ensure the validity of the data, a total of 166 samples from 31 provinces, cities, and autonomous regions were selected for the simulation from the promulgation of the Measures on Bidding and Tendering for Engineering Construction Projects in 2005 to the end of 2020.

The output parameters were the percentage decrease in the growth rate of cases and the percentage decrease in the variance. Before the training started, the maximum number of training cycles was set to 1000, the proportion of validation samples was set to 15%, and the proportion of test samples was set to 15%. The annealing algorithm parameters were set to a start temperature of 97°C, an end temperature of 3°C, and a decay coefficient of 0.8. MATLAB was used for the simulation.

As can be seen from Figure 3, with the continuous optimization of the simulation degradation algorithm, the current accepted optimal solution is continuously close to the historical optimal solution, the value of the mean error gradually decreases, and the model obtains a higher degree of fit.

From Figure 4, it can be found that the validation sample obtained the best fit after the 6th training session as the number of training sessions continued to increase.

From Figures 5 and 6, it can be seen that the actual effect of the test data has a small error with the prediction result. Over 70% of the predicted data is distributed around the 0 error line.

Therefore, the BP neural network optimized based on the simulated annealing algorithm can better predict the effect of government project bidding control policies, providing some reference value for the government to formulate policies. It also provides a basis for how the government formulates policies according to the local external environment, economic conditions, and the level of market development.

The simulation results show that changes in vertical collusion in tendering can be better predicted through indicators such as external conditions and the internal environment. It also shows that the above conditions have an impact on the creation of bid collusion. Therefore, the control path of the project can be investigated through the above indicators.

For researchers, this model extends the existing research and proposes a vertical collusion behavior prediction model for government investment project bidding based on SA-BP, which provides a new research direction for related research. For the government, before formulating policies on the control of collusion behavior in bidding, it can conduct

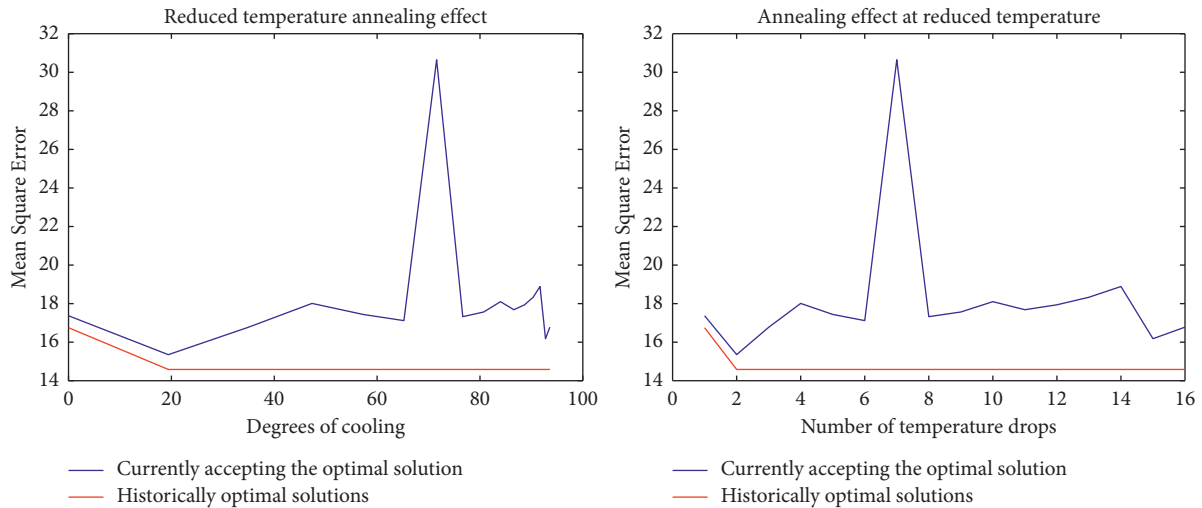


FIGURE 3: Annealing effect at reduced temperature.

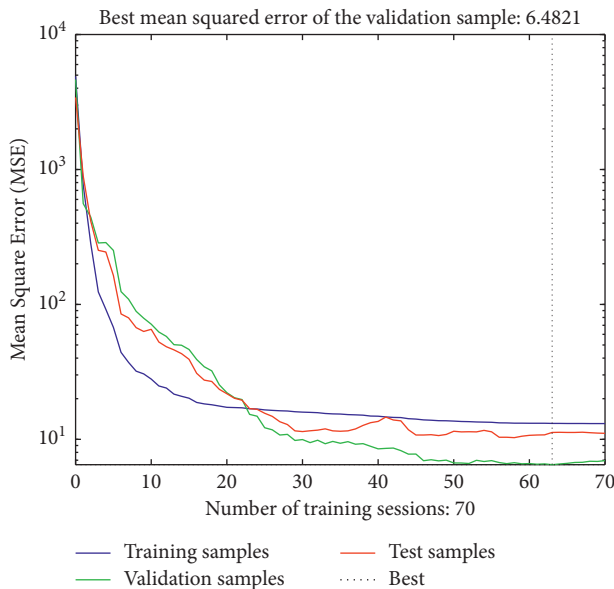


FIGURE 4: Plot of mean squared error of training times.

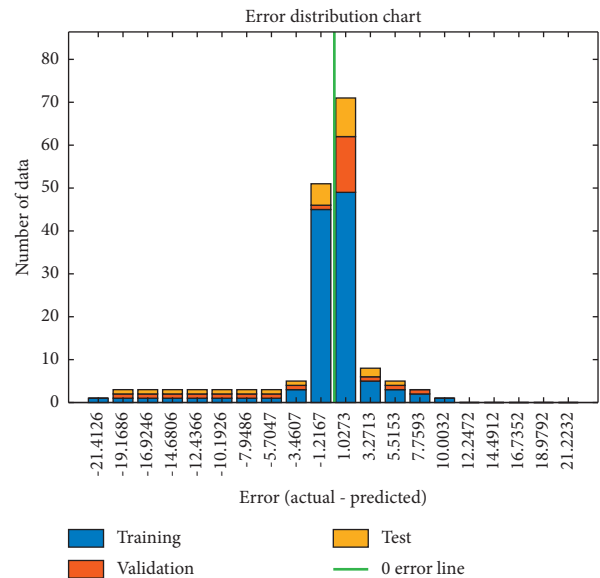


FIGURE 5: Sample regression plots.

research on the external environment of the city where the policy is implemented to predict the effect of vertical collusion control after the implementation of the new policy, provide data basis and theoretical support for policy formulation, and improve the pertinence of control policies. For project managers, the degree of control of vertical collusion behavior in the bidding process has a greater impact on the difficulty of project acquisition and project profits. So the model proposed in the research can be used to predict the vertical collusion behavior before the bidding, providing guidance for management work.

5. Conclusions and Limitations

5.1. Conclusions

- (1) In the actual calculation, 166 samples from 31 provinces, cities, and autonomous regions in China

were selected for the analysis, covering the changes in vertical collusion in most cities in China after 2005. The introduction of the simulated annealing algorithm avoids the complex process of parameter selection in BP neural networks and facilitates the extension of the method.

- (2) The results of the study showed that the use of SA-BP models to predict collusion bidding behavior has a high accuracy rate. The model constructed in this paper can be used to predict changes in bidding behavior, help relevant government departments predict changes in bidding behavior, and provide data support for the government to formulate control policies.
- (3) The BP neural network vertical collusion behavior prediction model of government project bidding based on the optimization of the annealing algorithm

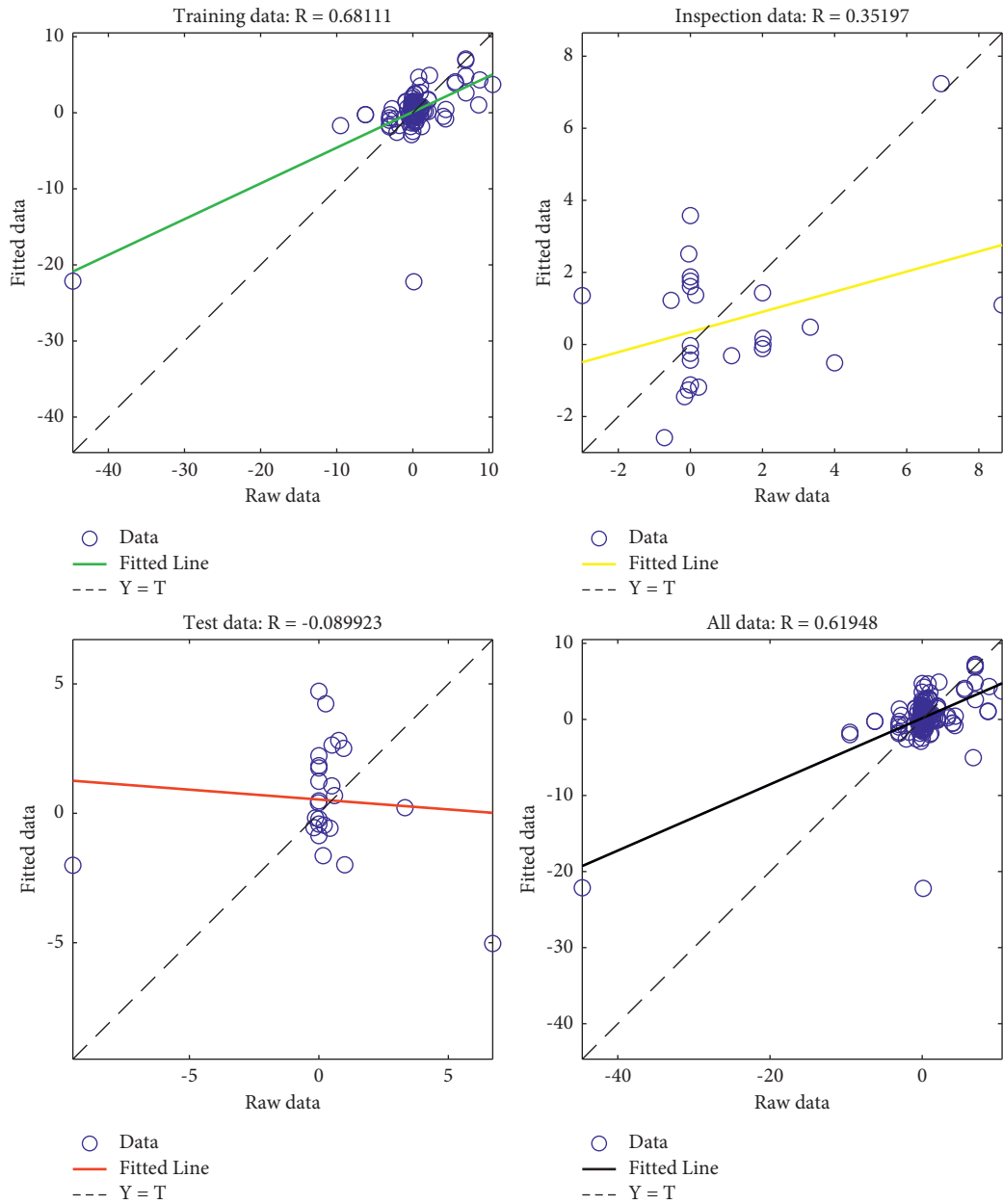


FIGURE 6: Error distribution chart.

proposed in this paper effectively solves the problem of policy formulation and implementation mainly relying on subjective judgment and lacking data guidance in the current process of bidding collusion behavior control process by using external conditions to predict the change trend of collusive behavior.

5.2. Limitations

- (1) As some of the data collection remained the same during the writing of the thesis, necessary simplifications were made to the indicators in the model building process. In future research, the credibility of

the model can be enhanced by increasing the scale of the survey and obtaining relevant data.

- (2) In the process of future practice, multiple deep learning models and research methods can be used to predict the behavior of vertical collusion groups, analyze the influence of external conditions on collusion behavior under different circumstances and achieve crossvalidation of the research results.

Data Availability

The raw data supporting the conclusions of this article will be made available by the authors, without undue reservation.

Conflicts of Interest

The authors declare that they have no conflicts of interest regarding this work.

Acknowledgments

National Natural Science Foundation of China (no. 71771031).

References

- [1] X. Ding, *Research on the Prevention and Control Mechanism of Bidding Integrity Risk*, Wuhan University, Wuhan, Hubei, 2013.
- [2] C. Yao and W. Duan, "Insider information trading corruption: a new corruption trend," *Journal of Shanghai University (Social Sciences Edition)*, vol. 33, no. 1, pp. 78–90, 2016.
- [3] J. Chen and Y. Hou, "Research on the identification of collusion behavior of multi-interest subjects in engineering project bidding," *Journal of Railway Science and Engineering*, vol. 17, no. 3, pp. 784–790, 2020.
- [4] Le Yun, B. Zhang, X. Guan, and Y. Li, "A study of collusion in government investment projects based on SNA perspective," *Journal of Public Management*, vol. 10, no. 3, pp. 138–139, 2013.
- [5] X. Huo, *Information Asymmetry between the Main Participants of Engineering Projects and its Prevention Strategy*, Chongqing University, Shapingba, 2015.
- [6] Y. Wu, *Research on the Formation and Control of gray Interest Chain between Bidders and Tenderers of Government Investment Engineering Projects*, Changsha University of Technology, Wangxin Rd, Yuelu, 2019.
- [7] H. Nie and Y. Zhang, "Decentralization, centralization and collusion between government and enterprises," *The World Economy*, vol. 38, no. 6, pp. 3–21, 2015.
- [8] "China Integrated Social Survey," 2003, <http://cgss.ruc.edu.cn/>.
- [9] N. Xu, *Research on the Prevention of Dilemma of Bidding for Engineering Projects*, Tianjin University of Technology, Tianjin, 2017.
- [10] X. Du, *Research on the Governance of Corruption in the Development of Public Procurement System*, Nanjing University, Gulou, Nanjing, 2017.
- [11] J.'e Zhou, *Analysis of Horizontal Collusion in Construction Bidding and Research on Governance Mechanism*, Tianjin University of Technology, Tianjin, 2010.
- [12] E. Chen and L. Ding, "Analysis of the causes of vertical collusion in bidding of government investment projects," *Journal of Changsha University of Technology (Natural Science Edition)*, vol. 15, no. 2, pp. 30–36, 2018.
- [13] R. Signor, P. E. D. Love, A. Oliveira, A. O. Lopes, and P. S. Oliveira, "Public infrastructure procurement: detecting collusion in capped first-priced auctions," *Journal of Infrastructure Systems*, vol. 26, no. 2, Article ID 05020002, 2020.
- [14] W. Lee, *Research on the Governance of Illegal and Unlawful Acts of Bidding and Tendering in Engineering Construction*, Xi'an University of Architecture and Technology, Beilin, Xi'an, 2017.
- [15] Y. Chen and S. Nie, "Calculating model of vertical collusion tendency degree in bidding of government investment projects," *Journal of Railway Science and Engineering*, vol. 15, pp. 1–8, 2022.
- [16] H. Chunyan, *Research on Collusion in Bidding for Engineering Projects and its Prevention*, Henan University of Technology, Zhongyuan, 2020.
- [17] D. E. Rumelhart and J. L. McClelland, "Parallel distributed processing, explorations in the microstructure of cognition," *MIT Press iCambridge Ma*, vol. 63, no. 4, pp. 5–12, 1986.
- [18] A. Henke, F. Khalil, and J. Lawarree, "Honest agents in A corrupt equilibrium," *Journal of Economics and Management Strategy*, 2022.
- [19] B. Yang, Ji Hai, J. Xu, and J. Wen, "Application of BP neural network in enterprise financial crisis early warning," *Forecasting*, vol. 20, no. 2, pp. 49–54+68, 2001.
- [20] Z. Zeng, "Construction of an early warning system for insurance enterprise business risk based on fuzzy preference and neural network," *Journal of Sichuan University (Medical Science Edition)*, vol. 2006, no. 2, pp. 28–34, 2006.
- [21] J. Fu and Li Zhang, "Green marketing performance evaluation of circular economy based on AHP and BP neural network model," *Science and Technology Management Research*, vol. 32, no. 2, pp. 215–220+242, 2012.
- [22] X. S. Yang, J. Zhou, and D. Q. Wen, "An optimized BP neural network model for teaching management evaluation," vol. 40, no. 2, pp. 3215–3221, 2021.
- [23] X. Yu, S. Xiong, Y. He, W. E. Wong, and Y. Zhao, "Research on campus traffic congestion detection using BP neural network and Markov model," *Journal of Information Security and Applications*, vol. 31, pp. 54–60, 2016.
- [24] Q. Liu, *Research on Value Assessment of High-Tech GEM Listed Companies Based on PCA-GA-BP Neural Network Model*, Shanghai University of Finance and Economics, Wujiaochang, 2020.
- [25] Q. Wang, S. Li, R. Li, and F. Jiang, "Underestimated impact of the COVID-19 on carbon emission reduction in developing countries - a novel assessment based on scenario analysis," *Environmental Research*, vol. 204, Article ID 111990, 2022.
- [26] Z. Lyu, Y. Yu, B. Samali et al., "Back-propagation neural network optimized by K-fold cross-validation for prediction of torsional strength of reinforced Concrete beam," *Materials*, vol. 15, no. 4, p. 1477, 2022.
- [27] F. Pang, *Principle of Simulated Annealing Algorithm and Application of the Algorithm to Optimization Problems*, Jilin University, Chaoyang, 2006.